MULTI-SCALE MODELING AND CONTROL OF LIQUID-GAS FLOWS WITH A FOCUS ON SPRAY ATOMIZATION

A Dissertation

Presented to the Faculty of the Graduate School

of Cornell University

in Partial Fulfillment of the Requirements for the Degree of

Doctor of Philosophy

by

Lam Xuan Vu

August 2022

MULTI-SCALE MODELING AND CONTROL OF LIQUID-GAS FLOWS WITH A FOCUS ON SPRAY ATOMIZATION

Lam Xuan Vu, Ph.D.

Cornell University 2022

In the context of the climate crisis, fuel sprays are of great societal importance because they directly impact energy consumption and pollutant emissions in liquid-fueled combustion systems. More broadly, liquid sprays appear in a wide range of applications such as powder production for additive manufacturing, drug encapsulation, and coatings for materials. Because of their importance and ubiquity, there is a strong desire to better model the spray atomization process and to develop optimization and control strategies to improve efficiency and to aid in the design of spray systems. However, computational modeling of atomization presents enormous challenges, in part because the extreme complexity of the associated flow field and because of the wide range of length and time scales involved.

In the first part of this work, I present a multi-scale simulation strategy that models the full spray atomization region from first principles. In contrast to prior work, this approach simulates the atomization process end-to-end, i.e., from the inlet of the injector to the spray dispersion region downstream. To that end, multiple simulation domains are coupled together to address the wide range of length scales that need to be captured. Another significant departure from standard approaches is that multiple sub-grid scale models are introduced to account for unresolved processes, most importantly a thin structure break-up model to explicitly model topology change. Simulations of a canonical two-fluid atomizer are quantitatively validated against experiments at identical operating conditions,

including drop size statistics.

As the computational prediction of liquid-gas flows remains arduous, it is no surprise that numerical frameworks for optimal control of liquid-gas flows have not received much attention from researchers yet. In the second part of this work, I present one of the very first computational adjoint frameworks for the optimization of liquid-gas flows using a sharp interface model. This approach is verified by showing low gradient errors for a range of test cases. It is then used to maximize the growth of a temporally evolving liquid-gas mixing layer, which demonstrates the potential of the proposed method for optimizing spray formation.

BIOGRAPHICAL SKETCH

Lam Xuan Vu was born in Anaheim California on September 21st, 1994 and raised in Southern California. He attended Fountain Valley High School where his interest in science began while taking a chemistry class. He attended college locally at the University of California, Irvine (UCI). There, he was fortunate enough to work as an undergraduate researcher at UCI's experimental wind tunnel lab whose research focused on turbulence. During his time in the lab, he assisted graduate students in data collection – turning knobs and, on too many occasions, accidentally breaking fragile hot-wire probes. Memorable and intriguing experiences in the lab prompted Lam to apply to graduate school with the intent to study fluid dynamics. In 2016 after graduating from UCI, Lam traded in his sunglasses and sandals for a winter coat, moving from sunny California to snowy New York to attend Cornell University. At Cornell, Lam joined the Computational Thermo-Fluids Lab, working on computational modeling and control of liquid-gas flows with a focus on spray atomization.

To my *father* – a phenomenal teacher – for spending countless hours teaching me the secrets of science and the importance of kindness.

To my *mother* – for her truly unconditional support. Thank you for changing my diapers, cooking, and cleaning for me for 27 years without a complaint.

To my *friends* on the west coast – for their willingness to seek adventure and their friendship despite the time difference. 3000 miles felt small.

To my *siblings* – for breaking my first tennis racket, thus forcing me to abandon my athletic talents for a lifetime of suffering in science.

To my *extended family* – my grandparents for their love, my uncles for being constant sources of inspiration and their limitless supply of arguably inappropriate jokes, my aunts for their delicious home cooked meals, and my cousins for being extra siblings to play games with.

ACKNOWLEDGEMENTS

I am indebted to my advisor, Professor Olivier Desjardins, for his encouragement, guidance, and infinite understanding and patience during my time as a clueless, procrastinating graduate student. I could not have asked for a better advisor. I am grateful for my committee members, Professor Gregory Bewley and Professor Mahdi Esmaily, for their willingness to discuss my research and their interesting lectures.

I am thankful for my friends at Cornell who have made these long years bearable. I cherish the memories we made in this strange place.

I am grateful for my lab mates – too many to name all – for sharing in the frustrations that come with research. Special thanks to Dr. Robert Chiodi for his technical support and advice in my early days in the lab.

I am extremely appreciative of all the talented researchers with whom I have been fortunate enough to collaborate with. Specifically, I would like to thank Professor Nathanael Machicoane for his experimental measurements and insights and our fruitful discussions, as well as Dr. Alexandru Fikl for the mathematical derivation of the adjoints and his willingness to share in my struggle with them.

There are many educators in my past for which this would not have been possible – my high school teacher, Mr. Orme, and my undergraduate professors, Prof. John Larue, Prof. Dimitri Papamoschou, and Prof. Roger Rangel.

I am grateful for Marcia Sawyer for fostering a sense of graduate community and the many happy hours she planned that fed a poor student.

This work was sponsored by the Office of Naval Research as part of the Multidisciplinary University Research Initiatives Program under grant number N00014-16-1-2617.

TABLE OF CONTENTS

LIST OF TABLES

LIST OF FIGURES

CHAPTER 1

INTRODUCTION

1.1 Motivation

With the ever-looming climate crisis, it has become more paramount than ever to take action on a large scale. The global temperature has risen nearly 1.8°F since the start of the Industrial Revolution, and much of that has been attributed to the burning of fossil fuels [13]. From $1910-1980$, the average rate of rise in temperature was 0.23°F per decade in North America alone. Since then, the average rate has more than doubled, reaching 0.52°F per decade - staggeringly, trends suggest further acceleration in the future [75]. Such rises in temperature have substantially impacted urban areas in recent years. California has experienced unprecedented arid climate conditions, irregular rain and snow patterns, and abnormal movements of vegetation, all of which have increased the frequency and intensity of the state's crippling wildfires [13]. In 2020, devastating wildfires ripped through the state, releasing more energy than any year in the past two decades by several factors, as seen in fig. 1.1a. These wildfires have had an invisible consequence in the form of planet-warming gas release, creating a viscous cycle [84]. In the city of Ithaca where Cornell University resides, the effect of the rising temperatures can readily be seen by the alarming decrease in annual snowfall in the past two decades, as shown in fig. 1.1b. Declining annual snowfall has potentially both environmental and human impacts, including the disruption of fish spawning in the spring and debilitating water shortages due to a lack of spring runoff supply [27].

Much of the rise in global temperature stems from greenhouse gas (GHG) emissions caused by industries in the economic sector such as agriculture, electricity,

and transportation. The transportation industry pertains to the movement of people and freight via passenger vehicles, ships, trains, and commercial airliners to name a few. Accounting for 27% of the total emissions, the transportation industry is the largest contributor of GHG emissions [28]. Although recent calls for clean transportation in the form of electric vehicles and bio-fuels are emerging, 90% of the transportation industry still relies on burning petroleum, namely gasoline and diesel, to power vehicles, thereby contributing a large amount to GHG emissions [28]. In addition to electric vehicles and bio-fuels, some techniques to mitigate emissions have involved investing in transit infrastructure to promote communal travel as well as urban planning to reduce travel distance. However, a more immediate and arguably far-reaching avenue for emissions reduction is to improve the efficiency of the combustion process by bettering the fuel atomization process, or more generally, spray atomization. To this end, we are motivated to: 1) improve computational modeling capabilities of spray atomization and gain confidence through experimental validation and 2) provide a novel computational framework for spray control.

On a broader scale, spray atomization appears in many other engineering applications outside of combustion. Spray drying is a technique that produces a fine powder by atomizing a liquid slurry to create a spray and rapidly dries it using a hot gas. This technique is utilized for powder metallurgy in additive manufacturing as well as the production of common household consumable powders such as Kool-aid, spice mixes for ramen and instant coffee [5]. In the medical field, spray drying is used for a variety of applications ranging from drug encapsulation important for drug delivery to the creation of bio compatible coatings for medical devices such as stents and catheters [93]. Sprays have also been used to coat wind turbine blades and the exterior of high-speed air-crafts so that they can operate

under difficult conditions. Furthermore, spray atomization is a facet that is pervasive in everyday life - a common sneeze, a sprinkler watering the lawn, and even the mist coming from a crashing ocean wave are all examples of spray atomization. Despite such ubiquity, modeling spray atomization presents significant challenges and much remains to be learned.

1.2 Background

Air-assisted (or air-blast) atomization utilizes gas flow to assist in breaking up a liquid jet. This type of atomization for combustion systems can be divided into three regions: the nozzle flow region, the spray formation region, and the spray dispersion region. In the nozzle flow region, separated streams of liquid and turbulent gas flow through a complex geometry. The spray formation region is just past the nozzle exit where the high-speed gas breaks up the low-speed liquid, creating a distribution of drops that form the spray. These drops are then dispersed in a complex, heavily drop-mediated flow around what is called the spray dispersion region.

Experiments have been used extensively to study spray atomization albeit with limitations. Experimental methods cannot easily quantify the flow inside the nozzle using standard particle image velocimetry (PIV) and hot-wire measurements. Optical imaging is one technique to quantitatively study the spray formation and dispersion region and yields near binary images of the liquid. Studies have successfully utilized this technique to quantify the intact length of the liquid, near-field wave characteristics, and dominant frequencies [e.g., [61, 64, 65, 57]]. However, these measurements are hinged upon unobstructed projections of the liquid. As

an example, in flow regimes where drops are stripped away from the liquid core, the dense spray creates an optical opaqueness wherein a contour of the main liquid body can no longer be distinguished. Under these conditions, measurements resort to using an ensemble of images to extract time-averaged measurements such as the spray cone angle. X-ray radiography is another technique to gather quantitative measurements but require highly specialized facilities and technical expertise, and therefore, have been a less common tool for studying spray atomization. This technique enables vision inside the liquid, allowing a wider range of physics such as bubble entrainment and contact line dynamics to be studied [4]. It has also been used to extract quantitative measurements such as the integrated liquid depth along a line of sight [15].

Simulations serve as a potentially powerful alternative to experiments as they can probe anywhere inside the flow; however, they are fraught with their own challenges. Some of these challenges include robust numerical methods capable of handling topology change, discontinuous fluid properties across the interface and singular forces at the interface, and computational demand owing to the wide range of length and time scales [37]. The simplest and cheapest computational models simulate the nozzle flow and spray dispersion region, and connect the two by using phenomenological models [77, 9, 89, 90, 47] to inject liquid blobs that undergo secondary break up and dispersion. More complex and expensive models simulate the spray formation process by solving for a liquid-gas mixture, thereby bypassing the difficulty of interface tracking and related discontinuities, limiting their physicality [104, 59]. The highest fidelity and most expensive models solve the complex two-phase immiscible Navier–Stokes equations and pour their computational resources on the spray formation region (e.g., [1, 33, 60]), forgoing the modeling of the nozzle flow and spray dispersion region. Although many com-

putational studies of spray atomization have been performed, the majority have been done as a stand alone study without experimental validation. For the studies that have been validated against experiments, simplifications were made such as simulating at lower density and viscosity ratios or relying mostly on qualitative comparisons and indirect quantities for quantitative comparisons.

Numerical frameworks for liquid-gas flow control are essentially non-existent. The optimization of dynamical systems can be conducted using several methods such as pattern search methods [46, 101], evolutionary algorithms [7], and machine learning through neural networks [3]. A major drawback of these methods is that they require many evaluations of the cost functional. In the current setting of PDE-constrained optimization, this involves expensive multidimensional unsteady large-eddy simulations (or similar), making them computationally strenuous. As such, gradient optimization appears as a powerful alternative as the number of cost functional evaluations can be better controlled. Adjoint methods pose the control problem as a minimization problem and calculate the gradient used in the gradient descent algorithm. Adjoint methods still face many challenges. For example, they require a complete model of the flow equations, the mathematical framework to adjoint the equations, and the numerical tools to perform the corresponding sensitivity calculations. All of these steps are highly non-trivial in a multiphase setting.

1.3 Contributions

In this dissertation, I present contributions I made to the field of spray atomization and computational control of liquid-gas flows. The contributions are summarized

as follows:

- A coaxial spray atomization simulation is performed at a low momentum flux ration, air-water conditions, and in a complex geometry. This simulation is validated against experiments by showing strong agreement of direct quantities obtained from back-lit imaging and rare X-ray focused beam measurements.
- The impact of the gas inflow model and the contact line model on spray statistics is carefully analyzed. Results show that the contact line model has a strong influence on the liquid distribution downstream. A sub-grid scale (SGS) static contact angle model is implemented and varied, quantifying the influence of nozzle tip wettability on spray statistics.
- A multi-scale simulation strategy is presented. This strategy uses multiple coupled domains to address the wide range in length scales, multiple sub-grid scale models to address unresolved scales and a thin structure break up model to explicitly model topology change. The thin structure break up model results in excellent agreement in drop size distributions. This strategy has the potential to be scaled up to industrially relevant applications. *The thin structure break up model requires the use of a connected component labeling algorithm developed by Austin Han and Professor Olivier Desjardins.*
- A numerical framework to perform adjoint based optimization of liquid-gas flows using a sharp interface model and its verification are presented. *The adjoint equations were derived by Dr. Alexandru Fikl and Professor Daniel J. Bodony.*
- A novel surface quantity transport scheme is presented as part of the adjoint framework and is generalizable to transport of other surface quantities such

as surfactants and electric charge.

- Liquid-gas flow control using the adjoint framework is demonstrated on a range of test cases including highly multi-dimensional control of the initial velocity profile to maximize growth of a temporally evolving liquid-gas mixing layer.

1.4 Organization

Chapters 2 to 4 are all manuscripts in preparation for submission and can be treated as stand alone documents. Chapters 2 and 3 focuses on advances in spray modeling and Chapter 4 focuses on the developments on adjoint based liquid-gas flow control.

Chapter 2 presents an in depth validation of the simulations against experiments at a low momentum flux ration, air-water conditions, and in a complex geometry. The influence of the gas velocity model, the contact line model, and static contact angle on spray metrics are quantified.

Chapter 3 presents a multi-scale simulation strategy that utilizes multiple domains and the corresponding governing equations, and coupling between the domains. A thin structure break up model is presented to model topology change and drop size distributions comparisons against experiments are shown.

Chapter 4 details the mathematical formulation and numerical implementation of the two-phase adjoint Navier–Stokes equations. The adjoint framework is verified by performing gradient checking exercises and demonstrated on a temporally evolving mixing layer, among other cases.

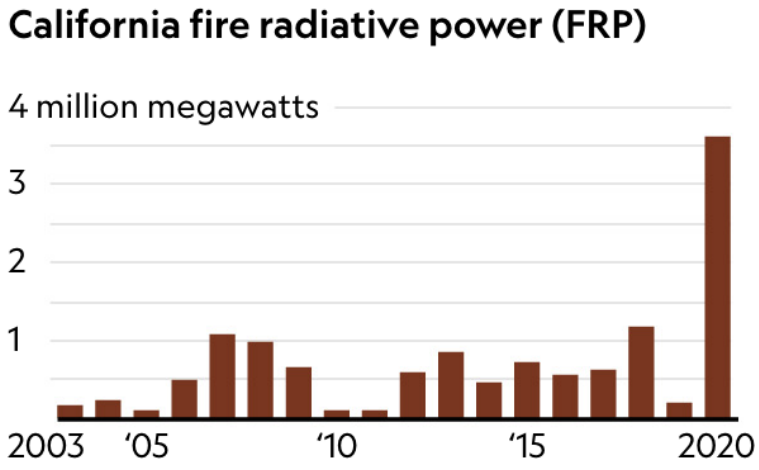

(a)

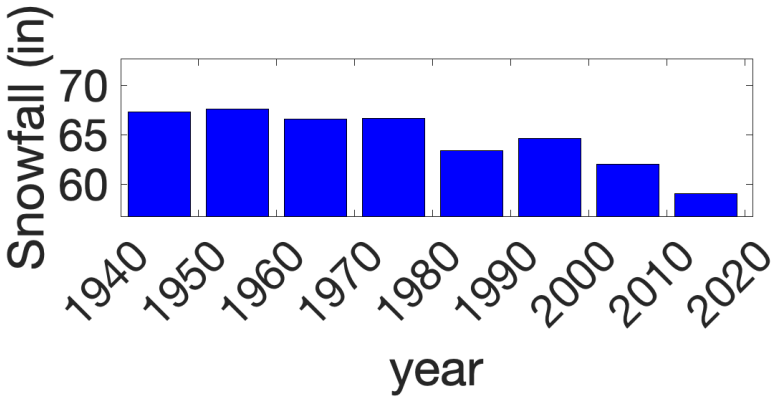

(b)

Figure 1.1: Impact of global temperature on urban areas: a) radiative power output from wildfires in CA [13] per year and b) annual snowfall in Ithaca over a 10 year average [18].

CHAPTER 2

A COMPUTATIONAL STUDY OF A TWO-FLUID ATOMIZING COAXIAL JET: VALIDATION AGAINST EXPERIMENTAL BACK-LIT IMAGING AND RADIOGRAPHY AND THE INFLUENCE OF GAS VELOCITY AND CONTACT LINE MODEL

2.1 Abstract

Numerical simulations of liquid atomization in a two-fluid coaxial geometry have been performed using a geometric Volume-of-Fluid method. Experimental measurements have been obtained using state of the art visible light back-lit imaging and X-ray radiography. Simulations are validated against experiments, using the same geometry and fluid injection rates of air and water, by showing excellent agreement in quantities such as equivalent path length of the liquid, liquid core length, and dominant flapping frequency. At the nozzle exit, coflowing liquid and gas streams are separated by a splitter plate. The liquid is laminar and modeled using a Poiseuille flow while the gas inflow model and the contact line model are varied. For the gas velocity models, the vorticity thickness has been shown to have a strong influence on the downstream liquid distribution. For the contact line model, pinning the interface to the inner wall of the splitter plate leads to an initial increase in the diameter of the liquid jet just downstream of the nozzle exit. In contrast, pinning to the outer wall of the splitter plate or allowing for a free moving contact line results in a monotonic decrease in the diameter of the liquid jet as the downstream distance is increased, as observed experimentally. A sub-grid scale contact line model based on a static contact angle is employed. The static contact angle is varied in the model, showing that the liquid remains intact

longer as the static contact angle is increased.

2.2 Introduction

Two-fluid coaxial atomizers utilize a high-speed gas stream to destabilize a coflowing low-speed liquid. These devices are widely used in engineering systems such as spray dryers and fuel injectors. Accurate modeling of the liquid jet's initial destabilization and break up is of the upmost importance as it serves as a starting point to how the resulting spray is dispersed. Because of the inherent difficulties associated with modeling primary atomization computationally [37], studies have mostly been limited to highly simplified and academic cases. Moreover, few studies have explored in detail the modeling of the nozzle exit. In particular, the impact of different modeling strategies for the high-speed gas, low-speed liquid, and the splitter plate separating the two streams, has not been carefully investigated.

Liquid atomization has been studied extensively both through experiments and simulations but have had limitations based on the methods used. A non-exhaustive list of such methods are described below along with some of their limitations. Experimentally, the flow inside the nozzle cannot be easily quantified using standard particle image velocimetry (PIV) and hot-wire measurements. Back-lit imaging is an effective technique for visualizing the spray and can be used to accurately extract quantitative measurements of the liquid in a region where the liquid stays mostly intact. However, measurements struggle in areas where the liquid is broken up and multiple liquid structures intersect a line of sight. In contrast, X-ray radiography enables vision through the liquid, enabling a wider range of physics such as bubble entrainment and contact line dynamics in extreme atomization conditions

to be studied. Recently, it has been used to extract quantitative measurements such as the integrated liquid depth along a line of sight [15]. Simulations have had their own challenges such as robust numerical methods capable of handling topology change, discontinuous fluid properties across the interface and singular forces at the interface, and computational demand owing to the wide range of length and time scales [37]. Front tracking methods [102], which transport a surface mesh are viable techniques but have difficulty with topology change as heuristics are needed for the deletion and re-population of surface elements. Diffuse interface methods [6] are also viable but diminish the sharpness of the discontinuities since the interface is smeared over a few computational cells. Level-set methods, which transport a signed distance function away from the interface, have been used extensively [98] but suffer from mass conservation issues. These issues have been addressed by improvements such as the conservative level set method [19] and the refined grid level-set method [43]. Volume-of-fluid (VOF) methods, using complex geometric transport operations [79], have had success in handling topology change, ensuring discrete mass conservation and maintaining the sharp discontinuities.

Validating simulations against experiments is a crucial step in computational studies of sprays and the majority of past validation exercises of two-fluid atomizers have compared indirect quantities or reduced the modeling complexity because of the computational and experimental challenges described above. Demoulin et al. [24] simulated primary break-up by solving equations for a single fluid representing a liquid-gas mixture under the assumptions of high Reynolds and Weber numbers and compared centerline liquid volume fraction profiles against experiments. Gorokhovski et al. [37] modeled the primary atomization by solving for the gas phase using a large eddy simulation (LES) and the liquid phase using a stochastic liquid depletion modeling. This study yielded satisfactory agreement

of liquid volume fraction distributions against experiments but most comparisons were qualitative. Fuster et al. [34] presented simulations at a lower viscosity and density ratio and compared droplet size distribution, as a function of mesh size, against experimental data. Fuster et al. [33] studied the influence of the splitter plate thickness on the peak frequency and made comparisons against linear stability analysis at low density ratio. For a single case, the frequency was compared against experiments and linear stability analysis at air-water conditions. The study showed that at low dynamic pressure ratios, a convective instability is observed whereas at high dynamic pressure ratios, the instability is absolute. Xiao et al. [109] simulated primary atomization at air-water conditions and showed great agreement in the liquid core length but generated the gas inflow using synthetic turbulence. This study showed the turbulent eddies in the liquid phase play a leading role on the interfacial instabilities. Muller et al. [74] simulated primary break up of a high viscosity fluid and showed great agreement in liquid core length and dominant frequency against experiments using the same geometry. Agbaglah et al. [1] presented 3D simulations in a planar geometry at experimental air-water conditions and compared well the liquid cone length and the most unstable frequency. This study showed that inclining the gas inflow enhanced the formation of liquid waves. Ling et al. [60] performed massively resolved simulations at a lower density and viscosity ratio and reported on droplet size distributions, as a function of mesh size, and compared them against log-normal and Gamma distributions fits. The simulations qualitatively discussed the expansion of punctured holes in liquid sheets and the ligaments generated at the edge of their rims. Carmona et al. [17] performed simulations of a pre-filmed air-blast atomizer and made qualitative comparisons and drop size comparisons as a function of VOF iso-surface value. Even with current studies, more detailed and direct comparisons under realistic

configurations are needed to validate computational capabilities.

In this study, we perform simulations of primary atomization in a coaxial two-fluid atomizer using the volume-of-fluid method and validate them against experiments. A novelty of our validation exercise is that we make direct comparisons of quantities obtained from experimental back-lit imaging and X-ray radiography under identical operating conditions, using the same geometry. Following the validation, we study the effect of using different gas inflow models which range from using an analytical velocity profile to an additional nozzle simulation. The liquid is laminar and modeled as a Poiseuille flow and a splitter plate separates the liquid and gas streams. We discuss the influence of the contact line model which ranges from pinning the interface to a specified location on the splitter plate to a free moving contact line. For free moving contact lines, we employ a sub-grid scale (SGS) contact line model that assumes a static contact angle [107]. We vary the static contact angle to understand the effect of nozzle tip wettability. These inflow modeling strategies are easily implementable and do not require large amounts of mesh resolution, making them particularly desirable from a practical engineering standpoint.

The Chapter is organized as follows: Section 2.3 discusses the experimental and numerical methods used, Section 2.4 validates our computational model against experiments, Section 2.5 discusses the influence of the gas velocity model, Section 2.6 discusses the influence of the contact line model, and conclusions are drawn in Section 2.7.

2.3 Methods

2.3.1 A canonical atomizer and flow conditions

A two-fluid coaxial atomizer [62], shown in fig. 3.1, is used in both simulations and experiments. Air enters the nozzle through 4 upstream ports perpendicular to the wall and flow through an annular passage at a total flow rate Q_g. Liquid water flows through a straight circular pipe at a flow rate Q_l. The outer wall of the liquid nozzle separates the two streams and its annular section at the exit plane, with inner and outer diameter $d_l = 2$ mm and $D_l = 3$ mm, will be referred to as the splitter plate. The liquid and gas bulk exit velocities are defined as $U_l = Q_l/A_l$ and $U_g = Q_g/A_g$, where $A_l = \pi d_l^2/4$ and $A_g = \pi(d_g^2 - D_l^2)/4$ are the liquid and gas nozzle exit flow through areas and $d_g = 10$ mm is the gas nozzle inner diameter. The fluids properties used are kinematic viscosities of $\nu_g = 1.45\ 10^{-5}$ m^2 s^{-1} and $\nu_l = 1.137\ 10^{-6}$ m^2 s^{-1}, densities of $\rho_g = 1.226$ kg m^{-3} and $\rho_l = 1000$ kg m^{-3}, and a surface tension coefficient $\sigma = 72$ mN m^{-1} where subscripts g and l denote gas and liquid properties respectively. Table 3.1 summarizes the non-dimensional parameters used in this case.

2.3.2 High-speed Back-lit Imaging and X-ray Radiography

High-speed back-lit imaging is used to produce 2D slices of the liquid presence in the near-field. The images are post-processed using a sequence of operations that binarize the liquid core, defined to be the portion of the liquid jet that is still fully connected to the nozzle, such that a liquid pixel value is 1 and a gas pixel value is 0. The temporal and spatial resolutions for this study are 0.1 ms and 27 μm

respectively. Details of this method are discussed further in [61].

Synchrotron X-ray radiography of the resulting spray was performed at the Advance Photon Source (APS) at Argonne National Laboratory, 7-BM beamline [52]. As opposed to binarized liquid data obtained from back-lit imaging, focused beam radiography enables the point-like measurement of the integrated liquid depth along a line-of-sight, referred to as the equivalent path length (EPL). The measurement technique begins with a monochromatic X-ray beam that is sent across the liquid and measured by a receiving pin-diode at 270kHz. Based on the attenuation of the signal caused by the impediment of the liquid, the EPL is deduced from Beer-Lambert's Law: $EPL = (1/\mu_a)\ln(I_0/I)$ where I_0 is the incident beam intensity, I is the beam intensity after passing through the spray, and μ_a is the X-ray attenuation coefficient. These point measurements can be raster-scanned across the spray to gather longitudinal or transverse profiles of the liquid depth. Details of this technique are further described in [15], and the experimental configurations and liquid phase visualization are detailed in [62].

2.3.3 Numerical methods

We consider liquid-gas flows governed by the incompressible Navier-Stokes equation

$$\frac{\partial \rho \mathbf{u}}{\partial t} + \nabla \cdot (\rho \mathbf{u}\mathbf{u}) = -\nabla p + \nabla \cdot \left(\mu\left[\nabla \mathbf{u} + \nabla \mathbf{u}^{\mathsf{T}}\right]\right) + \rho \mathbf{g}, \tag{2.1}$$

along with the incompressibility condition

$$\nabla \cdot \boldsymbol{u} = 0, \tag{2.2}$$

where $\mathbf{u}$ is the velocity, p is the pressure, $\mathbf{g}$ is the gravitational acceleration, and t is time. Fluid properties are constant within each phase but differ between the

phases. If Γ indicates the interface and $\left[\ \right]_\Gamma$ indicates the jump of a property across the interface, then the jump in density and viscosity across the interface are $\left[\rho\right]_\Gamma = \rho_l - \rho_g$ and $\left[\mu\right]_\Gamma = \mu_l - \mu_g$, respectively. The velocity is continuous across the interface, hence $\left[\mathbf{u}\right]_\Gamma = 0$, and the pressure jump across the interface is given by

$$\left[p\right]_\Gamma = \sigma\kappa + 2\left[\mu\right]_\Gamma \mathbf{n}^\mathsf{T} \cdot \nabla\mathbf{u} \cdot \mathbf{n}, \tag{2.3}$$

where σ is the surface tension coefficient, κ is the interface curvature, and $\mathbf{n}$ is the interface normal. The equations are solved using an in-house, conservative, finite volume flow solver for low Mach number flows [25]. The volume fraction transport equation

$$\frac{\partial\alpha}{\partial t} + \mathbf{u} \cdot \nabla\alpha = 0, \tag{2.4}$$

is solved with a geometric, semi-Lagrangian Volume-of-Fluid method [79] where α is the ratio of liquid volume to cell volume in a computational cell. The solver is second-order accurate in time and space and away from the interface, is discretely kinetic energy conserving. At the interface, local discontinuities degrade the methods and although mass is still discretely conserved and momentum is nearly conserved, kinetic energy is not conserved. Inside each computational cell, the interface is represented locally as a plane using the piece-wise linear interface construction (PLIC) [92], with the plane normal calculated using LVIRA [85]. The curvature of the interface is calculated using parabolic surface fits [95]. The pressure jump due to this curvature is then embedded as a source term in the pressure Poisson equation using a continuous surface force approach [87]. To capture subgrid scale (SGS) effects, a dynamic Smagorinsky turbulence model [70] and SGS contact line model [107] assuming a static contact angle, θ_s, are employed. Figure 2.2 shows a schematic of a grid cell that contains the triple contact point. In that cell, the mismatch between the interface angle resolved by the mesh (θ_d) and

the angle at the wall (θ_s) are used to compute a SGS curvature

$$\kappa_{SGS} = \frac{\cos\theta_s - \cos\theta_d}{\Delta}, \tag{2.5}$$

where Δ is the mesh spacing. This is then added to the resolved curvature ($\kappa_{resolved}$) to compute an updated curvature

$$\kappa = \kappa_{resolved} + \kappa_{SGS}. \tag{2.6}$$

2.3.4 Simulation Set up

Domain

The atomization domain is a rectangular box of size $11.16D_l \times 10D_l \times 10D_l$, discretized on a Cartesian mesh uniformly spaced by $n_x \times n_y \times n_z$ cells in each direction respectively. Cells are cubic with sides of length $\Delta/d_l = 0.066$. x is the downstream direction while y and z are the lateral directions with the origin of the domain located at the centerline of the nozzle exit. The liquid is laminar and given a parabolic velocity profile. The gas inflow condition is either specified by a Dirichlet condition according to an analytical profile or a supplementary nozzle simulation. All other boundaries are treated as Neumann outflow conditions.

In a specific atomization simulation, an auxiliary nozzle simulation of the internal gas flow of the nozzle is used to generate realistic inflow conditions. The domain size of this nozzle simulation is $10d_g \times 10d_g \times 10d_g$ and the mesh is Cartesian with a uniform spacing $\Delta_n/d_g = 0.05$. The nozzle plenum is the furthest point upstream in the domain and the furthest point downstream is a distance d_g past the nozzle exit. The liquid injection is masked out as a solid and a single-phase solver

is used, significantly reducing the computational cost. The converging nozzle walls are created by stair-stepping full cells that are treated as solid boundaries and the gas inflow is injected through the 4 normal ports upstream to match the gas flow rate Q_g. All other boundaries are treated as Neumann outflow conditions. The gas velocity field at $x = -1.16D_l$ is then used as a Dirichlet inflow condition for the atomization simulation.

Range of Gas Velocity and Contact Line Models

The gas velocity models used in this study are an analytical velocity profile and an additional nozzle simulation of the internal gas flow. The analytical profile used is

$$\mathbf{u} = \begin{cases} U_g \mathrm{erf}\big((r - R_l)/\delta_w\big)\big[1 + \mathrm{erf}\big((r - R_l)/\delta_w\big)\big]/2, \\ 0, \qquad\qquad R_l \le r \le r_g \\ 0 \end{cases} \tag{2.7}$$

where $R_l = D_l/2$ and $r_g = d_g/2$ are the lower and upper bounds containing the gas stream, δ_w is the prescribed gas vorticity thickness and U_g is chosen such that the flow rate integrates to Q_g. Figure 2.3a shows an atomization simulation run with an analytical gas velocity profile while fig. 2.3b shows a simulation where the nozzle and atomization simulations are coupled as described in Section 2.3.4.

The contact line models used in this study were pinning the contact line to the inner wall, d_l, pinning to the outer wall, D_l, and allowing for an unpinned/free moving contact line. The implementation of each is as follows: when pinning to d_l, the splitter plate is modeled a fully unwet wall while when pinning to D_l, it is modeled as a fully wet wall. In both cases, the splitter plate cells are treated as a solid boundary for the velocity solver, but either taken to be a full liquid or gas

cells when included in the LVIRA interface reconstruction. However, in the case where the contact line is free moving, the splitter plate cells are excluded from the LVIRA interface reconstruction but still treated as a solid boundary for velocity. For free moving contact lines, the sgs contact line model described in Section 2.3.3 is employed. It should be noted that although the splitter plate is resolved by 2-3 cells in this study, results presented in the following section show that excellent agreement with experiments is still obtained. More detailed analysis of the contact line in a highly resolved setting is left for future work.

2.4 Validation Against Experiments

The combination of using an additional nozzle simulation to model the gas profile and allowing for a free contact line with a static contact angle of 85° yields the best agreement against experiments; qualitative comparisons are made in fig. 2.4 and quantitative comparisons are made against X-ray measurements in fig. 2.5 and against back-lit imaging in fig. 2.6. The atomization simulation presented in this section uses a refined mesh of size $\Delta/2$.

Figure 2.4 show snapshots of the flow comparing simulations and experiments; emphasis is placed on the liquid core which is defined to be the large coherent liquid structure attached to the nozzle. At this low momentum flux ratio, the main instabilities observed are Kelvin-Helmholtz instabilities that develop just past the nozzle exit and a large-scale flapping instability. At large scales, both exhibit similar liquid core lengths, interface topology, and flapping motion. The three snapshots illustrate the small-scale event of bag break-up. The process begins with the development of a thick sheet, the high-speed gas subsequently inflates this

sheet which forms a bag, and finally, when the sheet becomes sufficiently thin, the bag burst. These thin sheets in the experiment can reach scales as small as $\mathcal{O}(1\mu\text{m})$ which computations cannot afford to resolve. In our simulations, the mesh sizes are $\mathcal{O}(100\ \mu\text{m})$ and as such, bags prematurely break and leave behind large rims resembling a prong. Running at these mesh sizes allow simulations to be relatively affordable, costing around 100,000 core hours.

Quantitative comparisons of EPL statistics, liquid core length, and dominant frequency are presented to validate simulations against experiments. EPL is calculated in the simulations by integrating the volume fraction along a line of sight, i.e. $\text{EPL} = \int \alpha dz$. After the flow has reached a statistically stationary state, statistics are accumulated for $T_{stat} = 113 d_l/U_l$, i.e. 113 characteristic liquid time scales, while experimental measurements are gathered over 10 seconds. Figure 3.7a shows a 2D map of EPL averaged in time. Figure 3.7b shows the comparison of mean EPL sampled along x, at the centerline ($y = 0$). The mean centerline EPL gives a measure of the approximate liquid diameter at distances close to the nozzle and decreases in value downstream either because the flapping instability has placed the liquid core away from the line of sight or the liquid core has deformed or fragmented. Simulations are in excellent agreement with experiments as they are able to match well the centerline decay of mean EPL. Figure 3.7c show that simulations also match well the experimental standard deviation (std) of centerline EPL. Peaks in the std of EPL occur where variations in the integrated volume fraction over time are largest and in the case of the centerline EPL, are visually confirmed to be a result of large-scale flapping motion. Figures 3.7d to 3.7k shows excellent agreement in transverse EPL statistics. Figures 3.7d to 3.7g show that simulations match the transverse mean profiles well, capturing the spreading of the liquid jet. Figure 3.7h show two peaks in the std transverse profile at the top and bottom

edges of the jet and can be explained by the variation in volume fraction caused by interfacial perturbations generated by Kelvin-Helmholtz instabilities [65, 91]. Figures 3.7i to 3.7k shows that as the downstream distance is increased, the centerline value and the two off-center peaks also increase, indicating a transition from a surface Kelvin-Helmholtz instability to a large scale flapping instability.

Figure 2.6a shows a time instance of a binarized image of the liquid core and mimics an experimental back-lit image. The quantities illustrated on the figure are the liquid core length (L_B), defined to be the instantaneous longitudinal extent of the liquid core, and the y liquid barycenter (y_{bary}) at a downstream location. Figure 2.6b shows that simulations exhibit great agreement in the normalized probability density functions (PDF) of L_B over time. Figure 2.6c shows a spectrum of a Fourier transform taken of a time signal of y_{bary} at $x/D_l = 3$ (see [51] for more details). A flapping Strouhal number is calculated through $\mathrm{St} = f_{dom} d_l / U_g$ where f_{dom} is the dominant frequency taken to be the frequency at which the spectrum peaks. Note that this normalization does not comment on any physical scaling but is done for non-dimensionalization purposes. Table 2.2 summarizes the comparison of the mean and std of L_B and the flapping Strouhal number between simulations and experiments.

We now look at the effect of mesh resolution on the statistics presented above. Two additional simulations using larger mesh resolutions Δ and 2Δ are presented. Figure 2.7 show the mean and std centerline EPL statistics and the PDF of liquid core length at these different mesh sizes. mean and std centerline EPL statistics indicate that a simulation with a mesh resolution Δ is relatively well converged because differences between Δ and $\Delta/2$ are small compared to differences between 2Δ and Δ. Furthermore, fig. 2.7c shows that the liquid core length is not strongly

affected by the mesh size. Although discrepancies are still present in statistics between mesh sizes Δ and $\Delta/2$, we conclude that a mesh size Δ is sufficient to draw inferences from. As such, to reduce computational resources, future simulations presented will maintain a mesh size of Δ.

2.5 Impact of Gas Velocity Model

2.5.1 Gas Velocity Profiles

Figure 2.8 shows velocity profiles at the nozzle exit plane for the experiment, the auxiliary nozzle simulation and the analytical velocity profiles according to eq. (2.7) at different vorticity thicknesses. For the analytical profiles, the vorticity thicknesses used are $2\delta_w$, δ_w and $\delta_w/2$ where $\delta_w = 5.6h/\sqrt{Re_h}$ is the vorticity thickness obtained from the correlation proposed by [65], $h = (D_l - d_g)/2$ and $Re_h = U_g h/\nu_g$ and no turbulent fluctuations are added. The experimental gas velocity profiles were measured a small distance downstream of the nozzle using hot-wires without any liquid present while the statistics in the simulation were sampled in the atomization domain. Various mesh sizes of the auxiliary nozzle simulation were tested and minimal changes in the stream-wise velocity statistics were observed. Figure 3.6a shows that the mean stream-wise velocity profile of the nozzle simulation and $\delta_w/2$ analytical profile match the experimental vorticity thickness at the inner wall while the vorticity thicknesses of δ_w and $2\delta_w$ are larger. Figure 3.6b shows that the stream-wise std velocity predicted from the nozzle simulation match the experiments well at the inner wall, which can be expected to be most relevant for atomization, but are under-predicted within the outer gas

shear layer.

2.5.2 Influence of Vorticity Thickness

Figures 2.9a and 2.9b shows the mean and std centerline EPL and fig. 2.9c shows the liquid core length PDF of simulations using an analytical velocity profile at three different gas vorticity thicknesses (i.e. $2\delta_w$, δ_w and $\delta_w/2$). The contact line model used in these simulations is a free contact line with a static contact angle 85°. The simulation presented in Section 2.4 using a mesh size $\Delta/2$ will serve as a benchmark. Considering the simulation using a gas vorticity thickness δ_w, the mean centerline EPL profile and liquid core length PDF have larger values compared to the benchmark case, suggesting that the jet remains coherent longer. Reducing the vorticity thickness by a factor of 2 more closely matches the vorticity thickness produced from the nozzle simulation used in the benchmark case and therefore, we observe better agreement in the mean centerline EPL profile. However, discrepancies still remain as the std centerline EPL for $x/D_l > 3$ and the liquid core length PDF exhibits larger values. This is likely attributed to the turbulence coming from the nozzle which is known to have a destabilizing effect [50]. Mean centerline EPL statistics and liquid core length for $2\delta_w$ have much larger values than all cases, confirming that increasing vorticity thickness increases the liquid core length. Table 2.3 summarizes the mean and std liquid core length and and the flapping Strouhal number. Results show that decreasing the vorticity thickness decreases the mean liquid core length while increasing the dominant frequency. The latter is a trend consistent with past studies [33, 66] and related to studying the influence of gas velocity deficits on frequencies [66, 67]. However, using an analytical profile seems to under-predict the flapping Strouhal number

by $\approx 30\%$ under the range of vorticity thicknesses presented here. This is further evidence that turbulent fluctuations play a key role on the dominant frequencies [50, 68].

2.6 Impact of Contact Line Model

2.6.1 Effect of Contact Line Location

The contact line model is varied by pinning the contact line to the splitter plate inner wall, outer wall and allowing for a free moving contact line with a static contact angle of 85°. The gas flow model is maintained as an analytical velocity profile according to eq. (2.7) with a vorticity thickness δ_w.

Pinning the interface to the inner wall models the splitter plate as a fully unwet wall. This contact line model creates a gas re-circulation and low pressure region just downstream of the splitter plate. This gives rise to aspiration of the interface in the radial direction towards the gas. The consequence of this is observed in fig. 2.10a where the initial mean EPL increases as the downstream distance is increased. It is only after $x/D_l \approx 0.25$, that the interface reaches the bulk of the high-speed gas stream and subsequently exhibits a monotonic decrease in mean EPL.

Pinning the interface to the outer wall models the splitter plate as a fully wet wall. Experimental X-ray imaging have shown that at this operating condition, the contact line lies mostly near the outer wall [41, 91]. Moreover, when adding swirl to the gas, it is observed that the contact line can even wick up into the gas flow

region as shown in fig. 2.12a. Therefore, pinning to the outer wall more closely matches the local experimental flow configuration. This pinning model results in a mean centerline EPL that decreases monotonically which is experimentally observed (see fig. 3.7b).

Using a free contact line with an sgs contact line force with $\theta_s = 85^\circ$ leads to similar EPL profiles to pinning to the outer wall. Figure 2.12b shows the PDF of the normalized radial location for the contact line such that a value of 0 indicates the interface is located at the inner wall while a value of 1 indicates it is at the outer wall. The figure shows that for $\theta_s = 85^\circ$, the contact line radius peaks near the outer wall, serving as an explanation of why pinning to the outer wall and this free contact line have similar EPL profiles.

Figure 2.10c shows the PDF of the liquid core length and table 2.4 summarizes the mean and std centerline EPL and St for all three cases. Pinning to the inner wall leads to a liquid that is too stable as quantified by the large mean liquid core length and at times, the liquid core length is observed to exceed the domain boundary. Pinning to the outer wall and having a free contact line have similar PDFs, with the free contact line exhibiting a slightly smaller mean liquid core length. Studies have shown that the vorticity thickness has a strong impact on the dominant frequency [33, 66]. Results show that the flapping Strouhal numbers are all within 2% of each other, suggesting that the dominant frequency is independent of the contact line model for a fixed vorticity thickness.

2.6.2 Effect of Static Contact Angle θ_s

The static contact angle depends on many factors such as surface roughness, temperature, nozzle material and treatment. For aluminum, water and air, a reasonable static contact angle is between $70° - 90°$ [111, 63]. In the present study, we consider the static contact angles 70°, 85°, and 110° which model a moderately hydrophylic, less hydrophylic, and moderately hydrophobic surface respectively. In these simulations, an auxiliary nozzle simulation was used as the gas inflow model. Figure 2.12b shows the contact line radius PDFs measured at a fixed arc location. The PDFs show that the contact lines sit very close to the outer wall for $\theta_s = 70°$, further away from the outer wall for $\theta_s = 85°$ and near the inner wall for $\theta_s = 110°$. Figure 2.11a shows the mean and std centerline EPL profiles for simulations using these static contact angles. Because a simulation using $\theta_s = 110°$ results in a contact line close to the inner wall, its EPL profile follows a similar behavior to pinning to the inner wall, with an initial increase in EPL and subsequent monotonic decrease. Similarly, a simulation using $\theta_s = 70°$ results in a contact line close to the outer wall and as such, exhibits a behavior similar to pinning to the outer wall in that a monotonic decrease in EPL is observed. Figure 2.11b shows that increasing θ_s shifts the std centerline EPL to the right. Figure 2.11c shows the PDFs of the liquid core length for simulations using $\theta_s = 70°$ and 85° are similar while 110° results in a profile shifted to the right. Table 2.5 summarizes the mean and std centerline EPL and flapping Strouhal number showing that as θ_s is increased, the liquid core length and dominant frequency also increase.

2.7 Conclusion

In this study, we have performed simulations of air-blast atomization in a coaxial two fluid atomizer using a geometric volume-of-fluid method. Simulations were validated against experiments under identical air/water conditions and geometries. Excellent agreement of quantities such as the mean equivalent path length of the liquid (EPL), liquid core length, and dominant frequency was observed. A mesh refinement study was also conducted showing that these quantities were reasonably well mesh converged. The liquid was modeled using pipe flow while the gas inflow and contact line models were varied.

The gas inflow models considered were analytical velocity profiles at different vorticity thicknesses with no turbulent fluctuations added and an auxiliary nozzle simulation. Simulations using analytical velocity profiles were benchmarked against a simulation using the nozzle simulation. Results showed that decreasing the vorticity thickness decreased the mean liquid core length, the mean centerline EPL, and increased the dominant frequency. While one analytical profile had a vorticity thickness that was close in value to the experiment and nozzle simulation, quantities such as the mean liquid core length remained larger. Furthermore, although decreasing the vorticity thickness increased the dominant frequency, a trend reported in other studies [33, 66], the dominant frequencies for the presented vorticity thicknesses yielded systematically lower values than the experiment. These results confirmed that turbulent fluctuations in the gas play an important role. However, results indicated that the vorticity thickness plays a leading role compared to the turbulent fluctuations.

The contact line models considered were pinning to the inner wall of the splitter plate, the outer wall of the splitter plate, and allowing for a free contact line with

a (SGS) contact line model using a static contact angle of 85°. This study showed that the contact line model has a key influence on the liquid jet development and on the liquid distribution downstream. In particular, pinning to the outer wall or using a free moving contact line yielded better experimental agreement of quantities such as mean and std centerline EPL and mean liquid core length than pinning to the inner wall. Pinning to the inner wall resulted in an immediate increase in mean centerline EPL downstream of the nozzle because of a re-circulation region created by the gas. In contrast, pinning to the outer wall or having a free moving contact line resulted in the monotonic decrease in EPL observed in the experiments. Results also indicated that when using an analytical gas velocity profile with a fixed vorticity thickness, the contact line model does not have a significant impact on the dominant frequency. The static contact angle was varied between $\theta_s = 70°$, $\theta_s = 85°$, and $\theta_s = 110°$. Results showed in the $\theta_s = 70°$ case, i.e. modeling a hydrophylic surface, the mean centerline EPL exhibited similar trends to pinning to the outer wall while in the $\theta_s = 110°$ case, i.e. modeling a hydrophobic surface, trends were similar to pinning to the inner wall.

As the near-field region has been validated in this study and a better understanding of the impact of the gas velocity and contact line models have been gained, several research questions remain open. Since computational tools now result in strong agreement of liquid distribution compared against experiments, our research efforts will now shift to modeling the conversion of broken liquid structures in atomization simulations to Lagrangian particles in spray dispersion simulations. Promising research efforts have been made in this direction (e.g. [53, 100]). The inflow modeling of the gas has been studied in various forms which include modeling the velocity profile just downstream the nozzle exit using a velocity deficit (e.g. [66, 67]). However, current literature has not considered in detail the influence of

the contact line which this study has shown to have an impact. Thus, a more detailed study of the contact line physics and different modeling strategies for the contact line would be useful.

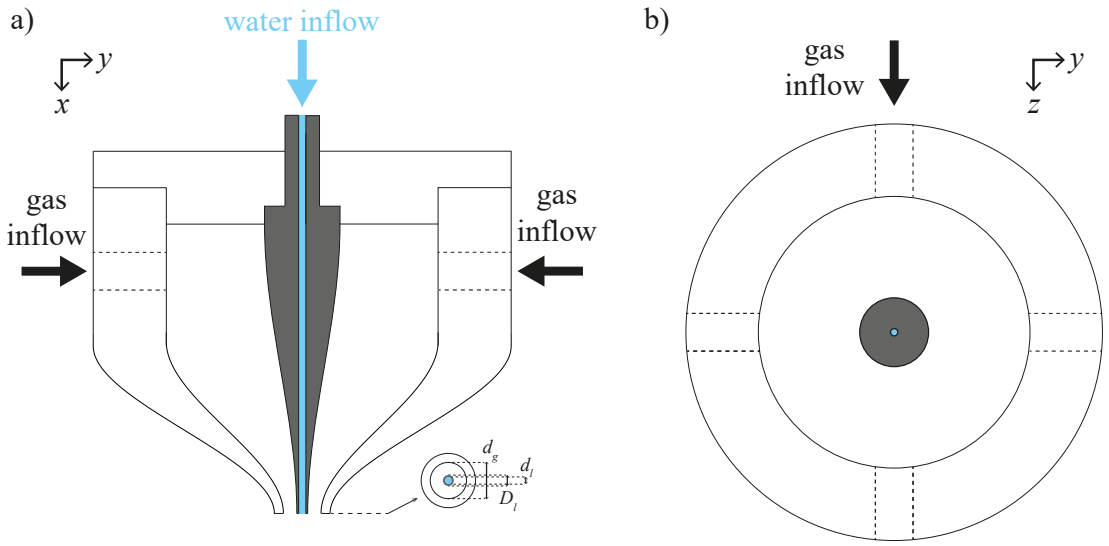

Figure 2.1: Nozzle schematic cut longitudinally (left) and transversely (right). Water is injected through a round pipe while gas is injected through 4 gas ports into a converging gas plenum with cubic-spline shaped inner and outer walls. A transverse cut at the exit plane is provided in the bottom right corner of (a), where the splitter plate is high-lighted in gray.

Table 2.1: Simulation's non-dimensional parameters: gas Reynolds number (Re_g), liquid Reynolds number (Re_l), momentum flux ratio (M), Weber number (We), density ratio (ρ^*) and viscosity ratio (μ^*).

$Re_g \equiv \frac{4Q_g}{\sqrt{4\pi A_g}\nu_g}$	$Re_l \equiv \frac{\rho_l U_l d_l}{\mu_l}$	$M \equiv \frac{\rho_g U_g^2}{\rho_l U_l^2}$	$We \equiv \frac{\rho_g (U_g - U_l)^2 d_l}{\sigma}$	$\rho^* \equiv \frac{\rho_l}{\rho_g}$	$\mu^* \equiv \frac{\mu_l}{\mu_g}$
21400	1200	6.4	39.1	815	65

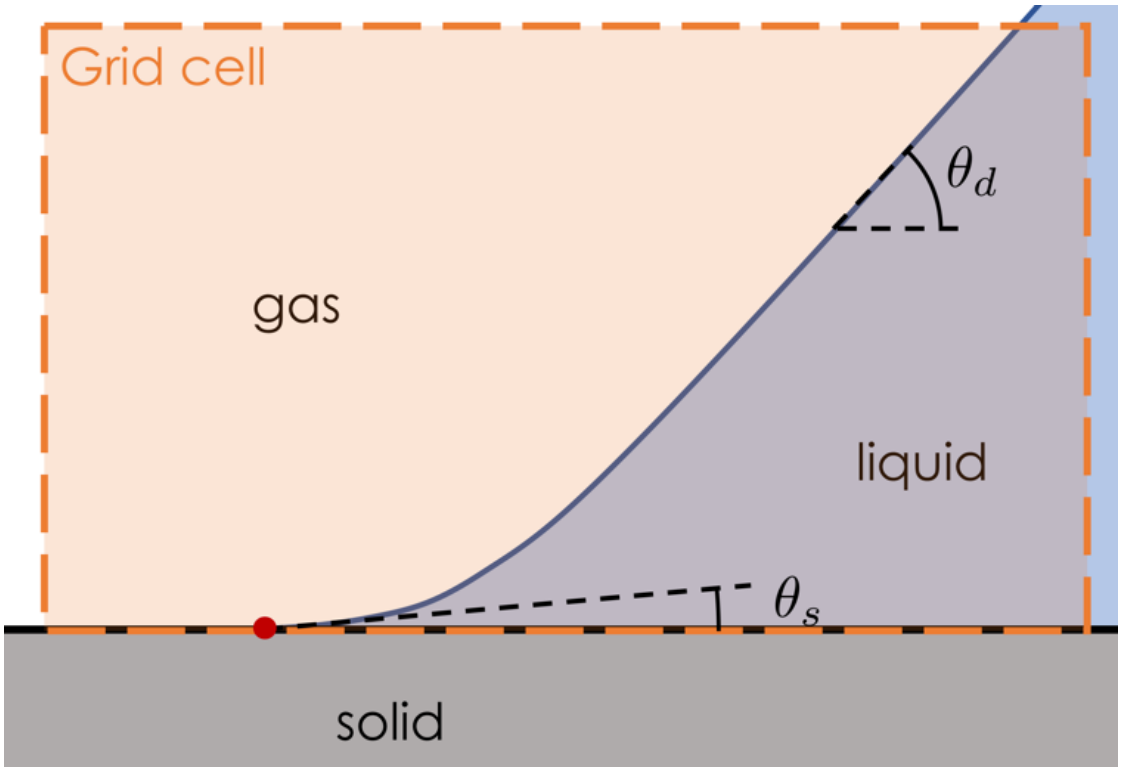

Figure 2.2: Schematic of sub-grid scale contact line model. The model adds a sub-grid scale curvature based on an assumed static contact angle θ_s to the resolved curvature based on θ_d.

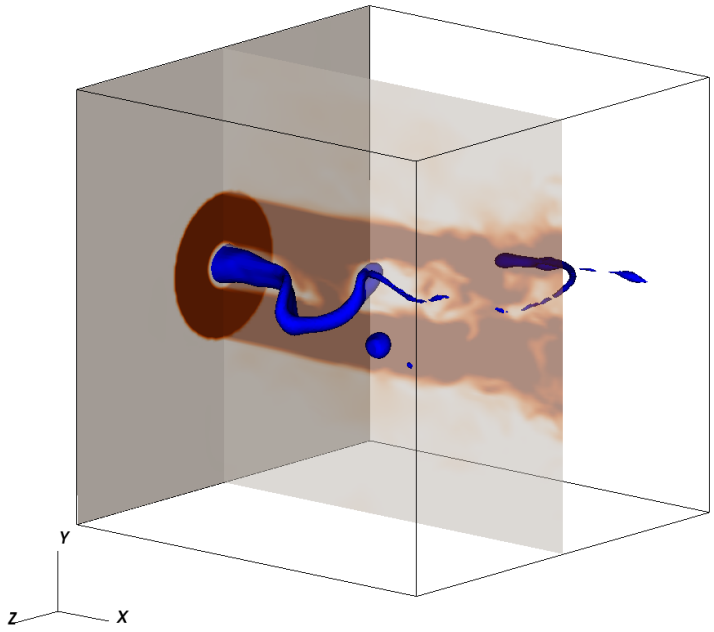

(a) Atomization Domain Only

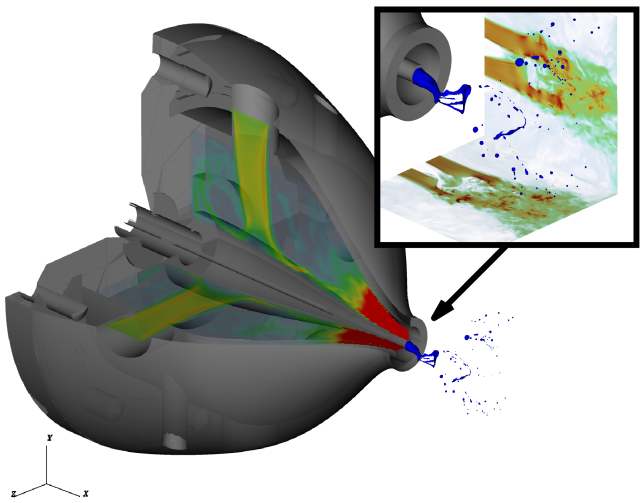

(b) Atomization and Nozzle Domains Coupled

Figure 2.3: Illustration of computational set up. a) Domain excludes the nozzle and utilizes an analytical profile to model the gas velocity and b) a separate nozzle simulation supplies gas velocity inlet conditions for the atomization simulation.

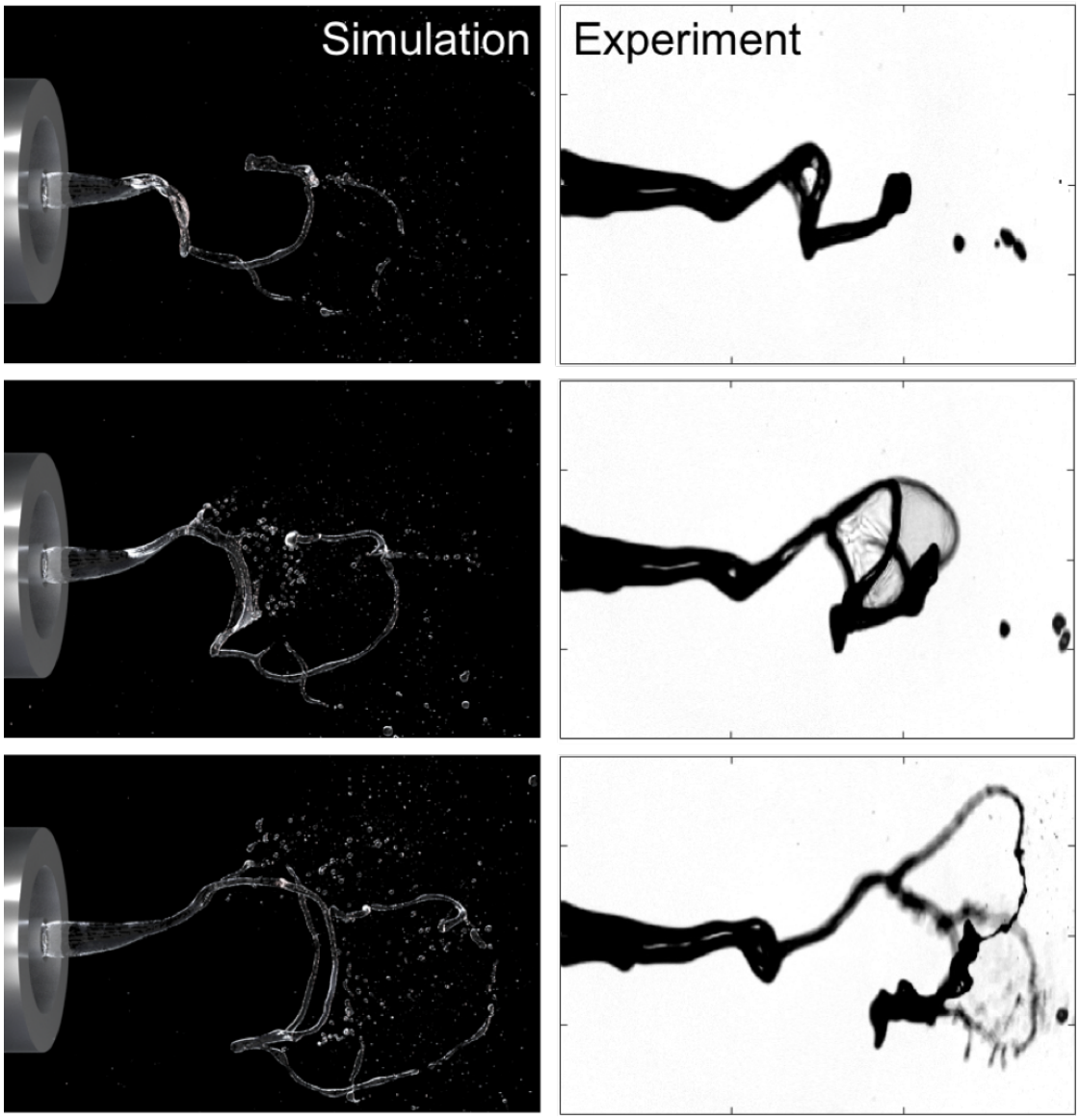

Figure 2.4: Qualitative comparisons between simulations (left) and experiments (right). Frames are separated by 1 ms.

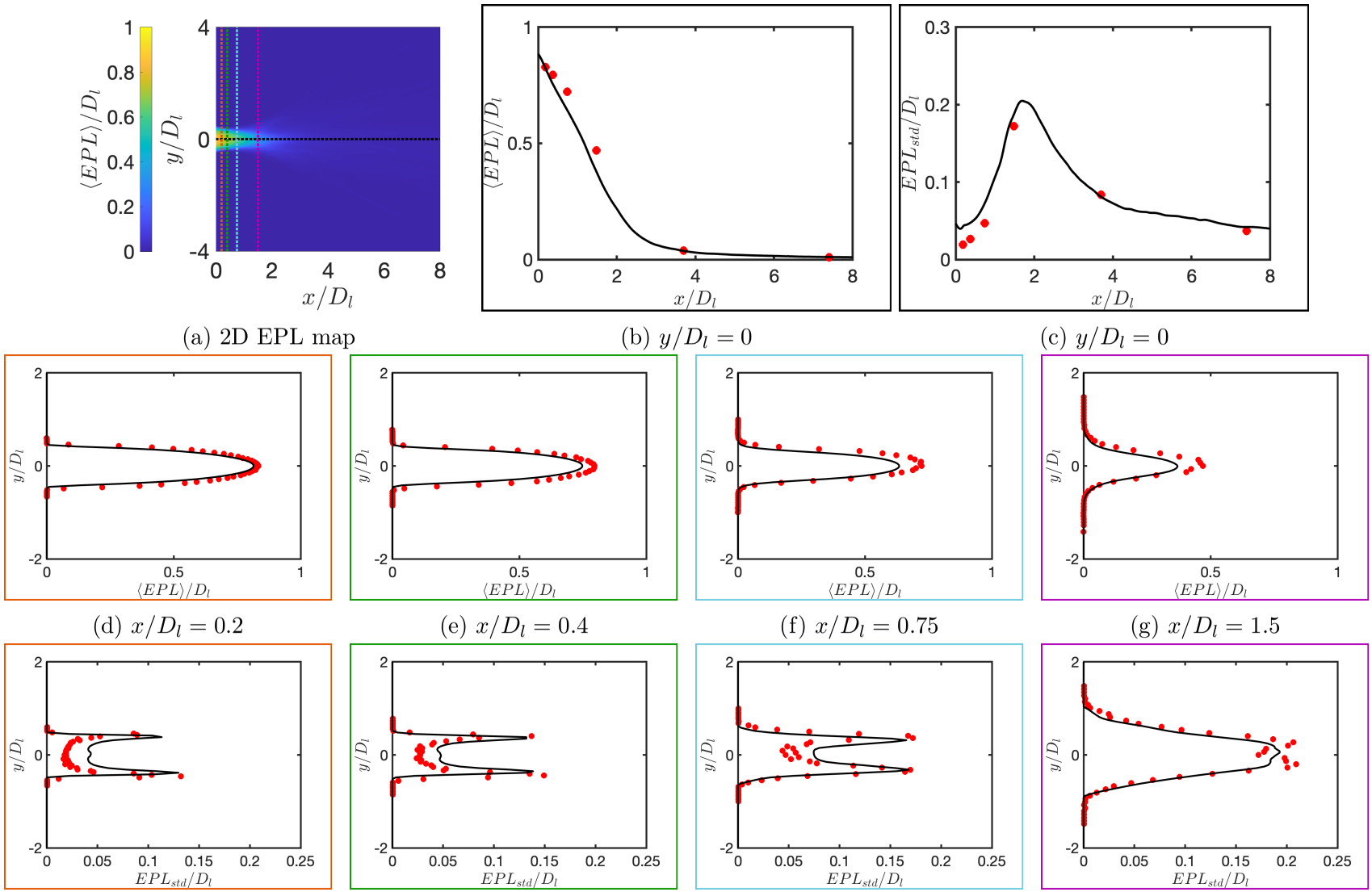

(a) 2D EPL map (b) $y/D_l = 0$ (c) $y/D_l = 0$

(d) $x/D_l = 0.2$ (e) $x/D_l = 0.4$ (f) $x/D_l = 0.75$ (g) $x/D_l = 1.5$

(h) $x/D_l = 0.2$ (i) $x/D_l = 0.4$ (j) $x/D_l = 0.75$ (k) $x/D_l = 1.5$

Figure 2.5: Simulation compared against experiments. a) 2D EPL map with sampling locations marked, b-k) EPL comparisons between simulations (—) and experiments (●).

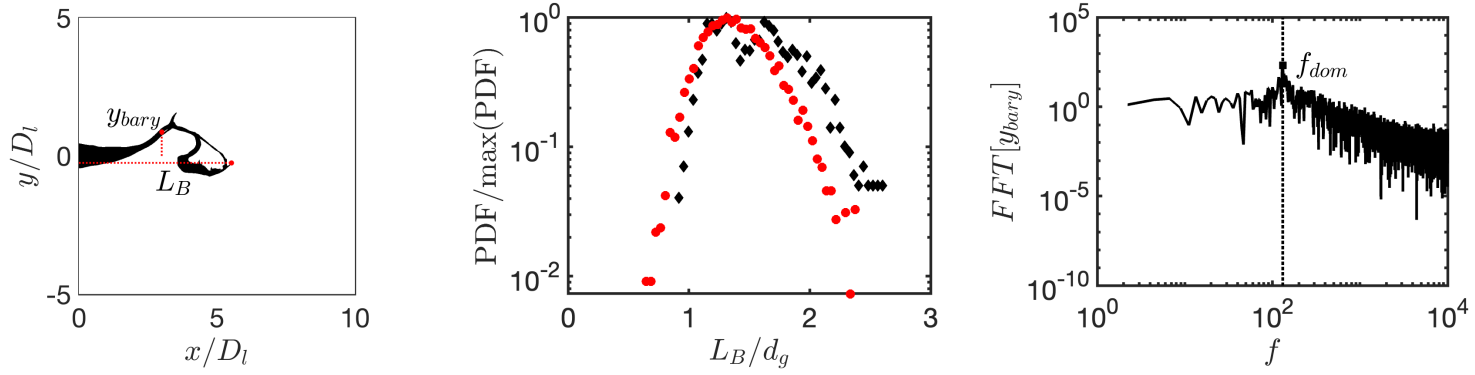

Figure 2.6: Simulation compared against experiments. a) Binarized image of the liquid core with relevant quantities, b) normalized PDF of liquid core length comparing simulations (♦) and experiments(●), and c) sample spectrum at $x/D_l = 3$.

Table 2.2: Summary of metrics from back-lit images

	$\langle L_b \rangle / d_g$	L_{std}/d_g	$f_{dom}\,(Hz)$
Simulation	1.57	0.346	127.6
Experiment	1.40	0.281	113.8
Normalized Difference	12%	23%	13%

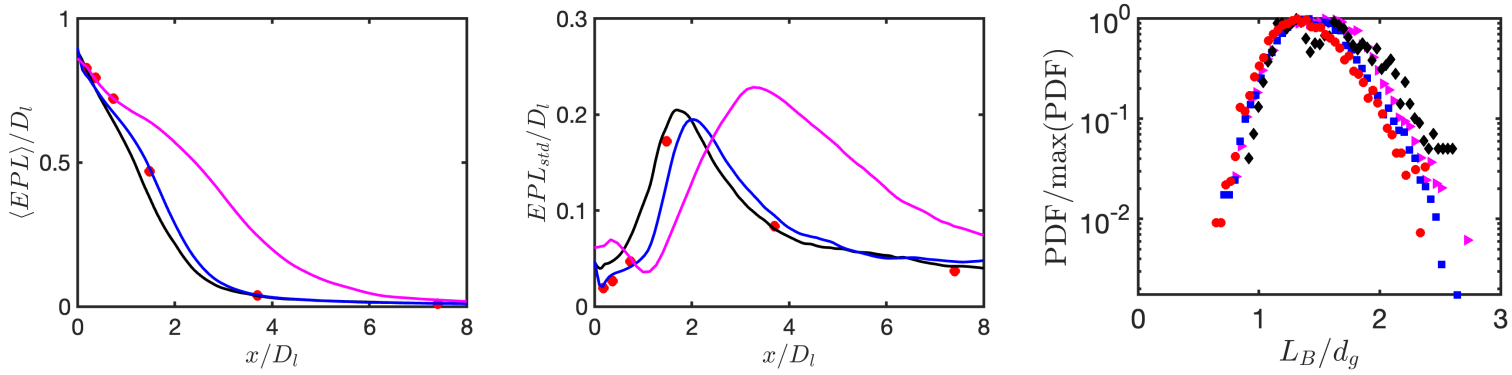

(a) $y/D_l = 0$ (b) $y/D_l = 0$ (c)

Figure 2.7: Mesh convergence of a-b) EPL statistics and c) liquid core length PDFs for simulations with mesh sizes 2Δ (— ▲), Δ (— ■), $\Delta/2$ (—, ♦),compared against experiments (●).

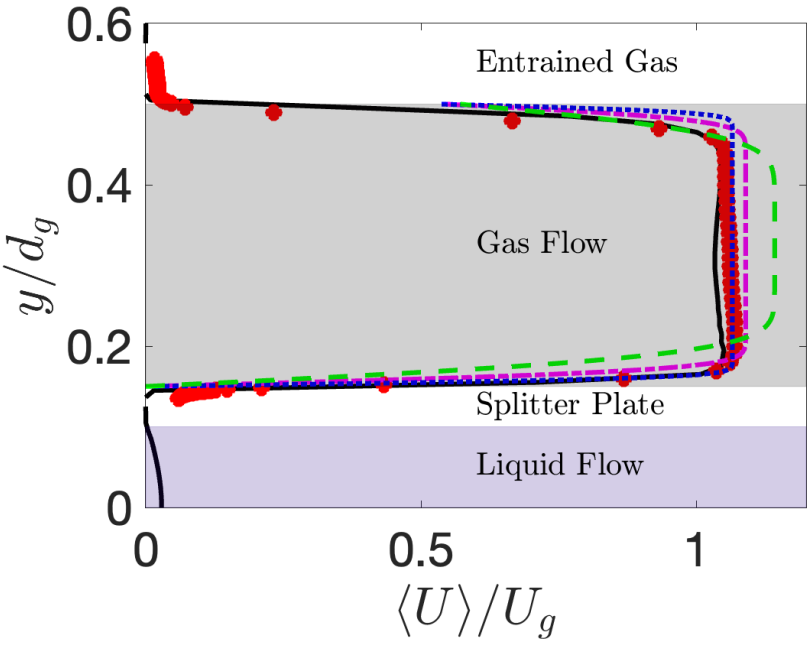

(a)

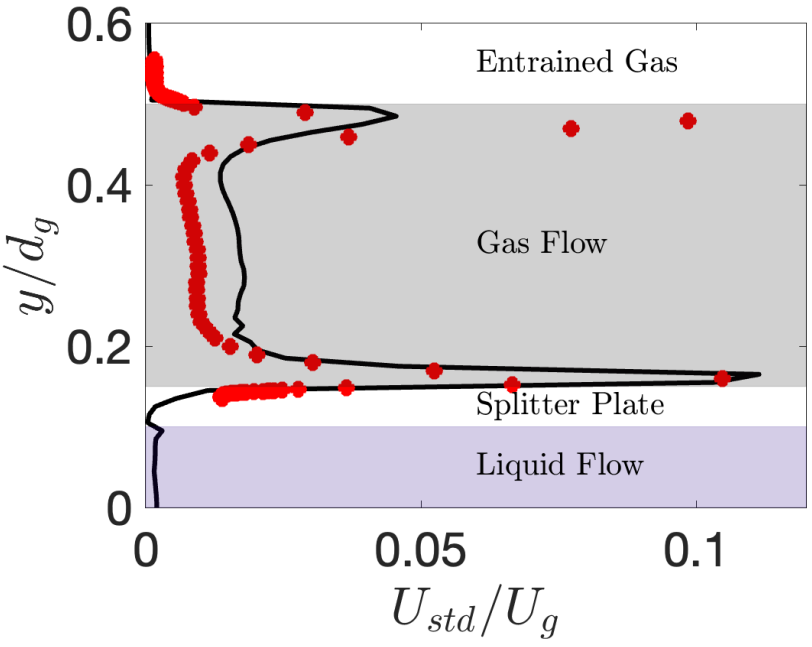

(b)

Figure 2.8: Comparisons of velocity statistics between analytical profiles with vorticity thicknesses $2\delta_w$ (- -), δ_w (-·-), $\delta_w/2$ (····), additional nozzle simulation (—) and experiment (●).

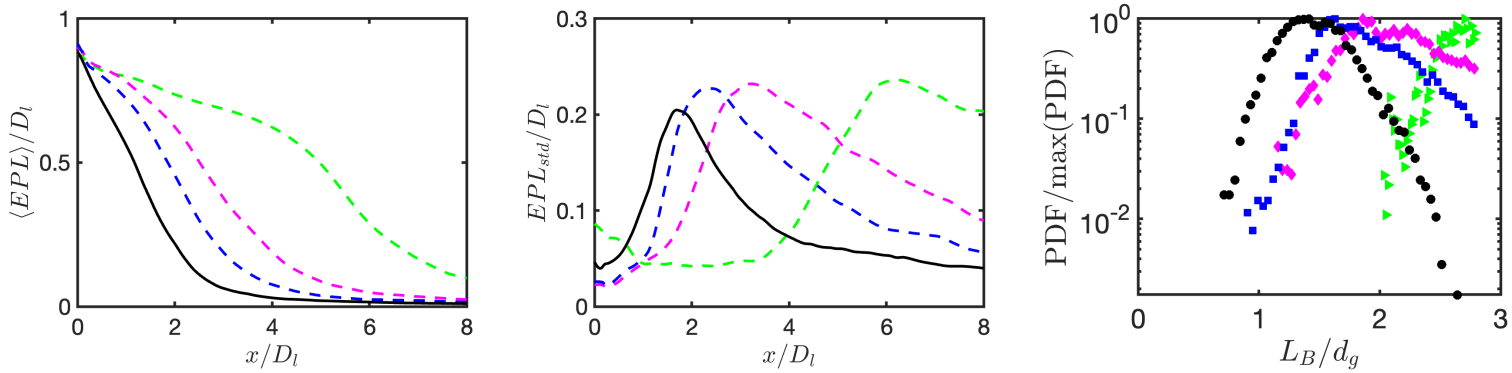

(a) $y/D_l = 0$ (b) $y/D_l = 0$ (c)

Figure 2.9: Influence of gas velocity model on a-b) EPL statistics and c) liquid core length PDFs using a vorticity thickness $2\delta_w$ (- -,▸), δ_w (- -,♦) and $\delta_w/2$ (- -,■) compared against the benchmark (—,●).

Table 2.3: Summary of metrics for gas velocity profiles using different vorticity thicknesses.

	$\langle L_B \rangle / d_g$	$L_{B,std}/d_g$	St
$2\delta_w$	2.57	0.161	7.38×10^{-3}
δ_w	2.07	0.354	7.38×10^{-3}
$\delta_w/2$	1.87	0.349	7.97×10^{-3}
Benchmark	1.46	0.284	1.13×10^{-2}

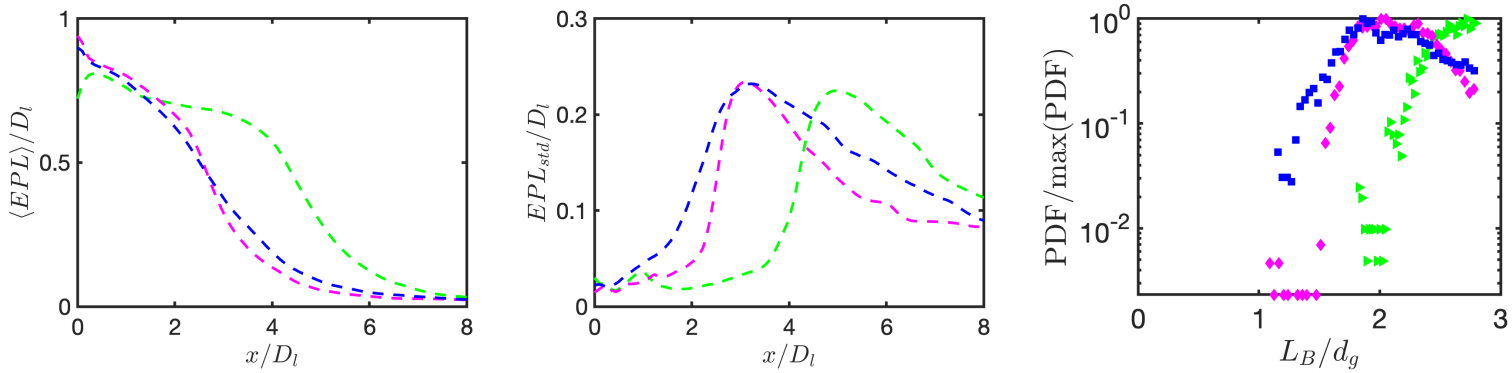

(a) $y/D_l = 0$ (b) $y/D_l = 0$ (c)

Figure 2.10: Influence of contact line model on a-b) EPL statistics and c) liquid core length PDFs for pinned to inner wall (--,▸), outer wall (--,♦) and a free contact line (--,■).

Table 2.4: Summary of metrics using different contact line models.

	$\langle L_B \rangle / d_g$	$L_{B,std}/d_g$	St
Pin to inner wall	2.55	0.175	4.92×10^{-3}
Pin to outer wall	2.14	0.284	5.06×10^{-3}
Free contact line	2.07	0.354	4.92×10^{-3}

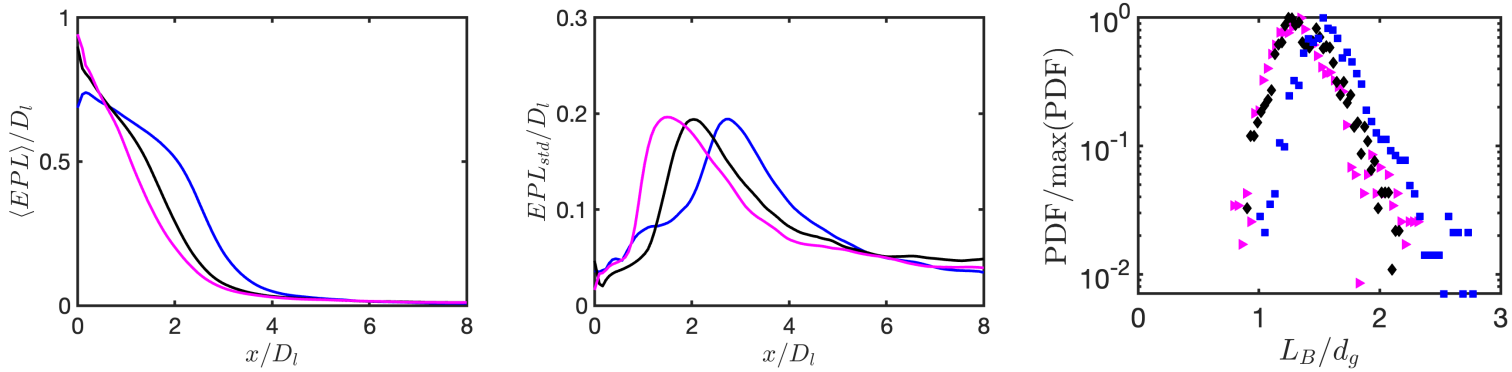

(a) $y/D_l = 0$ (b) $y/D_l = 0$ (c)

Figure 2.11: Influence of static contact angle on a-b) EPL statistics and c) liquid core length PDFs for 70° (—▸), 85° (—, ♦), and $\theta_s = 110°$ (—, ■).

Table 2.5: Summary of metrics using different static contact angles.

θ_s	$\langle L_B \rangle / d_g$	$L_{B,std}/d_g$	St
70°	1.35	0.242	1.05×10^{-2}
85°	1.46	0.284	1.13×10^{-2}
110°	1.61	0.259	1.28×10^{-2}

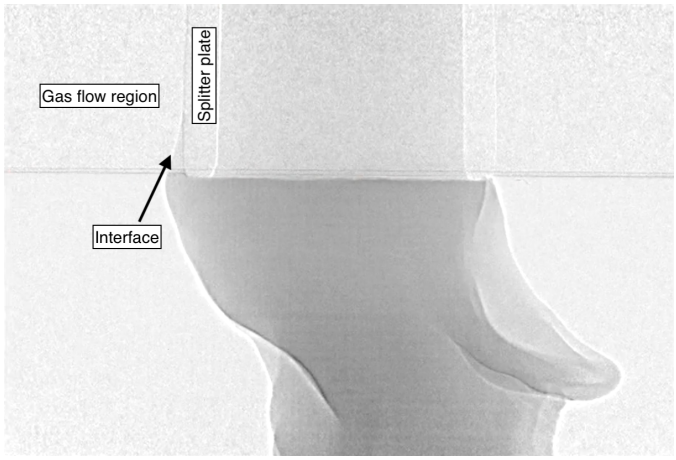

(a) Experimental Image

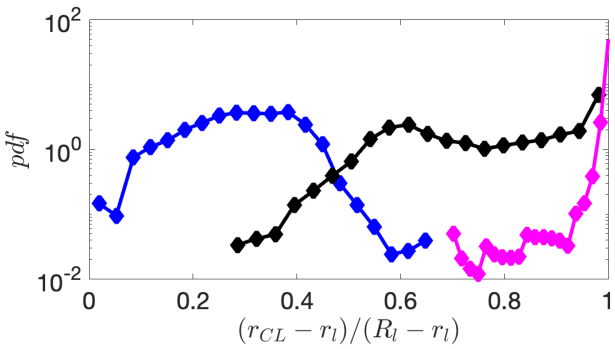

(b) PDF of contact line radius

Figure 2.12: a) Experimental image showing an instance where the contact line wicked up the outer wall into the gas flow region in the presence of gas swirl and b) the simulation's free contact line normalized radius PDF for $\theta_s = 70°$ (—), $\theta_s = 85°$ (—), $\theta_s = 110°$ (—). A normalized radius of 0 means that the contact line is at the inner wall of the splitter plate, while 1 indicates a location at the outer wall.

CHAPTER 3

HIGH-FIDELITY MULTI-SCALE MODELING OF ATOMIZATION WITH DROP SIZE COMPARISONS AGAINST EXPERIMENTS

3.1 Abstract

Coaxial atomizers create a spray by using a high-speed gas to shear and fragment a low-speed liquid. Computational predictions of drop sizes in coaxial atomizers present significant challenges, in part because of the wide range of length and time scales governing the processes involved. In this work, we employ a high-fidelity multi-scale atomization modeling strategy wherein multiple simulation domains are interfaced, with each domain tackling a different range of length scales of the problem. Upstream, we simulate the internal gas flow of the nozzle using a fairly inexpensive single-phase solver. This generates the gas inflow conditions for a Volume-of-Fluid (VOF) two-phase flow simulation of the spray formation region where sheets and ligaments are shed off the liquid core, generating a large number of drops. In stand-alone VOF simulations, droplet size distributions are based off broken liquid structures, limiting the smallest drop size to be on the order of the mesh size and making such measurements strongly mesh dependent. In contrast, we use a break up model that converts thin liquid structures into spherical, rigid Lagrangian particles which are transferred to an Euler-Lagrange simulation focused on the spray dispersion region. We compare droplet statistics generated with this multi-scale spray modeling strategy against experimental measurements.

3.2 Introduction

Sprays play an essential role in combustion systems and their effective modeling is crucial to improving surrounding technologies. Typically, computational spray modeling has been challenging, in part, because of its wide range of length scales. In a coaxial configuration, liquid and gas flow through a nozzle and the relevant scales can be as large as the flow-through areas and as small as the turbulence scales. Past the nozzle exit, a spray is formed when the gas breaks up the liquid into a collection of drops and ligaments. In this region, small length scales are involved due to interface deformation and topology change. The resultant liquid structures are dispersed over a large region roughly the size of the combustion chamber and eventually undergo evaporation and combustion. In the modeling of the spray dispersion region, drops are typically treated as rigid particles (the dispersed phase) whose sizes are determined by sampling a drop size distribution, and transported by the background fluid (the carrier phase). Methods for this modeling approach as well as evaporation and combustion modeling have been well-developed (e.g. [36, 58]). However, there exist limited models that produce drop size distributions starting from simulating spray formation from first principles. The focus of this paper is to present a simulation strategy to accomplish this at a relatively cheap cost. Furthermore, this strategy also simulates the spray dispersion region, giving it the potential to be scaled up to relevant industrial operating conditions.

Computational models that produce droplet distributions range in their complexity and physical accuracy. The simplest models forgo simulating the liquid injection and break up process and generate drops based on phenomenological processes of surface instabilities [89, 77, 9], liquid shedding [90], and turbulence [47]. More complex models (e.g. $\Sigma - Y$, ELSA) simulate the liquid injection process but

model the break up process [104, 59]. These models solve for a liquid-gas mixture, thereby bypassing the difficulty of interface tracking and related discontinuities, limiting their physicality. The highest fidelity models attempt to capture all scales of both the liquid injection and the break up process starting from the two-phase immiscible Navier-Stokes equations. However, these models come at a high cost because of the small scales associated with the break up process. To put in perspective, Ling et al. had mesh resolutions that ranged from $\Delta/h_l \approx 0.004 - 0.03$ where h_l is the height of the liquid flow passage, and used somewhere between 3 and 14 million core hours [60]. In the present model, we simulate all scales of the liquid injection process but model the break up process, reducing the computational cost by orders of magnitude. Our study is run at realistic air-war conditions and models many of these small scales using a mesh resolution an order of magnitude larger, $\Delta/d_l \approx 0.05 - 0.1$ where d_l is liquid jet diameter, and at a cost orders of magnitude lower, between 10 and 200 thousand core hours.

In this study, we present a multi-scale simulation strategy that produces drop size distributions that match experiments and tackles the multi-scale nature of atomization by using blocks, with each block tackling a range of scales of the problem using its own flow solver and domain. These blocks are coupled to each other using Dirichlet boundary conditions or volumetric forcing for the velocity field, and a thin structure break up model to convert liquid structures into drops. Three blocks are used to simulate the nozzle flow, spray formation, and spray dispersion processes. The velocity statistics at the nozzle exit are validated against experiments. Liquid distributions using a thin-film reconstruction method are validated against experiments and compared against a standard single plane reconstruction method (LVIRA) [85]. Drop size distributions using LVIRA and our model are compared against experiments. Results show that LVIRA exhibit heavily mesh dependent

results that do not match experiments while our model is weakly mesh dependent and agrees well with experiments. Finally, we show satisfactory agreement in radial statistics of mean drop size and velocity against experiments.

The Chapter is organized as follows, Section 3.3 describes the geometry used and the simulation conditions, Section 3.4 describes the governing equations and a brief description of the numerical methods used, Section 3.5 presents results from each block described above, and Section 3.6 summarizes results and proposes future directions.

3.3 Simulation Overview

A two-fluid coaxial atomizer [62], shown in fig. 3.1, is used in both simulations and experiments. The liquid flows through a straight circular pipe at a flow rate Q_l and separates the liquid from the coaxial gas stream that atomizes it. The gas enters the nozzle through four upstream ports perpendicular to the wall and flow through an annular passage at a total flow rate Q_g. U_l and U_g are the liquid and gas bulk velocities respectively, d_l is the liquid inner diameter, D_l, is the liquid outer diameter, and d_g is the gas inner diameter. The origin of our coordinate system is at the center of the nozzle exit. The non-dimensional parameters are summarized in table 3.1. A_g is the gas flow through area, ρ is the fluid density, μ is the dynamic viscosity, ν is the kinematic viscosity, σ is the surface tension coefficient, and subscripts l and g denote liquid and gas quantities, respectively.

Figure 3.2a illustrates the three aspects of the atomization process we model: the internal nozzle flow, the spray formation, and the spray dispersion region and fig. 3.2b shows a high-quality rendering of the spray. The gas nozzle flow is gener-

ated through a single phase simulation. The liquid is at a sufficiently low Re that it can be modeled as laminar pipe flow. The spray formation is simulated using a volume-of-fluid (VOF) method and a reconstruction method, R2P [20], capable of capturing liquid structures that fall below the mesh size. The spray dispersion is modeled using an Euler-Lagrange simulation where the carrier phase is solved on an Eulerian mesh and drops are tracked as Lagrangian rigid particles.

In the following section, we describe the governing equations used in each block and the coupling and time stepping to synchronize the blocks.

3.4 Governing Equations

3.4.1 Block 1: Nozzle Flow

Co-flowing liquid and gas streams at the nozzle exit mark the beginning of the spray formation region. The liquid injection is not simulated and the gas inflow conditions are generated by a concurrent running nozzle flow simulation. The gas flows through a non-trivial nozzle geometry at a high Re and we simulate it by solving the single phase incompressible Navier-Stokes equation,

$$\begin{aligned} \nabla \cdot \boldsymbol{u} &= 0, \\ \frac{\partial u}{\partial t} + \boldsymbol{u} \cdot \nabla \boldsymbol{u} &= -\frac{1}{\rho} \nabla p + \nu \nabla^2 \boldsymbol{u}. \end{aligned} \tag{3.1}$$

The nozzle is stair-stepped on a Cartesian mesh and consequently, convective and viscous operators are modified. Gas is injected through lateral ports upstream in the nozzle using Dirichlet boundary conditions and all other boundary conditions are treated as a Neumann outflow. A dynamic Smagorinsky turbulence model is employed to account for sub-grid scale turbulence scales [70]. The domain size is

$10d_g \times 10d_g \times 10d_g$ and the mesh spacing $\Delta_1/d_g = 0.05$ is uniform in all directions. The nozzle plenum is the furthest point upstream in the domain and the furthest point downstream is d_g past the nozzle exit.

3.4.2 Block 2: Spray Formation

The spray formation is simulated by solving the liquid-gas flow equations for incompressible, immiscible fluids. The governing equations are

$$\begin{aligned} \nabla \cdot \boldsymbol{u} &= 0, \\ \rho \frac{\partial u}{\partial t} + \rho \boldsymbol{u} \cdot \nabla \boldsymbol{u} &= -\nabla p + \nabla \cdot (\mu [\nabla \boldsymbol{u} + \nabla \boldsymbol{u}^{\mathsf{T}}]), \\ \frac{\partial \alpha}{\partial t} + \boldsymbol{u} \cdot \nabla \alpha &= 0, \end{aligned} \tag{3.2}$$

with the jump conditions

$$\begin{aligned} [\![\boldsymbol{u}]\!] &= 0, \\ [\![p]\!] &= \sigma\kappa + 2\big[\mu\big]_{\Gamma} \boldsymbol{n}^{\mathsf{T}} \cdot \nabla \boldsymbol{u} \cdot \boldsymbol{n}, \end{aligned} \tag{3.3}$$

where α is the liquid volume fraction in a cell, $[\![\cdot]\!]$ denotes the difference of a liquid and gas quantity across the interface and $\boldsymbol{n}$ is the interface normal. Equations (3.2) and (3.3) are solved using a geometric volume-of-fluid method [80]. Density and viscosity are approximated in a cell by

$$\begin{aligned} \rho &= \alpha\rho_l + (1-\alpha)\rho_g \\ \mu^{-1} &= \alpha\mu_l^{-1} + (1-\alpha)\mu_g^{-1}. \end{aligned} \tag{3.4}$$

In standard VOF schemes, the interface is represented in a computational cell using a single piece-wise linear interface (PLIC), whose interface can be calculated using LVIRA [85]. In our simulation, we use R2P as a reconstruction method which enables thin structures to be tracked below the mesh resolution by allowing two PLICs to co-exist in a computational cell [20]. The interface curvature is calculated using paraboloid surface fits and the pressure jump is incorporated into the pressure solver using a continuum surface force approach [87]. To capture sub-grid scale (SGS) effects, a dynamic Smagorinsky turbulence model [70] and sub-grid scale contact line model are employed [107]. The SGS contact line model assumes as static contact angle of 85°. The domain size is $11.16D_l \times 10D_l \times 10D_l$ and begins at $1.16D_l$ upstream of the nozzle, simulating a portion of the nozzle tip. The mesh size is uniform in all directions with a size $\Delta_2/d_l = 0.05$. All boundary conditions are Neumann outflows except the inflow boundary where the liquid is given a parabolic velocity profile and the gas velocity is interpolated from block 1 in a time-accurate fashion.

3.4.3 Coupling from Block 1 to 2

Block 1 and block 2 overlap for $x \in [-1.16D_l, d_g]$. Block 1 is one-way coupled with block 2 through a velocity interpolation plane at $x = -1.16D_l$. Block 1 simulates the flow a distance d_g downstream to allow the gas to expand but in the absence of liquid. Block 2 includes a portion of the nozzle tip to allow for flow development while simultaneously accounting for the out-flowing liquid.

3.4.4 Block 3: Spray Dispersion

The spray dispersion region is modeled using an Euler-Lagrange type strategy where velocity is solved on an Eulerian mesh and drops are tracked as Lagrangian rigid particles with one-way coupling. The governing equations are

$$\begin{aligned} \nabla \cdot \boldsymbol{u} &= 0, \\ \frac{\partial u}{\partial t} + \boldsymbol{u} \cdot \nabla \boldsymbol{u} &= -\frac{1}{\rho}\nabla p + \nu \nabla^2 \boldsymbol{u}. \end{aligned} \tag{3.5}$$

for the carrier phase and

$$\begin{aligned} \frac{\mathrm{d}\boldsymbol{x_p}}{\mathrm{d}t} &= \boldsymbol{u_p}, \\ \frac{\mathrm{d}\boldsymbol{u_p}}{\mathrm{d}t} &= -f_s \frac{\boldsymbol{u_{p,r}}}{\tau_p}. \end{aligned} \tag{3.6}$$

for the dispersed phase where $\boldsymbol{x_p}$ is the particle position, $\boldsymbol{u_p}$ is the particle velocity, $\boldsymbol{u_{p,r}} = \boldsymbol{u_p} - \boldsymbol{u}$ is the relative particle velocity. $f_s = 1 + 0.15 Re_p^{0.687}$ is the Schiller-Naumann drag coefficient on the particle where $Re_p = d_p u_{p,r}/\nu_g$, $\tau_p = \rho_l d_p^2/18\mu_g$ is the particle Stokes response time, d_p is the particle diameter and ν_g is the gas kinematic viscosity. The domain size is $10d_g \times 10d_g \times 10d_g$ with a uniform mesh size $\Delta_3/d_g = 0.1$. The domain includes a portion of the nozzle and begins at $x = -d_g$ as is the case for block 2 but mask out the liquid flow region. A Lagrangian dynamic SGS turbulence model is applied [70]. Boundary conditions are Neumann outflows in all directions.

3.4.5 Coupling from Block 2 to 3

Velocity Coupling

Block 3 domain encompasses the entirety of block 2. Block 2 is one-way coupled with block 3 through volumetric forcing. The source term

$$\boldsymbol{S} = \frac{\boldsymbol{u_2} - \boldsymbol{u_3}}{dt_3}(w_x w_y w_z)^2 \tag{3.7}$$

where

$$\begin{aligned} w_x(x) &= \max[(L_x - x)/L_x, 0] \\ w_y(y) &= \max[2(L_y/2 - |y|)/L_y, 0] \\ w_z(z) &= \max[2(L_z/2 - |z|)/L_z, 0], \end{aligned} \tag{3.8}$$

is added to the gas momentum equation which puts weights near the nozzle exit. $\boldsymbol{u_2}$ is the velocity in block 2 interpolated in time and space to block 3, $\boldsymbol{u_3}$ is the velocity in block 3 and $\mathrm{d}t_3$ is the time step of the third block.

Mesh Resolution Requirements: Hinze Scale

As R2P allows the mesh to capture thin liquid structures far smaller than the mesh (close to machine precision), a question arises – how coarse can we allow the mesh be? The answer is related to the Hinze Scale (also referred to as the Kolmogorov Critical Radius), which is related to the balance between the inertia from turbulent eddies to surface tension. Figure 3.3 illustrates a turbulent eddy of size l with a characteristic velocity u' impacting a liquid-gas interface with a surface tension σ. A turbulent Weber number can be formed $We_{turb} = \rho u'^2 l/\sigma$ where ρ is the gas density. When $We_{turb} \sim 1$, inertia balances surface tension and the length scale at which this happens is the Hinze Scale $l_\sigma = \sigma/(\rho u'^2)$. It can be shown in different

turbulence ranges (i.e. different estimates of u'),

$$l_\sigma \sim \begin{cases} (\frac{\sigma\nu}{\rho\epsilon})^{1/3} & l_\sigma \ll \eta \\ (\frac{\sigma^3}{\rho^3\epsilon^3})^{1/5} & l_\sigma \gg \eta \end{cases} \tag{3.9}$$

where η is the Kolmogorov Scale, ν is the gas kinematic viscosity, and ϵ is the turbulent dissipation (see [54, 45, 99] for full derivation).

We will now look at the effect of eddies on the interface topology at length scales both smaller and larger than the Hinze Scale. We consider a homogeneous isotropic turbulence case, in a triple periodic box, with a density and viscosity ratio of 1 and a surface tension coefficient σ. Figure 3.4 shows results from a study conducted by [69]. The traditional energy spectrum as a function of wave number is plotted along with a probability density function (PDF) of curvedness, $c = \sqrt{\gamma_1^2 + \gamma_2^2}$, which represent a geometric average of the two principal curvatures γ_1 and γ_2. The x axis is a length scale l normalized by the Hinze Scale, the energy spectrum determines the amount of energy (or inertia) an eddy contains at a length scale l ($\kappa = 2\pi/l$), and the PDF of curvedness ($c = 1/l$) is related to the likelihood that an eddy at that scale, would imprint onto the interface. When $l_\sigma/l \ll 1$, the eddies have enough energy to overcome the effects of surface tension, as observed in the high probability of curvedness. However, if $l_\sigma/l \gg 1$, the eddies do not have enough energy to overcome surface tension and a low probability of curvedness is observed. Thus, when $l_\sigma/l \gg 1$, turbulent eddies have almost no effect on the interface topology. Therefore, the mesh size should be smaller than the Hinze scale to capture all of the turbulent effects on the interface topology. Any scales of liquid structures below the Hinze scale, are likely to exist in the form of sheets, ligaments, and drops, termed here as meta-stable structures. Their modeling can all be encapsulated in the break up model discussed in the following section.

Thin Structure Break Up Model

A thin structure break up model is used in block 2 to break thin liquid structures into drops and transfer their volume to block 3 to be tracked as Lagrangian particles. We will discuss the model in the context of films but the model works equivalently for any thin liquid structure. This model begins by tagging and tracking coherent liquid films using a connected-component labeling (CCL) algorithm [40]. In this algorithm, thin liquid films are given a global identification number and the corresponding lists of cells that intersect them. The film thickness is approximated to be the ratio of liquid volume to cross sectional area in a 27 cell stencil and is calculated through

$$h = 2\frac{\sum_{i}^{27} \alpha_i V_i}{\sum_{i}^{27} A_{PLIC,i}} \tag{3.10}$$

where i is the stencil index and A_{PLIC} is the surface area of the PLIC polygons. The smallest thickness h_{min} is monitored over time and when this thickness falls below a specified threshold value $h_{threshold}$, the break up model is executed. Starting from the smallest thickness, a running sum is kept of the liquid volume as the cells are traversed in order of increasing thickness. This continues until the running sum volume exceeds the volume of a particle that has a diameter that is a specified ratio, β, larger than the local film thickness. At this point, the particle is created and the remaining volume from that running sum is carried forward and the process repeats until the entire film volume has been depleted. When no more particles can be created, the remainder of the running sum volume is evenly distributed to all particles by scaling their diameter, making this model exactly volume conserving. The particles are placed at the centroid of their respective

converted film, and given the velocity at the particle location. For this study, $h_{threshold} = 0.1\ \mu$m which is an estimate based on experimental studies [105, 76]. Studies [2] have also suggested a power law dependence of β on h but for simplicity in this study, we assume $\beta = 10$. Algorithm 1 details this break up model. Figure 3.5 shows the liquid gas interface and particles at an instance before and after the break up model is executed.

3.4.6 Time Step Synchronization

Block 2 simulates the spray formation region which poses the most difficult modeling challenge and plays the most influential role on droplet distributions. Block 1 supplies block 2 with inflow conditions while block 3 cheaply enables the dispersion region to be captured. Therefore, block 2 acts as the main time driver and blocks 1 and 3 synchronize around it. Algorithm 2 provides a complete description of the synchronization of the blocks.

3.5 Results

3.5.1 Block 1: Velocity Statistics

Block 1's role is to yield realistic inflow conditions for block 2. As the gas velocity at the nozzle exit in block 2 directly affects the liquid jet, velocity statistics are sampled on block 2. Figure 3.6a show that the mean stream-wise velocity matches well against experimentally acquired hot wire data. Moreover, fig. 3.6b shows fluctuations at the inner wall that directly impact the liquid instabilities are well

predicted. However, they are over predicted at the outer wall where they play a secondary role.

3.5.2 Block 2: Liquid Distributions

The liquid is spatially distributed as the spray forms. Equivalent path length (EPL), the integrated liquid depth along a line of sight, is a measurement of liquid distribution. Experimentally, it can be accurately extracted through focused beam X-ray measurements [15]. In the simulations, EPL is calculated by integrating the volume fraction over the z direction, i.e,

$$EPL = \int \alpha \, \mathrm{d}z. \tag{3.11}$$

Figure 3.7 shows the centerline and transverse EPL profiles using R2P validated against experiments and compared against LVIRA. Figures 3.7b and 3.7c shows excellent agreement in R2P against experiments and shows minor differences against LVIRA. In particular, R2P exhibits slightly lower values in $\langle EPL \rangle$ for $x/D_l > 1.5$ and EPL_{std} peaks at $x/D_l = 1.5$. $x/D_l \approx 1.5$ is visually confirmed to be the downstream location in which inflating large scale bags tend to pivot around the main body of the liquid. By virtue of this, much of the thin film model conversion occurs just downstream this point. By converting the liquid structures, it is likely that the liquid volume is under-predicted in this region, explaining the lower mean EPL values.

Figures 3.7d to 3.7k show the transverse EPL profiles. Figures 3.7d to 3.7g show that for $\langle EPL \rangle$, R2P matches the experimental data well and closely follows

LVIRA. Figures 3.7h and 3.7i show the same behavior for the EPL_{std} profiles. However, figs. 3.7j and 3.7k show that R2P begins to deviate from LVIRA and the experiments as the downstream distance is increased.

3.5.3 Block 3: Velocity Nudging and Drop Statistics

Figures 3.8a and 3.8b show the the velocity statistics averaged in time and on the mid plane ($z = 0$) with block 2 superimposed on top of block 3. The figures suggest the nudging strategy is effective as it does a great job in enforcing the continuity of velocity statistics between the two blocks. Figure 3.8a shows the expansion of a high-speed annular gas jet whose momentum diffuses radially outward as it moves downstream. Furthermore, upstream close to the nozzle exit, an imprint of the low-speed liquid is seen. Figure 3.8b shows that the velocity standard deviation locally peaks near the outer gas-gas shear layer and the liquid-gas shear layer.

Figure 3.9 shows drop size distributions using LVIRA and R2P using two different mesh sizes and comparisons against experiments. In standard LVIRA, numerical error is the predominant cause of break up and results in two-types of liquid structures than can be extracted as drops: 1) isolated flotsams below the mesh size and 2) resolved drops above the mesh size. The former is produced solely due to numerical error and the latter is produced when larger liquid structures detach through more physical mechanisms such as when the neck of a ligament undergoing a Rayleigh-Plateau instability falls below the mesh size. Therefore, we only consider drops above the mesh size and may expect heavily mesh dependent drop size distributions. In contrast, since R2P is able to maintain films below the mesh size and the break up process is modeled, we may expect a limited mesh dependency on the drop size distributions. Results confirm this, showing that drop size distri-

butions using LVIRA are heavily mesh dependent with peaks around two or three times the mesh size and are in poor agreement with experiments. In contrast, R2P with our thin structure break up model show excellent agreement with experiments and exhibit a weak mesh dependence. The Sauter mean diameter calculated in the simulation is 102.4 μm which is in good agreement with the experimental value 106.2 μm.

Figures 3.10a to 3.10c show the radial drop statistics using the simulation with mesh size Δ_2. Figure 3.10a show the mean drop size from the simulation is in satisfactory agreement with the experiment. Figures 3.10b and 3.10c show the stream-wise and radial velocity statistics are in moderate agreement with experimental measurements. The simulations predict roughly the correct scaling, but over predict both the mean and standard deviation. One possible reason for this is that particles are initialized with the gas velocity interpolated to the particle location. However, other physics such as film retraction, which are not modeled here, influence the drop's velocity. The carrier phase imposes a drag on the particles and due to Newton's third law, the particles impose an equal and opposite drag on the carrier phase, which was not modeled. Therefore, the carrier phase has a higher velocity, which in turn, transports the particles with a higher velocity.

3.6 Conclusion

In this study, we presented a high fidelity multi-scale simulation strategy to produce drop size distributions capable of matching experiments. This multi-scale simulation strategy relies on coupled blocks, with each block tackling a different length scale of the problem. We used three blocks to model the nozzle flow, spray

formation, and spray dispersion. The nozzle flow was validated by showing good experimental agreement of velocity statistics. The spray formation was validated by showing good agreement of liquid distribution statistics against experiments. We validated our break up model by showing that our method exhibited excellent agreement of droplet size distribution against experimental measurements. Finally, we showed good agreement in drop velocity statistics as a function of radial distance.

This break up model requires tunable parameters such as the termination length scale to activate the model, $h_{threshold}$ and the film thickness to drop diameter conversion factor, β. Future studies can be taken to access the dependence of these parameters on resultant drop size distributions. Moreover, better physical modeling of the thin sheets would prove useful as their development and local film size distribution at the time of break up would be more accurate, directly impacting drop size distributions.

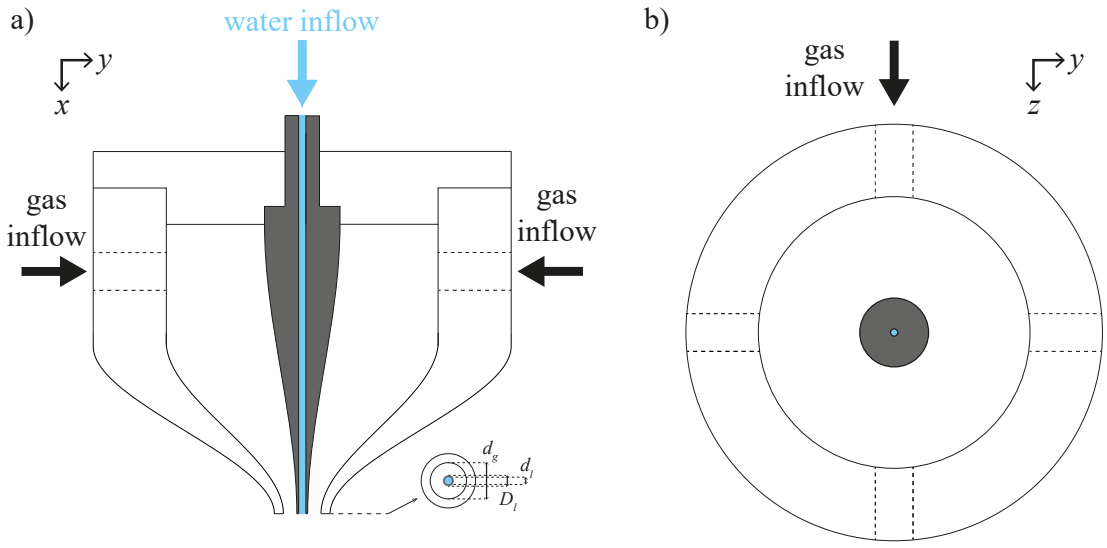

Figure 3.1: Nozzle schematic cut longitudinally (left) and transversely (right). Water is injected through a circular needle while gas is injected through four gas ports.

Table 3.1: Simulation's non-dimensional parameters: gas Reynolds number (Re_g), liquid Reynolds number (Re_l), momentum flux ratio (M), Weber number (We), density ratio (ρ^*) and viscosity ratio (μ^*).

$Re_g \equiv \frac{4Q_g}{\sqrt{4\pi A_g}\nu_g}$	$Re_l \equiv \frac{\rho_l U_l d_l}{\mu_l}$	$M \equiv \frac{\rho_g U_g^2}{\rho_l U_l^2}$	$We \equiv \frac{\rho_g (U_g - U_l)^2 d_l}{\sigma}$	$\rho^* \equiv \frac{\rho_l}{\rho_g}$	$\mu^* \equiv \frac{\mu_l}{\mu_g}$
21400	1200	6.4	39.1	815	65

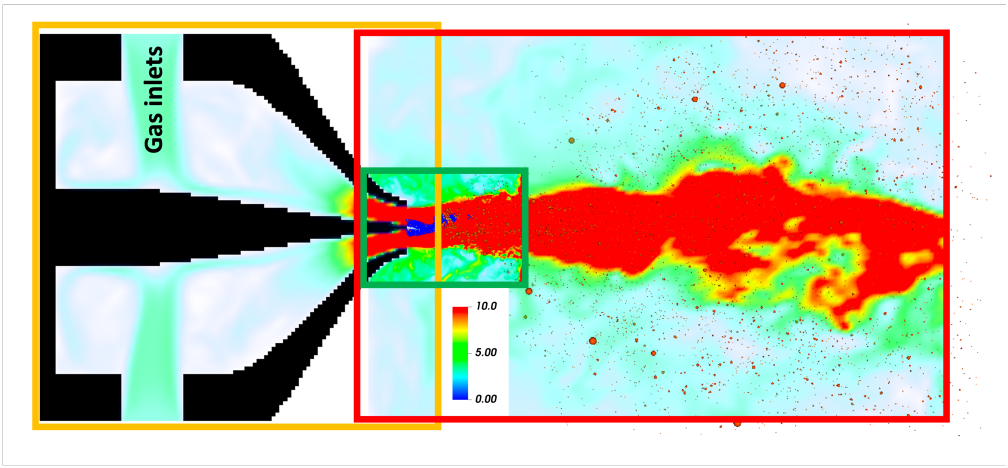

(a)

(b)

Figure 3.2: a) Illustration of 3 blocks boxed for the nozzle simulation (orange), spray formation (green), and spray dispersion (red) regions. Plot of pseudocolor of velocity, interface (blue) and particles (orange). b) Ray-traced image of the simulation

Algorithm 1 Thin liquid structure transfer algorithm

Transfer algorithm
Input: β, $h_{threshold}$
for each tagged film **do**
    # *Enable transfer only if film meets criteria*
    if $h_{min} \leq h_{threshold}$ **then**
        # *Initialize running sum and sort film*
        $V_{transfer}, V_{transferred} \leftarrow 0$
        Sort list of cells L in current film in order of increasing h
        for i in L **do**
            # *Update running sum of volume counter*
            $V_{transfer} \leftarrow V_{transfer} + \alpha_i V_i$
            $V_{droplet} \leftarrow \pi(\beta h_i)^3/6$
            # *Create Lagrangian drop*
            while $V_{transfer} \geq V_{droplet}$ **do**
                Create Lagangian drops, $d_p \leftarrow \beta h_i$, $\boldsymbol{x_p} \leftarrow$ centroid of film in current cell i, $\boldsymbol{u_p} \leftarrow \boldsymbol{u}(\boldsymbol{x_p})$
                # *Carry forward leftover volume and track liquid volume transferred thus far*
                $V_{transfer} \leftarrow V_{transfer} - V_{droplet}$
                $V_{transferred} \leftarrow V_{transferred} + V_{droplet}$
            end while
            # *Remove liquid in current cell from block 2*
            $\alpha_i \leftarrow 0$
        end for
        # *Re-scale drop diameters with left over volume*
        for each created Lagrangian droplet **do**
            $d_p = d_p(\frac{V_{transferred}+V_{transfer}}{V_{transferred}})^{\frac{1}{3}}$
        end for
    end if
end for
Output: A list of drops with attributes d_p, $\boldsymbol{x_p}$, $\boldsymbol{u_p}$

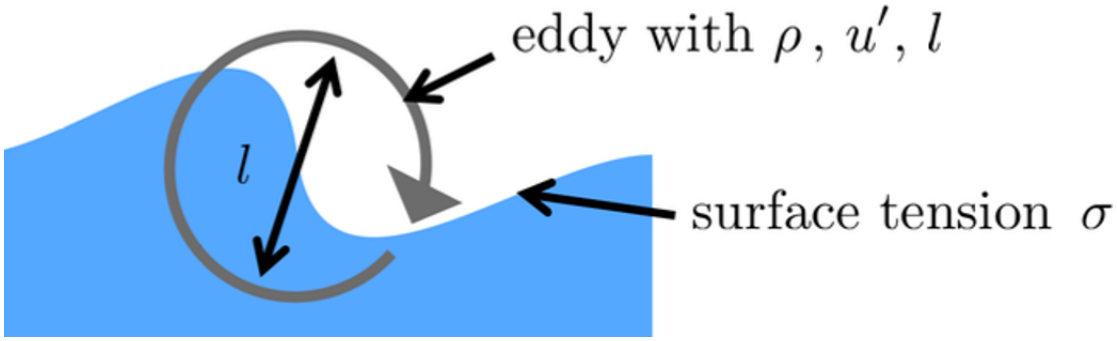

Figure 3.3: Schematic an eddy impacting a liquid-gas interface, representing the balance between inertia and surface tension.

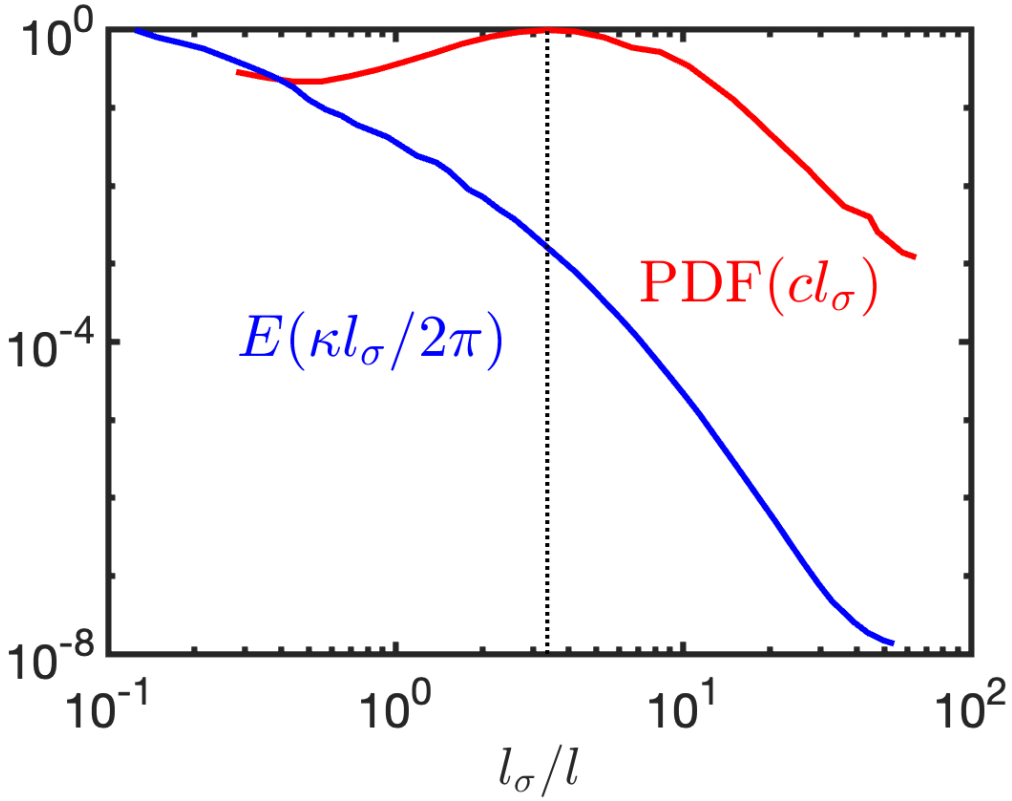

Figure 3.4: Normalized energy spectrum (—) of turbulent eddies and probability density function of interface curvedness (—). The x axis is the respective length scale l normalized by the Hinze Scale where the wavenumber is $\kappa = 2\pi/l$ and the curvedness $c = 1/l$. $l_\sigma/l \sim 1$ is shown in (····).

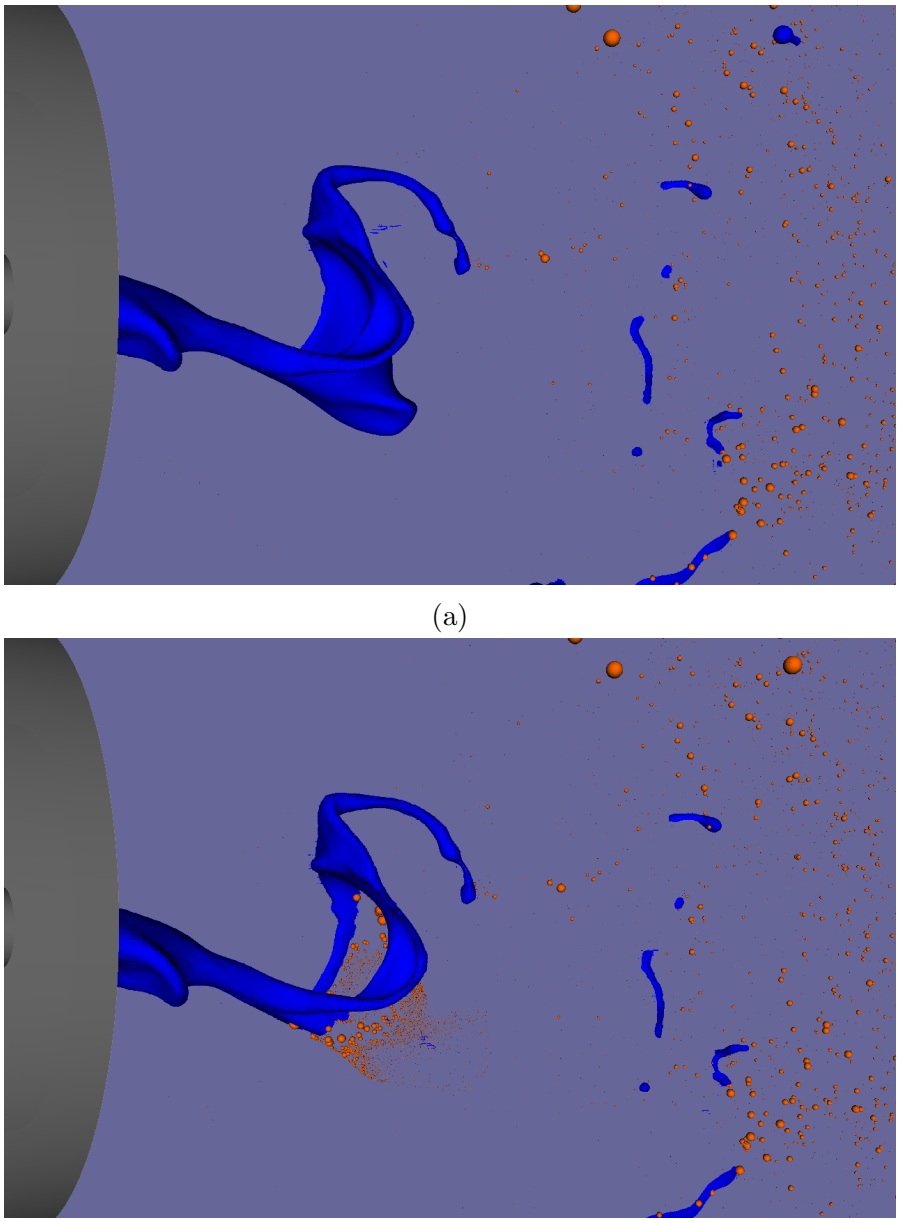

(a)

(b)

Figure 3.5: Illustration of break up model in a) frame before and b) after breakup model is activated.

Algorithm 2 General solution algorithm

```
# Solve until block 2 reaches final time
while t_2 < T_f do
    # Update block 1's flow solver
    while t_1 < t_2 do
        Update block 1 by solving eq. (3.1)
        t_1 ← t_1 + dt_1
    end while
    # Update block 2's flow solver
    Interpolate velocity in space and time from block 1 to block 2
    Update block 2 by solving eqs. (3.2) and (3.3)
    Track liquid structures through CCL algorithm and monitor film thickness
    Transfer liquid structures to Lagrangian particles using algorithm 1
    t_2 ← t_2 + dt_2
    # Update block 3's flow solver
    while t_3 < t_2 do
        Nudge velocity from block 2 to block 3 through eq. (3.7)
        Update block 3 by solving eqs. (3.5) and (3.6)
        t_3 ← t_3 + dt_3
    end while
end while
```

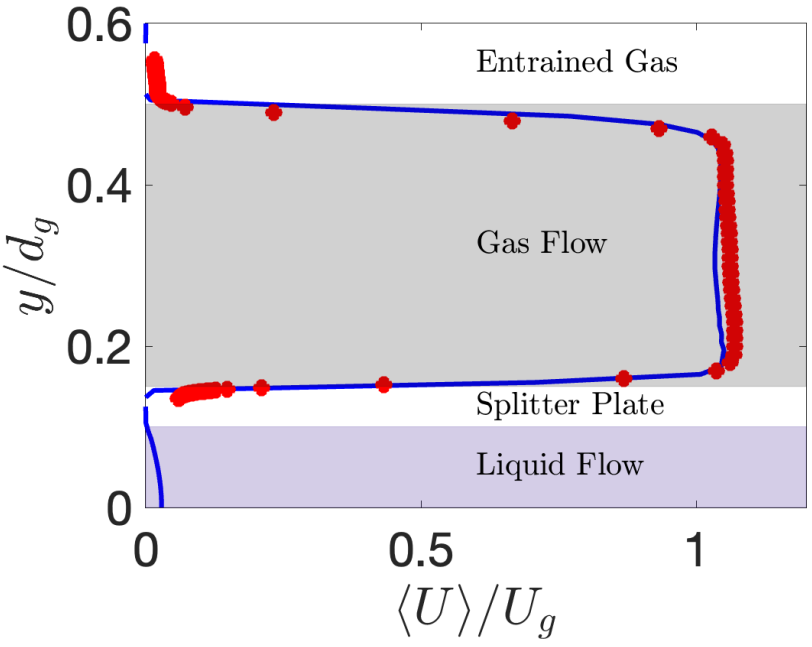

(a)

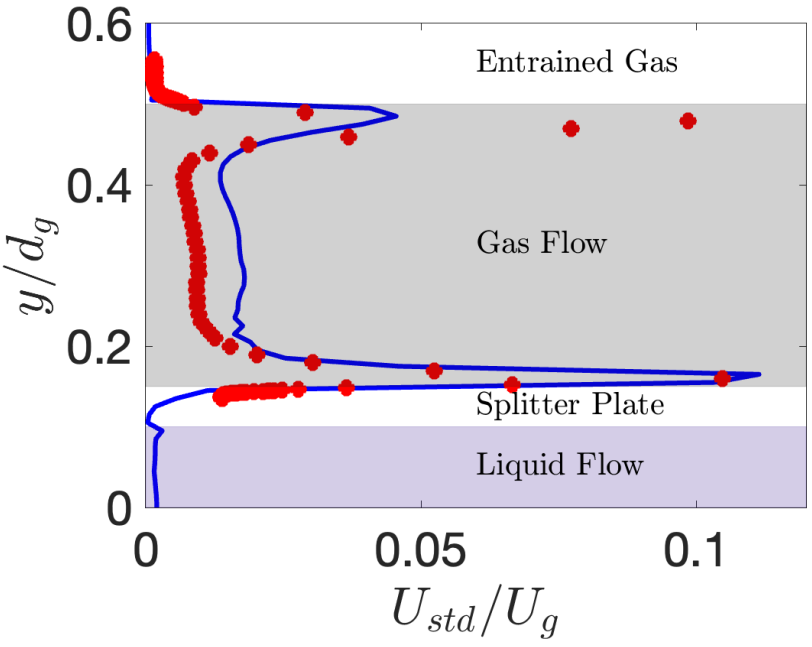

(b)

Figure 3.6: Comparisons of velocity statistics between the simulation (—) and experiment (●).

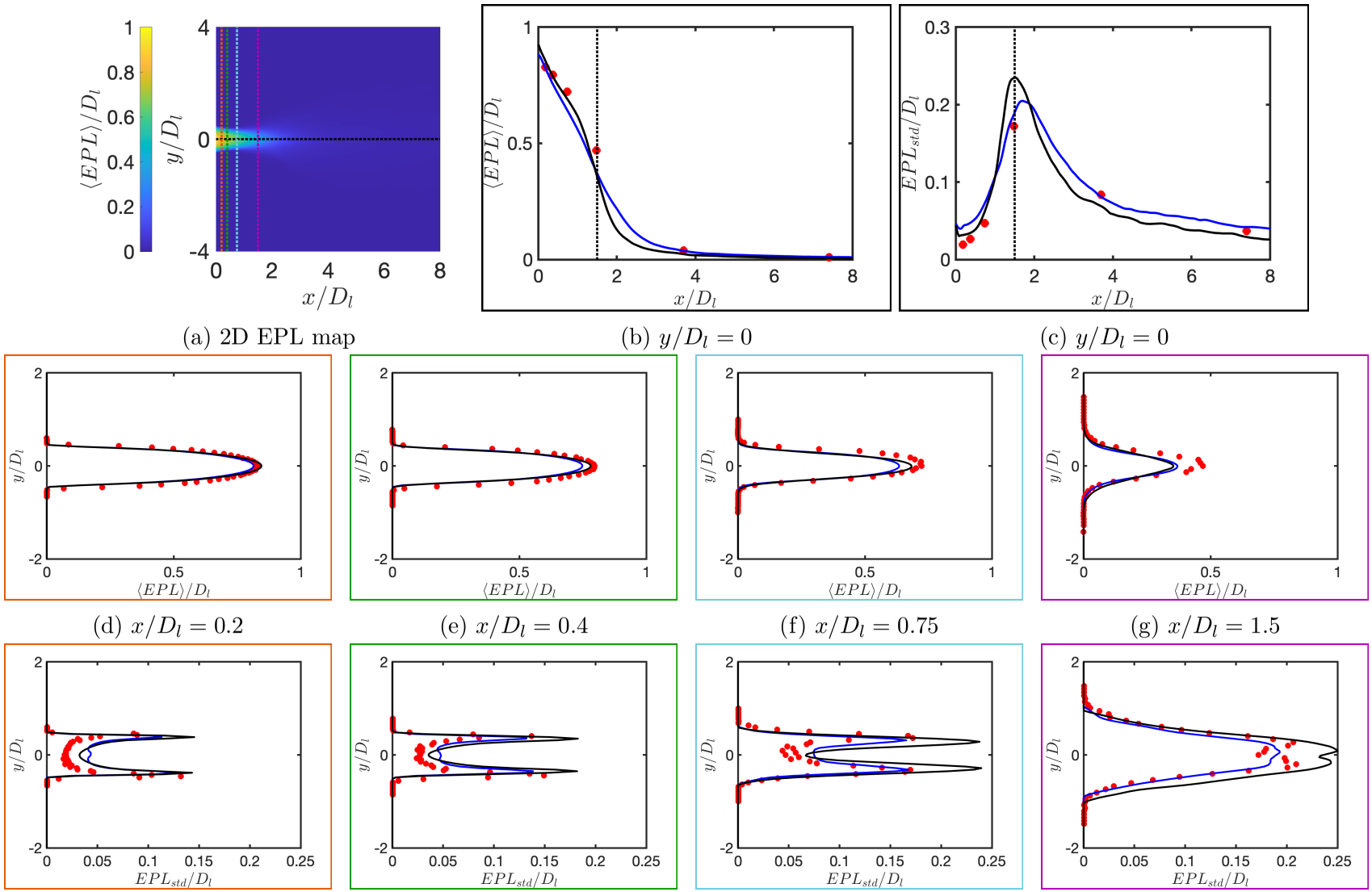

(a) 2D EPL map (b) $y/D_l = 0$ (c) $y/D_l = 0$

(d) $x/D_l = 0.2$ (e) $x/D_l = 0.4$ (f) $x/D_l = 0.75$ (g) $x/D_l = 1.5$

(h) $x/D_l = 0.2$ (i) $x/D_l = 0.4$ (j) $x/D_l = 0.75$ (k) $x/D_l = 1.5$

Figure 3.7: Simulation compared against experiments. a) 2D EPL map with sampling locations marked, b-k) EPL comparisons between simulations using ELVIRA (—),R2P (—) and experiments (●). $x/D_l = 1.5$ (····) is plotted for reference.

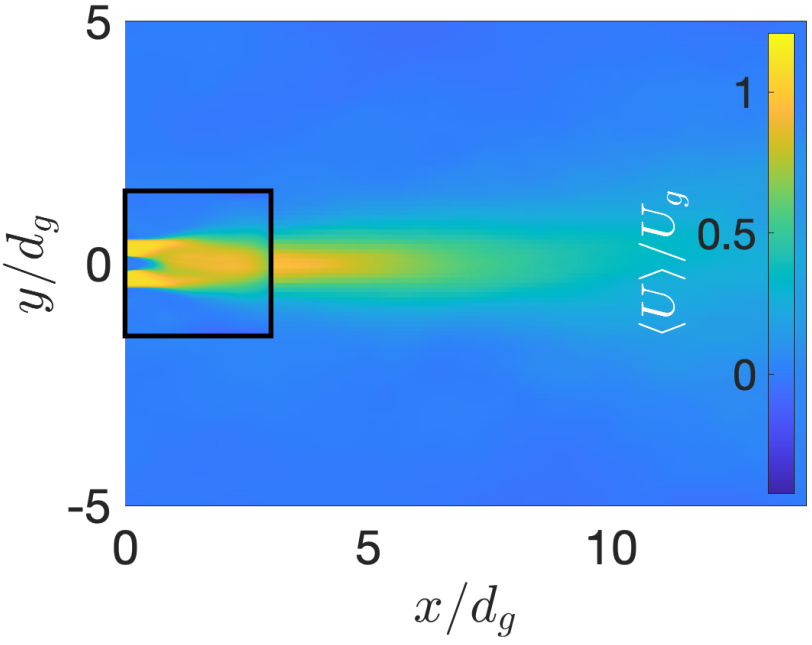

(a)

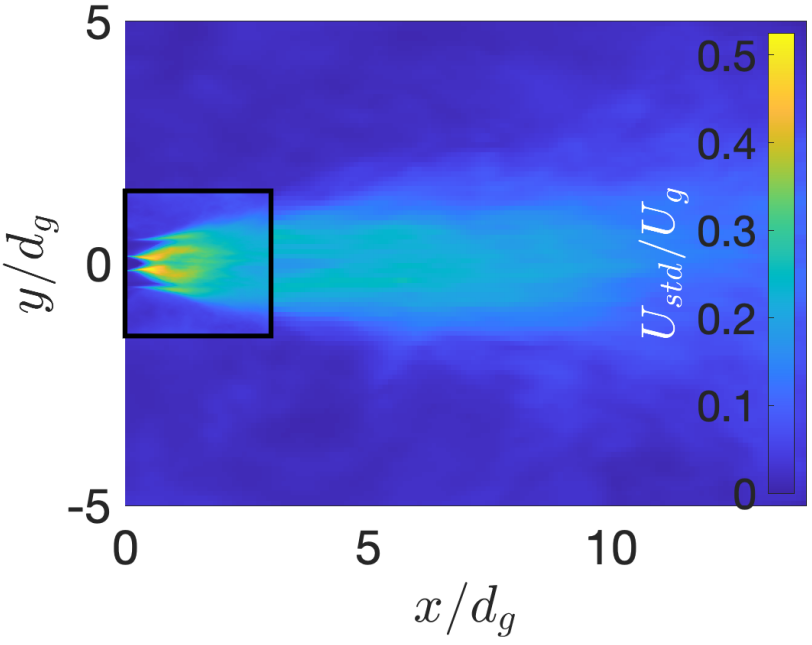

(b)

Figure 3.8: Illustration of nudging to couple block 2 and 3. Velocity are shown for a) mean and b) velocity stats showing the expansion of the gas jet.

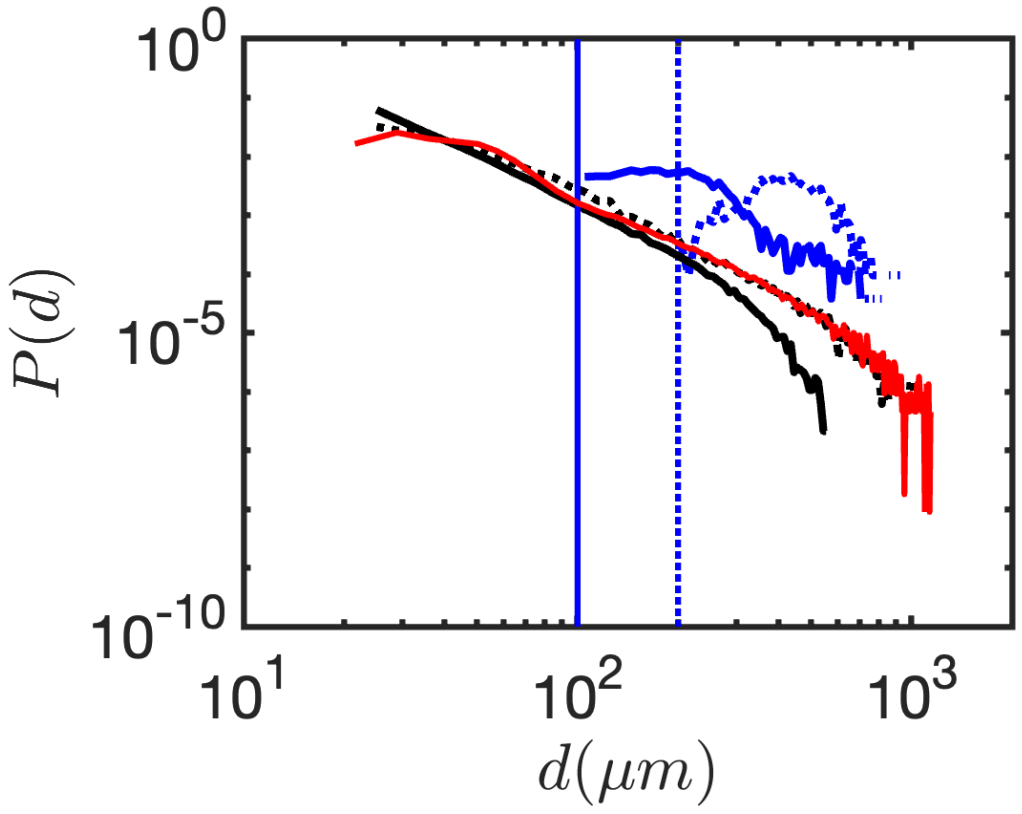

Figure 3.9: Comparisons of drop size distributions between LVIRA with mesh spacing $2\Delta_2$ (- -) and Δ_2 (—), R2P with mesh spacing $2\Delta_2$ (- -) and Δ_2 (—) and experiment (—). Vertical dashed and solid lines denote $2\Delta_2$ and Δ_2 respectively.

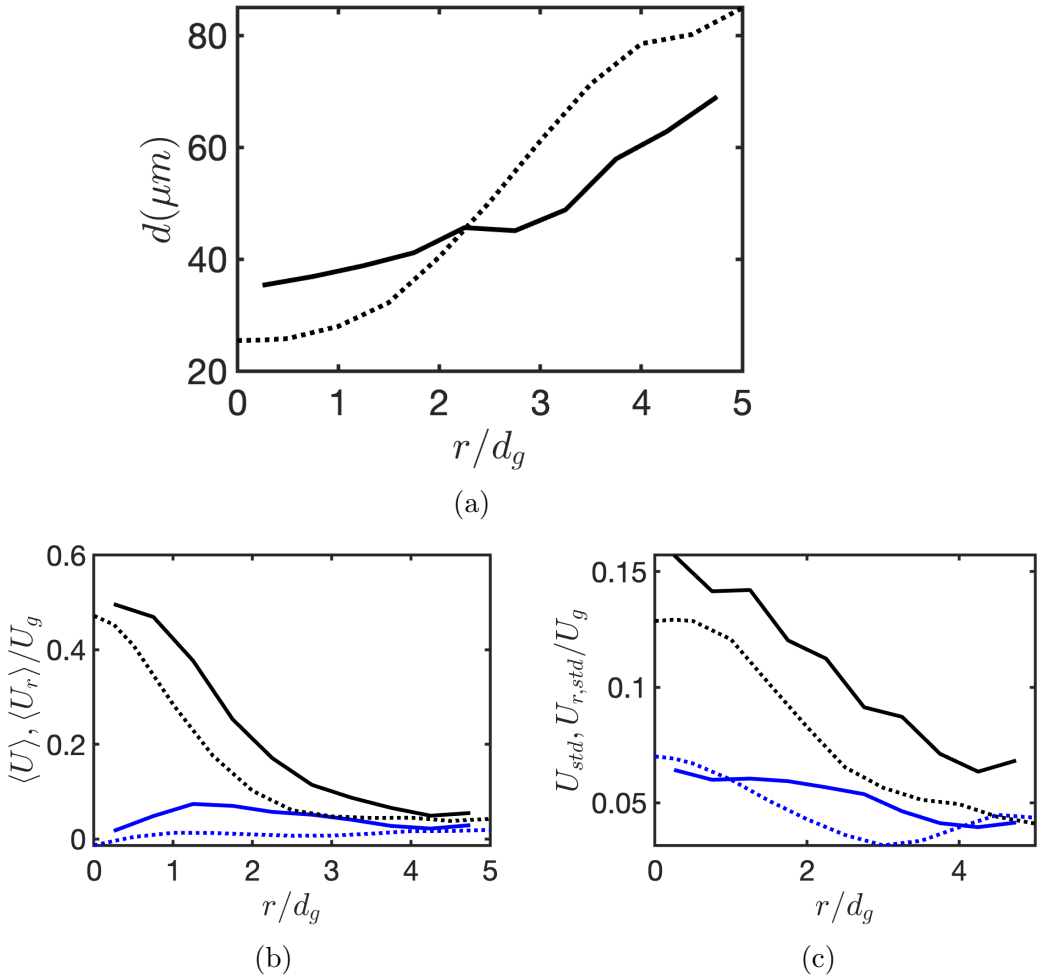

Figure 3.10: Radial drop statistics a) mean drop size measured from experimental PDPA (- -) and simulations (—). b) Mean and c) standard deviation of drop velocity statistics for the stream-wise velocity U (black) and radial velocity U_r (blue) comparing simulations (solid lines) and experiments (dotted lines).

CHAPTER 4

AN ADJOINT METHOD FOR CONTROL OF LIQUID-GAS FLOWS USING A SHARP INTERFACE MODEL

4.1 Abstract

We present a computational adjoint framework for the optimization of liquid-gas flows using a sharp interface model. The two-phase Navier–Stokes equations are solved using a mass-conserving geometric Volume-of-Fluid method while the adjoint equations consider a level set based representation of the interface and its sensitivity. To facilitate the accurate transport of surface sensitivity, a geometric surface transport method is formulated and applied. We validate our method by comparing adjoint calculated gradients against analytical gradients or finite difference approximations. Finally, optimization is performed on a variety of benchmark two-phase flow problems. Cases include highly multi-dimensional inflow control of droplet position and optimal control of the initial velocity profile in a temporally evolving liquid-gas mixing layer.

4.2 Introduction

Liquid-gas flows appear in a variety of engineering applications, such as wave-energy conversion systems [42, 82], fuel sprays for combustion engines [71], and injection molding in the manufacturing industry [22], among others. Effective modeling of liquid-gas flows is a first step to better design and improve performance of such systems. In recent decades, significant progress has been made on numerical methods for liquid-gas flows (e.g. [6, 79, 43, 103, 94, 98]), enabling high-fidelity

simulations. These simulations have been capable of generating unprecedented amounts of data, while simultaneously incorporating physical processes such as turbulence [50] and evaporation [83]. Because of these advancements on the modeling side, a new area of research is emerging focused on the computational control of liquid-gas flows.

The optimization of dynamical systems can be conducted using several common methods such as derivative-free methods or standard gradient descent-type methods. Some derivative-free methods include pattern search methods [46, 101], evolutionary algorithms [7], and machine learning through neural networks [3]. A major drawback of these methods is that they require many cost functional evaluations. In the current setting of PDE-constrained optimization, this involves expensive multidimensional unsteady large-eddy simulations (or similar), making them computationally unfeasible. As such, gradient optimization, often combined with the use of adjoint methods, appears a powerful alternative, as the number of cost functional evaluations can be better controlled. Adjoint methods still face many challenges. For example, they require a complete model of the flow equations, the mathematical framework to adjoint the equations, and the numerical tools to perform the corresponding sensitivity calculations. All of these steps are highly non-trivial in a multiphase setting. Furthermore, as the problems are in general nonlinear, gradient methods are only guaranteed to converge to local minima, unlike some families of stochastic algorithms. Finally, in the presence of discontinuities (shocks or contact discontinuities), numerical methods have used smoothing techniques to regularize the equations, e.g. sponge zones for compressible flows, modifying the gradient and making the subsequent implications in the formulation difficult to pinpoint.

The first seminal papers on gradient methods in fluid dynamics focused on aerodynamic shape design [86, 49]. Since then, they have been extended to tackle more challenging problems like turbulent channel flows [72, 11], compressible jets [32], separated flows [78] and mixing layers ([55, 108]). In a liquid-gas flow setting, studies have been performed successfully for diffuse interface methods, where discontinuities are smoothed over a few cells [35, 44]. For sharp interface methods, only recently have adjoint methods emerged, due to the mathematical challenges posed by discontinuous variables and jump conditions across the interface. High-fidelity shape optimization of axisymmetric viscous drops has been tested successfully using boundary integral methods [29]. Control of immersed objects with a free-surface have also been demonstrated [56]. Promising results were shown on controlling interfacial flows using an algebraic Volume-of-Fluid (VOF) method for simpler potential flows [30].

In this chapter, we present fully two-way coupled adjoint equations for the optimization of liquid-gas flows with a sharp treatment of the interface. The adjoint derivation begins with the level set equation which solves for a continuous variable (i.e. signed distance function away from the interface) and as a result, allows a direct linearization of the equations. However, the phase transport equations in the forward problem is solved using a geometric Volume-of-Fluid method. This hybrid formulation (VOF in the forward calculation and level set in the backwards calculation) ensures that the liquid-gas flow model is discretely mass-conserving and makes the adjoint framework tractable. We discuss a solution method to the solve the adjoint equations which involves the use of a novel geometric transport method to transport surface quantities. This geometric transport method can be extended to a larger class of problems, such as the transport of surfactants and electric charge. In order to verify our formulation, we check the accuracy of the

adjoint-based gradient against analytical or finite-difference approximated gradients. We show that cost functionals involving surface integrals exhibit larger errors than those with volume integrals – a consideration that must be taken into account for verification against gradients calculated from finite-difference approximations. The cases we consider for gradient verification are velocity matching problems in a lid-driven cavity flow and a multiphase Couette flow, a centroid matching problem for a drop, and a surface area maximization problem for a drop placed in a steady-state Couette flow. Following verification, we perform optimization on a series of liquid-gas flow problems, such as controlling the inflow velocity to move a drop to a desired position and to levitate a drop. To conclude, we optimize the initial velocity profile to maximize wave growth in a temporally evolving liquid-gas mixing layer. Although the adjoint equations are two-way coupled, results here show that simpler one-way coupling leads to low gradient errors and produces usable, non-trivial optimal solutions for a range of conditions. As such, we leave the two-way coupling for a future study.

The Chapter is organized as follows. In Section 4.3 we discuss the mathematical formulation, including the two-phase flow equations, the adjoint equations, and the optimization setup. Section 4.4 details the surface transport method for the adjoint level set. Section 4.5 shows the accuracy of our gradient calculation and Section 4.6 validates our method by demonstrating control on a number of model problems. Finally, Section 4.7 draws conclusions and details future work.

4.3 Mathematical Formulation

In this section, we will discuss the general formulation of the optimization problem and the explicit expression of the flow equations. We consider a continuous adjoint approach (also referred to as *differentiate-then-discretize*) to formulate the PDE-constrained optimization problem for two-phase flows. Figure 4.1 illustrates a typical domain Ω used, where $\partial\Omega_c$ is a control boundary, $\partial\Omega_d$ is a Dirichlet boundary, $\partial\Omega_o$ is an outflow boundary, and Γ is the interface. To make the handling of the interface in the derivation of the adjoint equations tractable, we include the following assumptions:

a) The interface Γ does not intersect the domain boundary $\partial\Omega = \partial\Omega_c \cup \partial\Omega_d \cup \partial\Omega_o$. This would require handling surfaces with boundary and the resulting conditions at the contact points, which we leave for future work.

b) The interface Γ is assumed to consist of a set of closed surfaces with a uniquely defined curvature at every point. This is required to meaningfully linearize all the quantities present in the two-phase Navier–Stokes equations.

Under these simplifying assumptions, the adjoint formulation does not account for the interface exiting the domain through the outflow boundary $\partial\Omega_o$ nor does it account for topology changes. We will show that, despite the latter assumption, numerical results are still accurate in the presence of topology change, as the interface reconstruction regularizes the topology change event instantaneously. Extending the theoretical formulation to relax these assumptions is left for future work.

4.3.1 Adjoint-based Gradient Optimization

Adjoint methods are used in conjunction with gradient descent methods as a way to provide efficient access to first- and higher-order derivatives. Their main benefits are the straightforward inclusion of constraints and efficient handling of different types of controls. In the most general sense, we consider a PDE-constrained optimization problem of the form

$$\begin{cases} \min\limits_{\boldsymbol{g}_c \in \mathcal{G}} \mathcal{J}(\boldsymbol{g}_c, \boldsymbol{q}(\boldsymbol{g}_c)), \\ \text{subject to } \mathcal{F}(\boldsymbol{g}_c, \boldsymbol{q}(\boldsymbol{g}_c)) = 0, \end{cases} \tag{4.1}$$

where $\boldsymbol{g}_c \in \mathcal{G}$ are the control parameters in an admissible set $\mathcal{G}$, $\boldsymbol{q}$ are the state variables, $\mathcal{J} : \mathcal{G} \to \mathbb{R}$ is a cost functional, and $\mathcal{F}$ are the constraints of the problem. For multiphase flows, the constraints include the two-phase Navier–Stokes equations with appropriate boundary conditions and initial conditions. A Lagrangian $\mathcal{L}$ is introduced to turn the constrained optimization problem into an unconstrained optimization problem. Abstractly, it can be written as

$$\mathcal{L}(\boldsymbol{g}_c, \boldsymbol{q}, \boldsymbol{q}^*) = \mathcal{J}(\boldsymbol{g}_c, \boldsymbol{q}) - \langle \boldsymbol{q}^*, \mathcal{F}(\boldsymbol{g}_c, \boldsymbol{q}) \rangle, \tag{4.2}$$

where $\boldsymbol{q}^*$ are the adjoint variables (sometimes referred to as Lagrange multipliers or costate variables) and $\langle \cdot, \cdot \rangle$ is an appropriate bilinear mapping. Here, the state variables are given by $\boldsymbol{q} \triangleq (p, \boldsymbol{u}, \phi)$ (see Section 4.3.3), where p is the pressure, $\boldsymbol{u}$ is the velocity field, and ϕ is the level set function that determines the interface. The adjoint variables are given by $\boldsymbol{q}^* \triangleq (p^*, \boldsymbol{u}^*, \phi^*)$ (see Section 4.3.4). The problem then reduces to finding a stationary point of the Lagrangian. Taking the directional derivatives with respect to the problem variables $(\boldsymbol{q}, \boldsymbol{q}^*, \boldsymbol{g}_c)$ results in the first-order

optimality conditions

$$\frac{\partial \mathcal{L}}{\partial \boldsymbol{q}^*}[\tilde{\boldsymbol{q}}^*] = 0 \implies \mathcal{F}(\boldsymbol{g}_c, \boldsymbol{q}) = 0, \qquad \text{(state equations)}$$

$$\frac{\partial \mathcal{L}}{\partial \boldsymbol{q}}[\tilde{\boldsymbol{q}}] = 0 \implies \left(\frac{\partial \mathcal{F}}{\partial \boldsymbol{q}}\right)^* [\boldsymbol{q}^*] = \frac{\partial \mathcal{J}}{\partial \boldsymbol{q}}, \qquad \text{(adjoint equations)}$$

and the gradient of the cost functional with respect to the control, that takes the constraints into account,

$$\frac{\partial \mathcal{L}}{\partial \boldsymbol{g}_c}[\tilde{\boldsymbol{g}}_c] = \frac{\mathrm{d}\mathcal{J}}{\mathrm{d}\boldsymbol{g}_c}[\tilde{\boldsymbol{g}}_c]. \qquad \text{(gradient formula)}$$

The main difficulty in applying the adjoint method to the two-phase Navier–Stokes system lies in developing the adjoint equations themselves. In particular, this is due to the state variables $\boldsymbol{q}$ including the interface location, represented here by a level set function ϕ or a liquid volume fraction α. Linearizing the state equations with respect to perturbations in the interface location requires careful analysis and application of the theory of shape calculus introduced by [49] and fully developed in [23, 73].

The required concepts and derivation are presented in Appendix A.1 and Appendix A.2, respectively, while the following sections present the main results. Section 4.3.2 discusses the cost functional considered, its gradient, and the general optimization algorithm. Section 4.3.3 presents the forward flow equations with boundary, inflow, and jump conditions. Finally, Section 4.3.4 presents the resulting adjoint equations.

4.3.2 Cost functional, Gradient and General Optimization Algorithm

To derive the adjoint equations, we consider a sufficiently general cost functional of the form

$$\mathcal{J} = c_1 \int_0^T j_\Omega \,\mathrm{d}t + c_2 j_{\Omega_T} + c_3 \int_0^T j_\Gamma \,\mathrm{d}t + c_4 j_{\Gamma_T}, \tag{4.3}$$

where $c_i \in \mathbb{R}$ are weights for each term and T is the final time. Subscripts denote an evaluation of a term over the specified spatial and temporal location. A cost function of this form allows the control problem to optimize spatially over the domain and interface and temporally for all time and the final time (or any linear combination thereof). For example, j_Ω is evaluated in the domain at a time t while j_{Γ_T} is evaluated on the interface at the final time T. It is assumed here that all terms in the cost are functions of the velocity field $\boldsymbol{u}$ and the level set function ϕ only. We do not consider the pressure p in the cost functional, as this would change the character of the adjoint system. The gradient $\nabla_{\boldsymbol{g}_c}\mathcal{J}$ is obtained from the directional derivative of the Lagrangian $\mathcal{L}$ defined in eq. (4.2) by applying Riesz Representation Theorem, i.e.

$$\frac{\partial \mathcal{L}}{\partial \boldsymbol{g}_c}[\tilde{\boldsymbol{g}}_c] = \frac{\mathrm{d}\mathcal{J}}{\mathrm{d}\boldsymbol{g}_c}[\tilde{\boldsymbol{g}}_c] = \frac{\partial \mathcal{J}}{\partial \boldsymbol{g}_c}[\tilde{\boldsymbol{g}}_c] - \left\langle \boldsymbol{q}^*, \frac{\partial \mathcal{F}}{\partial \boldsymbol{g}_c}(\boldsymbol{q}) \right\rangle = \langle \nabla_{\boldsymbol{g}_c}\mathcal{J}, \tilde{\boldsymbol{g}}_c \rangle. \tag{4.4}$$

As shown, the gradient has a strong dependence on the choice of bilinear mapping and control parameters. These choices will be investigated as part of the numerical results from Section 4.5. In most situations, the gradient can be directly extracted from the directional derivative by employing an L^2 inner product. However, other choices can result in improved smoothness of the control, as discussed, e.g., in [14].

The gradient optimization algorithm employed in this work is a standard steepest descent-type algorithm (see e.g. [39]). The update is given by

$$\mathbf{g_c}^{(k+1)} = \mathbf{g_c}^{(k)} - \alpha_s^{(k)} \nabla_{\boldsymbol{g}_c} \mathcal{J}^{(k)}, \tag{4.5}$$

where $\alpha_s^{(0)} \equiv 1$ and

$$\alpha_s^{(k)} = \frac{\|(\boldsymbol{g}_c^{(k)} - \boldsymbol{g}_c^{(k-1)}) \cdot (\nabla_{\boldsymbol{g}_c} \mathcal{J}^{(k)} - \nabla_{\boldsymbol{g}_c} \mathcal{J}^{(k-1)})\|}{\|\nabla_{\boldsymbol{g}_c} \mathcal{J}^{(k)} - \nabla_{\boldsymbol{g}_c} \mathcal{J}^{(k-1)}\|^2}. \tag{4.6}$$

For an optimization iteration k, a calculation of the gradient $\nabla_{\boldsymbol{g_c}} \mathcal{J}$ is needed. Calculating $\nabla_{\boldsymbol{g_c}} \mathcal{J}$, evaluated from $(\boldsymbol{q}, \boldsymbol{q}^*, \boldsymbol{g_c})$, requires solving the state and adjoint equations to obtain the solutions $(\boldsymbol{q}, \boldsymbol{q}^*)$. For time-dependent problems, the state equations are solved forward in time, while the adjoint equations transport the sensitivities backwards in time. Due to the nonlinearity of the problem, the adjoint equations require knowledge of the state solution for all the spatial and temporal instances considered. Note that this requires some form of checkpointing of the state variables. For high-fidelity simulations, checkpointing can become a non-trivial bottleneck due to the disk space requirements. There is significant literature on optimal checkpointing strategies, e.g. [38], and applications to complex problems, e.g. [96, 12]. In this work, we focus on two-dimensional simulations, for which this type of issue is less pronounced and allows for a more naive approach. Figure 4.2 summarizes our optimization algorithm.

4.3.3 Forward Problem: Two-phase Flow Equations

We consider a two-phase flow described by the incompressible Navier–Stokes equations. The phases are assumed to be immiscible and there is no phase change at the interface. We allow for the presence of a constant surface tension force at the

interface, modeled by the Young-Laplace law. The flow equations are then given by

$$\begin{aligned}
&\text{(continuity)} && \nabla \cdot \boldsymbol{u} = 0, && [0,T] \times \Omega,\\
&\text{(momentum)} && \rho \boldsymbol{u}_t + \rho \boldsymbol{u} \cdot \nabla \boldsymbol{u} = -\nabla p + \nabla \cdot \left[\mu \left(\nabla \boldsymbol{u} + \nabla \boldsymbol{u}^T\right)\right] + \boldsymbol{f}, && [0,T] \times \Omega\\
&\text{(initial condition)} && \boldsymbol{u}(0, \boldsymbol{x}) = \boldsymbol{u}_0, && \Omega,\\
&\text{(outflow)} && \mu \boldsymbol{n}_b \cdot \left(\nabla \boldsymbol{u} + \nabla \boldsymbol{u}^T\right) - p \boldsymbol{n}_b = 0, && [0,T] \times \partial\Omega_o,\\
&\text{(controlled)} && \boldsymbol{u}(t, \boldsymbol{x}) = \boldsymbol{g}_c, && [0,T] \times \partial\Omega_c,\\
&\text{(Dirichlet)} && \boldsymbol{u}(t, \boldsymbol{x}) = \boldsymbol{u}_d, && [0,T] \times \partial\Omega_d,
\end{aligned} \tag{4.7}$$

where ρ is the density, μ is the dynamic viscosity, $\boldsymbol{n}_b$ is the domain boundary exterior normal vector and $\boldsymbol{f}$ contains additional body force terms (e.g. gravity). At the interface Γ, we consider the jump conditions (see [110])

$$\begin{aligned}
&\text{(velocity jump)} && [\![\boldsymbol{u}]\!] = 0,\\
&\text{(traction jump)} && [\![p]\!] = \sigma\kappa + 2[\![\mu]\!](\boldsymbol{n} \cdot \nabla \boldsymbol{u}) \cdot \boldsymbol{n},
\end{aligned} \tag{4.8}$$

where $[\![\cdot]\!]$ is the jump operator, that gives the difference between the liquid and the gas quantities across the interface, σ is the surface tension coefficient, κ is the total curvature (sum of the principal curvatures) and $\boldsymbol{n}$ is the interface normal vector, pointing towards the liquid phase. The phase transport equation can described by the advection of the liquid volume fraction α, i.e.,

$$\begin{aligned}
&\text{(evolution)} && \alpha_t + \boldsymbol{u} \cdot \nabla \alpha = 0, && [0,T] \times \Omega,\\
&\text{(initial condition)} && \alpha(0, \boldsymbol{x}) = \alpha_0 && \Omega,\\
&\text{(inflow)} && \alpha(t, \boldsymbol{x}) = \alpha_i, && [0,T] \times \partial\Omega_c,
\end{aligned} \tag{4.9}$$

or, alternatively, by the advection of a level set function ϕ whose zero level set determines the interface, i.e.,

$$\begin{aligned} &\text{(evolution)} && \phi_t + \boldsymbol{u} \cdot \nabla \phi = 0, && [0,T] \times \Omega, \\ &\text{(initial condition)} && \phi(0, \boldsymbol{x}) = \phi_0 && \Omega, \\ &\text{(inflow)} && \phi(t, \boldsymbol{x}) = \phi_i, && [0,T] \times \partial\Omega_c. \end{aligned} \tag{4.10}$$

In practice, we solve eq. (4.9) for the liquid volume fraction α in the forward problem. Across the interface, α is highly discontinuous whereas ϕ is smoothly varying and therefore, we propose to start the adjoint derivation from a level set formulation described by eq. (4.10). As will be discussed in Section 4.3.4, this hybrid approach of VOF in the forward and adjoint level set in the backward adds essentially no complexity.

The phase transport equation given by eq. (4.9) is solved with a geometric, semi-Lagrangian Volume-of-Fluid method (VOF). The velocity flow solver is second-order accurate in time and space except near the interface, where discontinuities degrade the methods and introduce first-order errors. Details on the discretization are further described in [25, 83, 79, 16]. Inside each computational cell, the interface is represented locally as a plane using piecewise linear interface reconstruction (PLIC) with the plane normal calculated using ELVIRA [85]. The curvature of the interface is calculated using height functions [81]. The pressure jump due to this curvature is then embedded as a source term in the pressure Poisson equation using a continuous surface force approach [87].

4.3.4 Backward Problem: Adjoint Equations

The adjoint equations for the two-phase Navier–Stokes system presented in Section 4.3.3 are derived in Appendix A.2. We summarize the resulting equations here, highlight some key features and proceed to discuss their discretization in Section 4.4. These equations solve for the adjoint variables (also referred to as the sensitivities) $\boldsymbol{q}^* \triangleq (p^*, \boldsymbol{u}^*, \phi^*)$ where p^* is the adjoint pressure, $\boldsymbol{u^*}$ is the adjoint velocity, and ϕ^* is the adjoint level set. Due to the choice of the cost functional $\mathcal{J}$ given by eq. (4.3), the adjoint equations have a similar form to the state equations (e.g. the adjoint velocity field is also solenoidal). The adjoint Navier–Stokes equations are given by

$$\begin{aligned}
&\text{(adjoint continuity)} && -\nabla\cdot\boldsymbol{u}^* = 0, && [0,T]\times\Omega,\\
&\text{(adjoint momentum)} && -\rho\boldsymbol{u}^*_t - \rho\boldsymbol{u}\cdot\nabla\boldsymbol{u}^* + \rho\boldsymbol{u}^*\cdot\nabla\boldsymbol{u}^T && [0,T]\times\Omega,\\
& && \quad = -\nabla p^* + \nabla\cdot\left[\mu\left(\nabla\boldsymbol{u}^* + \nabla\boldsymbol{u}^{*T}\right)\right] + c_1\nabla_{\boldsymbol{u}} j_\Omega, &&\\
&\text{(initial condition)} && (\rho\boldsymbol{u}^*)(T,\boldsymbol{x}) = c_2\nabla_{\boldsymbol{u}} j_{\Omega_T}, && \Omega\\
&\text{(outflow)} && \mu\boldsymbol{n}_b\cdot\left(\nabla\boldsymbol{u}^* + \nabla\boldsymbol{u}^{*T}\right) - p^*\boldsymbol{n}_b = -\rho(\boldsymbol{u}\cdot\boldsymbol{n}_b)\boldsymbol{u}^*, && [0,T]\times\partial\Omega_o,\\
&\text{(controlled)} && \boldsymbol{u}^*(t,\boldsymbol{x}) = 0, && [0,T]\times\partial\Omega_c\\
&\text{(Dirichlet)} && \boldsymbol{u}^*(t,\boldsymbol{x}) = 0, && [0,T]\times\partial\Omega_d.
\end{aligned} \tag{4.11}$$

Note that, in the Navier–Stokes equations (both forward and adjoint), the pressure is sometimes defined up to a constant. However, the gradient formula often involves p^* and, as such, the implementation of the adjoint outflow boundary shown in eq. (4.11) is paramount to obtaining a unique adjoint pressure and a subsequently accurate gradient. The jump conditions at the interface are given by

$$\begin{aligned}
&\text{(velocity jump)} && \llbracket\boldsymbol{u}^*\rrbracket = 0,\\
&\text{(traction jump)} && \llbracket p^*\rrbracket = c_3\nabla_{\boldsymbol{u}} j_\Gamma + \phi^* + 2\llbracket\mu\rrbracket(\boldsymbol{n}\cdot\nabla\boldsymbol{u}^*)\cdot\boldsymbol{n},
\end{aligned} \tag{4.12}$$

where $c_3\nabla_{\boldsymbol{u}} j_\Gamma + \phi^*$ takes the place of the surface tension term in the forward problem and carries information about the surface sensitivities. Finally, the adjoint level set equation is given by

$$\begin{aligned}
&\text{(adjoint level set)} && -\phi_t^* - \boldsymbol{u}\cdot\nabla\phi^* = c_1\nabla_\phi j_\Omega + (c_3\nabla_\phi j_\Gamma + f_\Gamma^*)\delta(\phi), && [0,T]\times\Omega,\\
&\text{(initial condition)} && \phi^*(T,\boldsymbol{x}) = c_2\nabla_\phi j_{\Omega_T} + c_4\nabla_\phi j_{\Gamma_T}\delta(\phi) && \Omega,\\
&\text{(inflow)} && \phi^*(t,\boldsymbol{x}) = 0, && [0,T]\times(\partial\Omega\setminus\partial\Omega_c),
\end{aligned} \tag{4.13}$$

where $\delta(\phi)$ is the usual Dirac delta distribution and is used to localize terms to the interface. The first two source terms in the adjoint level set equation depend on the explicit form of the cost functional and can be obtained using the results from Appendix A.1. The remaining source term is dependent on the two-phase Navier–Stokes system can be written as (for the two-dimensional case)

$$\begin{aligned}
f_\Gamma^* = {}& \sigma\left(\boldsymbol{n}\cdot\frac{\partial^2\boldsymbol{u}^*}{\partial s^2} + 2\kappa\boldsymbol{t}\cdot\frac{\partial\boldsymbol{u}^*}{\partial s}\right)\\
&- \boldsymbol{u}^*\cdot[\![\rho\boldsymbol{u}_t + \rho\boldsymbol{u}\cdot\nabla\boldsymbol{u} + \boldsymbol{f}]\!] - [\![\mu\nabla\boldsymbol{u}^*\cdot\left(\nabla\boldsymbol{u} + \nabla\boldsymbol{u}^T\right)]\!]\\
&+ \left\langle\boldsymbol{n}\cdot\mu\left(\nabla\boldsymbol{u}^* + \nabla\boldsymbol{u}^{*T}\right)\right\rangle\cdot[\![\boldsymbol{n}\cdot\nabla\boldsymbol{u}]\!] + \left\langle\boldsymbol{n}\cdot\mu\left(\nabla\boldsymbol{u} + \nabla\boldsymbol{u}^T\right)\right\rangle\cdot[\![\boldsymbol{n}\cdot\nabla\boldsymbol{u}^*]\!],
\end{aligned} \tag{4.14}$$

where s denotes the arc length parametrization of the interface and $\langle\cdot\rangle$ denotes an interfacial average (see Appendix A.2 for details on the result and notation). In eq. (4.14), we can see that the various terms vanish in the single-phase limits $\sigma\to 0$, $[\![\rho]\!]\to 0$ and $[\![\mu]\!]\to 0$, as expected.

The forward problem solves for the liquid volume fraction α given by eq. (4.9). On the other hand, the adjoint derivation starts from the level set equation given by eq. (4.10) and arrives at the adjoint level set equation from eq. (4.13). The level set ϕ can be reconstructed from the interface location given by the liquid volume fraction α using Fast Marching Methods [97]. The level set equation solves for ϕ over the entire domain, but is only really relevant at the interface where $\phi = 0$. The

adjoint level set equation solves for ϕ^* over the entire domain when the volumetric source terms $\nabla_\phi j_{\Omega_T}$ and $\nabla_\phi j_\Omega$ are non-zero. These source terms are non-zero when the cost functional involves the level set function integrated over the volume Ω (or a non-zero measure subset thereof). As the level set function is not unique away from the interface, we do not consider this type of control in this study, i.e., $c_1 = c_2 = 0$. The remaining source terms in the adjoint level set equation are localized at the interface by $\delta(\phi)$. Considering also that ϕ^* only couples to the adjoint Navier–Stokes equations through the adjoint pressure jump, given by eq. (4.12), the adjoint level set reduces to a surface equation. The geometric transport method used to solve it is discussed in Section 4.4.2. The level set appears in the adjoint level set equation explicitly through the source terms arising from the cost functional in eq. (4.13) and the geometric properties of the interface (e.g. κ, $\boldsymbol{n}$, and $\boldsymbol{t}$ in eq. (4.14)). The geometrical quantities are readily available from the forward simulation and are calculated using the volume fraction α. Therefore, ϕ is never calculated explicitly and the adjoint level set equation only involves α. The hybrid approach of using the volume fraction α in the forward problem and adjoint level set ϕ^* in the backward problem adds essentially no complexity.

As mentioned, the adjoint pressure jump couples the adjoint level set equation to the adjoint Navier–Stokes equations. Then, the additional source terms given by eq. (4.14) (referred to here as the two-way coupling terms) couple the adjoint Navier–Stokes equations back to the adjoint level set equation. Although a complete mathematical description of the two-phase, incompressible adjoint equations is presented, we restrict our implementation to only consider problems where the two-way coupled terms are much smaller than the remaining source terms arising from the cost functional (including the initial condition) in the adjoint level set equation, i.e., $\| \int f_\Gamma^* \, \mathrm{d}t \| \ll \| c_3 \int \nabla_\phi j_\Gamma \, \mathrm{d}t + c_4 \nabla_\phi j_{\Gamma_T} \|$. In this case, we set $f_\Gamma^* = 0$.

As will be shown and discussed in Section 4.5.5, we are still capable of performing control effectively when these two-way coupling terms are neglected. We leave their implementation and impact for a future study.

4.4 Numerical Methods

In this section, we discuss the discretization and implementation of the adjoint equations presented in Section 4.3.4. The numerical discretization for the forward equations can be found in [25, 83, 79, 16]. The general solution method for the adjoint Navier–Stokes equations is discussed in Section 4.4.1 along with the implementation of the adjoint outflow boundary condition in Section 4.4.1. The solution method for the adjoint level set is discussed in Section 4.4.2. Algorithm 3 summarizes the solution method for solving the backwards equations.

4.4.1 Adjoint Two-phase Navier–Stokes Discretization

Pressure Projection

The two-phase adjoint Navier–Stokes equations are solved on a 2D staggered Cartesian mesh using a pressure-projection method [21]. Once a forward simulation is performed on $t \in [0, T]$, the forward variables are assumed to be readily available to use in the backwards calculation for all time steps. Suppose the forward problem is discretized by N time steps, with index $n = 0$ corresponding to $t = 0$ and $n = N$ corresponding to $t = T$, then the backward problem will be index by $m = N - n$. The time integration is performed using a first-order explicit Eu-

ler with fluid properties, state variables $\boldsymbol{q}$ and adjoint variables state variables $\boldsymbol{q}$ evaluated at m. Density and viscosity are calculated using the volume fraction α according to

$$\begin{aligned} \rho &= \alpha\rho_l + (1-\alpha)\rho_g, \\ \mu &= \left(\frac{\alpha}{\mu_l} + \frac{1-\alpha}{\mu_g}\right)^{-1}. \end{aligned} \tag{4.15}$$

First, a non-solenoidal adjoint velocity field $\hat{\boldsymbol{u}}^*$ is computed by

$$\begin{aligned} -\frac{\rho\hat{\boldsymbol{u}}^* - \rho\boldsymbol{u}^{*,m}}{\Delta t} = &\underbrace{-\nabla p^{*,m}}_{pressure} + \underbrace{\rho\boldsymbol{u}^m \cdot \nabla\boldsymbol{u}^{*,m}}_{convective} + \underbrace{\nabla\cdot\left[\mu\left(\nabla\boldsymbol{u}^{*,m} + \nabla\boldsymbol{u}^{*,m\,T}\right)\right]}_{viscous} \\ &\underbrace{-\rho\boldsymbol{u}^{*,m}\cdot\nabla\boldsymbol{u}^{*,m\,T} + c_1\nabla_{\boldsymbol{u}}j_\Omega^m}_{source}, \end{aligned} \tag{4.16}$$

where $\Delta t = t^{m+1} - t^m < 0$ is the time step. The right-hand side represents the pressure, convective, viscous, and source terms, respectively. It should be noted that although the time integration is described here to be explicit, it can be formulated implicitly without loss of generality. The convective term is discretized with a first-order downwind scheme, and all other terms are discretized with a second-order central difference scheme. Although this simple discretization limits the accuracy of the gradient, later it will be shown that it is still effective in performing control for the test cases presented. Next, the incremental adjoint pressure $\Phi^{*,m+1}$ is computed by solving the Poisson equation

$$\nabla\cdot\left(\frac{1}{\rho}\nabla\Phi^{*,m+1}\right) = \frac{\nabla\cdot\hat{\boldsymbol{u}}^*}{\Delta t}. \tag{4.17}$$

in conjunction with the adjoint pressure jump eq. (4.12), which is incorporated using a continuum surface force approach [87].

Finally, the adjoint velocity $\boldsymbol{u}^{*,m+1}$ and adjoint pressure $p^{*,n+1}$ are updated

using $\Phi^{*,n+1}$ according to

$$-\frac{\rho \boldsymbol{u}^{*,m+1} - \rho \hat{\boldsymbol{u}}^{*}}{\Delta t} = -\nabla \Phi^{*,m+1} \tag{4.18}$$

$$p^{*,m+1} = p^{*,m} + \Phi^{*,m+1}. \tag{4.19}$$

In the above, eq. (4.16), eq. (4.17) and eqs. (4.18) and (4.19) will be referred to as the *predictor*, *projection*, and *corrector* step respectively. The boundary conditions for the adjoint velocity must be specified at the end of the predictor and corrector steps and for the adjoint pressure, during the projection step. In the case where the forward problem has a periodic boundary condition, the adjoint variables feature the same periodicity. On the uncontrolled boundary $\partial\Omega_d$ and the controlled boundary $\partial\Omega_c$, the adjoint velocity and adjoint pressure boundary conditions are

$$\frac{\partial \Phi^{*,m+1}}{\partial \boldsymbol{n_b}} = 0, \tag{4.20}$$

$$\boldsymbol{u}^{*} = 0, \tag{4.21}$$

where eq. (4.21) is applied at the end of the predictor and eq. (4.20) guarantees that it does not change after the corrector step. The following section will discuss the implementation of the adjoint outflow boundary condition on $\partial\Omega_o$.

Adjoint Outflow Boundary Condition

The adjoint outflow boundary condition shown in eq. (4.11) specifies the adjoint stress on the outflow boundary to be $-\rho(\boldsymbol{u} \cdot \boldsymbol{n_b})\boldsymbol{u}^{*}$ and in this study, we impose an adjoint stress-free condition, i.e.,

$$\mu \boldsymbol{n_b} \cdot \left(\nabla \boldsymbol{u}^{*} + \nabla \boldsymbol{u}^{*T}\right) - p^{*} \boldsymbol{n_b} = 0 \tag{4.22}$$

on $\partial\Omega_o$. This is a common simplification in the forward problem and we briefly describe the implementation of this boundary condition in the context of a pressure-projection method which follows many past works [16, 26, 88].

Because of the staggered grid, the goal is to solve for $\boldsymbol{u}^{*,n+1}$ on $\partial\Omega_o$ and $\Phi^{*,n+1}$ at the cell right before $\partial\Omega_o$. To simplify the notation, suppose that the outflow is the right boundary, i.e, $\boldsymbol{n_b} = \hat{i}$. In this case, eq. (4.22) reduces component-wise to

$$(x-direction) \quad 2\mu\frac{\partial\hat{u}^*}{\partial x} - p^{*,n} = 0 \qquad \partial\Omega_o \tag{4.23}$$

$$(y-direction) \quad \frac{\partial\hat{v}^*}{\partial x} = 0 \tag{4.24}$$

during the predictor step and

$$(x-direction) \quad 2\mu\frac{\partial u^{*,n+1}}{\partial x} - p^{*,n+1} = 0 \qquad \partial\Omega_o \tag{4.25}$$

$$(y-direction) \quad \frac{\partial v^{*,n+1}}{\partial x} = 0 \tag{4.26}$$

during the corrector step. eqs. (4.23) and (4.24) solve for $\hat{\boldsymbol{u}}^*$ and eqs. (4.25) and (4.26) solve for $\boldsymbol{u}^{*,n+1}$ once $p^{*,n+1}$ is known. To solve for $p^{*,n+1}$, the incremental pressure must be calculated. To derive its equation, consider the adjoint incompressibility condition at the cell right before $\partial\Omega_o$

$$\nabla\cdot\boldsymbol{u}^{*,n+1} = \frac{\partial u^{*,n+1}}{\partial x} + \frac{\partial v^{*,n+1}}{\partial y} = 0. \tag{4.27}$$

Expressing $\dfrac{\partial u^{*,n+1}}{\partial x}$ using the difference of eqs. (4.23) and (4.25) and $\dfrac{\partial v^{*,n+1}}{\partial y}$ by applying $\dfrac{\partial}{\partial y}$ to the y component of eq. (4.18), the resulting equation can be shown to be

$$-\frac{\partial}{\partial y}\Big(\frac{\Delta t}{\rho}\frac{\partial \Phi^{*,n+1}}{\partial y}\Big)-\frac{1}{2\mu}\Phi^{*,n+1}=\nabla\cdot\hat{\boldsymbol{u}}^{*} \tag{4.28}$$

This equation is applied to solve for $\phi^{*,n+1}$ at the last cell before the outflow boundary condition.

4.4.2 Adjoint Level Set Equation

The adjoint level set ϕ^* is a surface quantity and as such, we develop a geometric transport method to transport a general surface quantity. This method can be extended to a larger class of problems such as the transport of surfactants or electric charge. ϕ^* can be interpreted as a concentration, defined by the level set sensitivity per unit area. The discrete value of the adjoint level set in cell index by i is a surface averaged value, i.e.

$$\phi_i^*=\frac{M_i}{S_i}=\frac{\int_{\Gamma_i}\phi^*\,\mathrm{d}S}{\int_{\Gamma_i}\mathrm{d}S}, \tag{4.29}$$

where M and S are the integrated adjoint level set sensitivity and surface area in the cell, respectively. To solve the transport given by eq. (4.13), the numerator M and the denominator S are transported separately. Then, ϕ^* is reconstructed through eq. (4.29) (see [48]). The transport of surface area S is discussed in Section 4.4.2, while the transport of M will be discussed in Section 4.4.2.

Surface Area Transport

Surface area evolves according to the transport equation

$$\frac{\partial S}{\partial t}+\boldsymbol{u}\cdot\nabla S=-(\boldsymbol{n}\cdot\nabla\boldsymbol{u}\cdot\boldsymbol{n})S, \tag{4.30}$$

(see e.g. [8, 48] for derivation). Surface area is materially transported with a source term accounting for the surface area creation and destruction through surface dilatation. As mentioned above, in the VOF method, the interface is reconstructed in each computational cell as a plane in 3D (or straight line in 2D) and the resultant polygon from the intersection of the plane and cell is known as PLIC and here denoted by $\mathcal{P}$. The orientation and placement of PLIC is calculated to match the local volume fraction in a cell and to minimize the volume fraction error in neighboring cells through the ELVIRA algorithm [85]. The collection of all PLIC elements in the domain form a discrete representation of the entire interface.

For our method, there exist two underlying fields that represent surface area, one is $A[\mathcal{P}]$ where $A[\cdot]$ is an operator that calculates surface area over a polygon and the other is S which is solved through a geometric transport method. It should be noted that PLIC elements are spatially discontinuous across cells. Their reconstruction is sensitive to the neighboring volume fraction field and a small re-distribution of the local volume fraction can lead to a large relative change in their surface area. Therefore $A[\mathcal{P}]$ can experience spurious time rate of changes of surface area in a cell due to the interface reconstruction rather than the underlying flow. Thus, we are motivated to calculate a smoother surface area field S through the following geometric transport method.

The geometric transport method contains two steps: a geometric advection of the surface represented by PLIC elements and then a special integration over this surface to calculate surface area in all cells. The method is described here for the forward problem but can easily be applied in the backward problem without a loss of generality. The first step involves advecting the vertices of each PLIC polygon at t^n ($\mathcal{P}^n$) to form new polygons that represent the interface at t^{n+1} ($\mathcal{P}^{n\to n+1}$).

The final step is to estimate the surface area, e.g. in cell i at t^{n+1}, by integrating all advected PLIC that intersect this cell according to the equation

$$S_i^{n+1} = \sum_{j \in \mathcal{N}_i} \frac{A[\mathcal{P}_j^{n \to n+1} \cap \Omega_i]}{A[\mathcal{P}_j^n]} S_j^n \tag{4.31}$$

where Ω_i is the volume of cell i and $\mathcal{N}_i$ is a set of indices that the advected PLIC, intersecting cell i, came from, i.e., $\mathcal{N}_i = \{j \mid \mathcal{P}_j^{n \to n+1} \cap \Omega_i \neq \emptyset\}$. $\frac{A[\mathcal{P}_j^{n \to n+1} \cap \Omega_i]}{A[\mathcal{P}_j^n]}$ is the *ratio* surface area of a advected PLIC originating from cell j that intersects cell i to its initial area, and S_j^n is the corresponding *accurate estimation* of the advected surface area. The *ratio* is motivated by the fact that the surface area introduced by the advected PLIC (i.e. $A[\mathcal{P}_j^{n \to n+1} \cap \Omega_i]$) is not accurate, but the ratio of advected area is sufficiently accurate (see [48]). The *ratio* is multiplied by the *accurate estimation* of surface area and the summation over $\mathcal{N}_i$ is present since multiple advected PLIC can intersect a single cell. This type of approach was proposed in [48] and our formulation follows the same ideas with modifications. First, PLIC advection is un-split, i.e. all directions are handled in one step whereas [48] was split. Secondly, our ratio implicitly handles the surface area creation/destruction term during the advection of the PLIC whereas [48] evaluated the term using a finite difference approximation.

Figure 4.4 illustrates an example of the geometric transport method where the surface area in cell i at t^{n+1} is given by

$$S_i^{n+1} = \frac{A[\mathcal{P}_1^{n \to n+1} \cap \Omega_i]}{A[\mathcal{P}_1^n]} S_1^n + \frac{A[\mathcal{P}_2^{n \to n+1} \cap \Omega_i]}{A[\mathcal{P}_2^n]} S_2^n. \tag{4.32}$$

Adjoint Level Set Transport

Each PLIC has an associated adjoint level set value ϕ^*. The transport of M is identical to the surface area transport of eq. (4.31), except that each PLIC is multiplied by its corresponding ϕ^*, i.e.

$$M_i^{n+1} = \sum_{j \in \mathcal{N}_i} \frac{A[\mathcal{P}_j^{n \to n+1} \cap \Omega_i]}{A[\mathcal{P}_j^n]} S_j^n \phi_j^{*,n} \tag{4.33}$$

This accounts for the advection part of the adjoint level-set equation. To finalize, M is normalized by the surface area according to eq. (4.29) and because of the linearity of adjoint level-set equation eq. (4.13), the two-way coupled source terms can be added (if considered) in a multi-step fashion. This gives

$$\phi_i^{*,n+1} = \frac{M_i^{n+1}}{S_i^{n+1}} + \Delta t^n (f_\Gamma^{*,n} + j_\Gamma^{*,n}). \tag{4.34}$$

4.5 Verification

4.5.1 Verification of Surface Area Transport Method

The surface area transport is an essential part of the adjoint level set transport scheme. In this section, we validate and discuss the limitation of the surface area transport method described in Section 4.4.2. We begin by tracking the surface area of a circular material interface placed in a steady state Couette flow. Figure 4.5 illustrates the setup of this problem. The top and bottom walls are moving at $\pm V_w$, the density and viscosity ratios are 1 and there is no surface tension present. The domain $[-H/2, H/2]^2$ is discretized with a uniform mesh spacing and $n_x = n_y$ cells in each direction. The drop diameter is $D = H/2$ and the final time is

$T = H/(2U)$. The exact surface area at the final time, used as a benchmark, can be written as

$$A_{exact} = \int_0^{2\pi} r \, \mathrm{d}\theta. \tag{4.35}$$

The interface translation is purely horizontal so $r^2 = x^2 + y^2$, where $x = R\cos\theta + 2V_w yT/H$ and $y = R\sin\theta$. Figure 4.6a shows that the surface area A, calculated by integrating the transported surface area S over the domain is accurate and smooth over time, whereas the value obtained by integrating the PLIC surface area $A[\mathcal{P}]$ exhibits large errors and is spurious in time. Figure 4.6b shows the surface area error at the final time T. It is observed the geometric transport method spatially converges with second-order accuracy, whereas the PLIC-based surface area $A[\mathcal{P}]$ fails to converge.

We also test our method on a 2D deformation of a circle. The center of the circle of diameter $D = 0.3$ is placed at $\boldsymbol{c} = (0, 0.25)$ in a square domain $[-0.5, 0.5]^2$ and is discretized by a uniformly spaced mesh. The velocity field is given by

$$\begin{aligned} u &= -2\sin^2(\pi x)\sin(\pi y)\cos(\pi x)\cos(\pi t/8), \\ v &= 2\sin^2(\pi y)\sin(\pi x)\sin(\pi y)\cos(\pi t/8), \end{aligned} \tag{4.36}$$

which will stretch the circle into a spiral until $t = 4$ and then reverse the flow to compress the spiral back to its initial circular shape at the final time $t = 8$. The previous example involved surface area stretching, while in this case, both interface stretching and compression are present. Cases using 64^2 and 256^2 cells are compared against a benchmark case using 512^2 cells. Figures 4.7a and 4.7b show the interface at $t = 4$ and $t = 8$. The coarse 64^2 case shows significant break up, while the fine 256^2 case does not and is able to return back to its original shape. Figure 4.7c shows the total surface area over time calculated from $A[\mathcal{P}]$ and S. The geometric transport method performs well for the surface area stretching portion,

achieving a value closer to the benchmark than that surface area calculated from PLIC at $t = 4$. However, it struggles in the compression portion. The PLIC based area gets back to the initial surface area at $t = 8$ whereas the geometric transport method systematically struggles to destroy surface area, failing to return to the initial surface area even at fine resolutions.

4.5.2 Verification Exercises for Two-phase Flow Problems

The adjoint formulation yields the gradient $\nabla \mathcal{J}_{adj}$ that will be used in the gradient descent algorithm. This gradient can be verified against an analytical gradient $\nabla \mathcal{J}_{ex}$, if it exists, or a finite difference gradient $\nabla \mathcal{J}_{FD}$, otherwise. However, comparing against a finite difference gradient can be non-trivial in cost functionals pertaining to liquid-gas flow problems.

Figure 4.8 illustrates a test case where a drop is advected by a uniform velocity $(U, 0)$. The goal of this exercise is to find the control parameter U that will bring a drop of diameter D to a desired position $\boldsymbol{x}_d$ at the final time T. The initial and desired positions are separated by a horizontal distance $L = D$. The cost functional can be posed in two ways to accomplish this objective:

$$\mathcal{J} = \frac{1}{2} \int_{\Gamma(T)} \phi_d^2 \, \mathrm{d}S, \tag{4.37}$$

$$\mathcal{J} = \frac{1}{2} \|\boldsymbol{x}_c(T) - \boldsymbol{x}_d\|^2, \quad \boldsymbol{x}_c = \frac{1}{|\Omega_g|} \int_{\Omega_g} \boldsymbol{x} \, \mathrm{d}V. \tag{4.38}$$

The first cost functional is a surface-based integral that attempts to align the transported fluid interface with its target. The latter is a volume-based integral that attempts to match the drop centroid. Here, $\boldsymbol{x}_d = (x_d, 0)$ is the desired position of the center of the drop, and $\phi_d(\boldsymbol{x}) = D/2 - \|\boldsymbol{x} - \boldsymbol{x}_d\|$ is the desired level set

function. The optimal solution is $U_{opt} = L/T$ and results in an minimum $\mathcal{J} = 0$ for both cost functionals. For verification purposes, we will evaluate the gradient at an operating point of $U = L/(2T)$. The domain $[0, 2D] \times [-D, D]$ is discretized by a uniformly spaced mesh with $n_x = n_y$ cells in all directions. The initial spherical drop position is taken to be at $(D/4, 0)$.

Figures 4.9a and 4.9b show the finite difference gradient compared to the analytical one for various mesh sizes and finite difference step sizes ϵ. A few observations are highlighted. First, both exhibit a $\mathcal{O}(\epsilon^{-1})$ scaling at coarse mesh sizes and small finite different sizes. However, this error can be reduced by reducing the mesh size for the volume-based cost functional, whereas the surface-based cost functional retains the issue. This suggests that finite difference gradients for volume-based cost functionals are less spurious than surface-based cost functionals in the ϵ space. It should also be noted that the relative error in the volume-based cost functional is an order of magnitude smaller than in the surface-based cost, e.g., $\epsilon = 10^{-4}, n_x = 16$. To qualify this, suppose that there is an error $e_{\mathcal{J}}$ associated with evaluating the cost functional, i.e.

$$e_{\mathcal{J}} = \mathcal{J}_{ex} - \mathcal{J}_{num},$$

where $\mathcal{J}_{ex}$ is the true cost functional value and $\mathcal{J}_{num}$ is a numerical approximation. Using a first-order finite difference scheme for the gradient approximation evaluated at $\boldsymbol{g}_c$, i.e.

$$\nabla \mathcal{J}_{FD} \approx \frac{\mathcal{J}_{num}(\boldsymbol{g}_c + \epsilon) - \mathcal{J}_{num}(\boldsymbol{g}_c)}{\epsilon}, \tag{4.39}$$

will result in an error of the form

$$e_{FD} = \nabla \mathcal{J}_{FD} - \nabla \mathcal{J}_{ex} = \mathcal{O}(\epsilon) - \frac{e_{\mathcal{J}}(\boldsymbol{g}_c + \epsilon) - e_{\mathcal{J}}(\boldsymbol{g}_c)}{\epsilon}. \tag{4.40}$$

Here, we have assumed $e_{\mathcal{J}}(\boldsymbol{g}_c + \epsilon) - e_{\mathcal{J}}(\boldsymbol{g}_c) \sim \mathcal{O}(\epsilon^k)$ for a given k. Then, eq. (4.40) has an $\mathcal{O}(\epsilon)$ error associated with the finite difference approximation

and an unknown $\mathcal{O}(\epsilon^{k-1})$ error associated with differentiating the error $e_{\mathcal{J}}$. This equation highlights the difficulties of a finite difference approximation, since the resulting error exhibits anomalous behavior and can increase as the finite difference step size is decreased for $k \leq 0$. In single-phase problems, we may expect $e_{\mathcal{J}}$ to be smooth in the ϵ space and $k > 0$. However, for liquid-gas flows using VOF methods and interfaces modeled using spurious PLIC elements, there is no guarantee that $e_{\mathcal{J}}$ is smooth in the ϵ space. As we have seen, the results above suggest that $k \approx 0$ for this setup. Therefore, caution must be taken when verifying the adjoint gradient against a finite difference gradient and analytical gradients should be preferred, if available.

On the other hand, the adjoint calculated gradient only incurs a error e_{disc} due to discretizing the continuous adjoint formulation. Therefore,

$$\nabla \mathcal{J}_{adj} - \nabla \mathcal{J}_{ex} = e_{disc}, \tag{4.41}$$

$$\nabla \mathcal{J}_{adj} - \nabla \mathcal{J}_{FD} = \mathcal{O}(\epsilon) + \frac{e_{\mathcal{J}}(\boldsymbol{g}_c + \epsilon) - e_{\mathcal{J}}(\boldsymbol{g}_c)}{\epsilon} + e_{disc}. \tag{4.42}$$

In the following sections, we will check the adjoint-based gradient using these equations. We will consider a range of test cases for which the source terms in the adjoint equations are summarized in Table 4.1 and the gradient formulas are summarized in Table 4.2.

4.5.3 Case 1: Single-phase Lid Driven Cavity Flow

In this section, we provide a simple test case in the limit of unit viscosity and density ratios with no surface tension to verify the baseline adjoint solver. We consider a lid-driven cavity velocity matching problem, where the cost functional

is

$$\mathcal{J} = \frac{1}{2}\int_{\Omega} \|\boldsymbol{u}(T) - \boldsymbol{u}_d\|^2 \,\mathrm{d}V, \tag{4.43}$$

for a final time T and a desired velocity $\boldsymbol{u}_d$. The control parameter is the lid velocity V_w. For this setup, the adjoint-based gradient is given by

$$\frac{\mathrm{d}\mathcal{J}}{\mathrm{d}V_w} = \int_0^T \int_{\partial\Omega_c} 2\mu \frac{\partial u^*}{\partial y} \,\mathrm{d}x. \tag{4.44}$$

The fluid density and viscosity are $\rho = 1$ and $\mu = 0.1$, respectively. The domain $[-H/2, H/2]^2$ is discretized with a uniform mesh space using 32^2 cells. The fluid initially starts at rest. The simulation is integrated at a viscous CFL of 0.75 until $T = \rho 100 H^2/\mu$. The desired velocity profile $\boldsymbol{u}_d$ is obtained by the final time solution for the lid-driven cavity flow case using $V_w = 2$. The adjoint gradient is calculated at an operating point $V_w = 1$. Since the velocity field and correspondingly the cost functional are not known analytically, the adjoint gradient is verified against a finite difference approximation using eq. (4.42). Figure 4.10 shows the gradient error as a function of the finite difference step size ϵ. For large ϵ, the $\mathcal{O}(\epsilon)$ finite difference error dominates and as ϵ is decreased, a plateau is observed due to the discretization errors of the adjoint equations.

4.5.4 Case 2: Two-phase Couette Flow

We verify our adjoint formulation for a velocity matching problem using the cost functional given by eq. (4.43) in a two-phase planar Couette flow. Figure 4.11 illustrates the setup of this problem. The control parameter is again the wall velocity V_w. The fluid initially starts off at rest and evolves to a final time $T = 12$. The long time horizon is sufficient for the fluid to arrive at a steady state. The adjoint-based gradient is again given by eq. (4.44). The fluid properties are

$\mu_l = 1, \mu_g = 0.5$, $\rho_l = \rho_g = 1$, and $\sigma = 0$. Each fluid occupies half of the channel width. The domain $\mathbb{R} \times [-H/2, H/2]$ is discretized by a uniform mesh spacing Δy. The desired profile is the steady state profile at a wall velocity of $V_w = 1$. The gradient is evaluated at an operating point $V_w = 2$. Since the forward problem is analytically known, the gradient is verified using eq. (4.41). Figure 4.12a shows that the adjoint calculated gradient approximates the exact gradient well and converges with $\mathcal{O}(\Delta y^2)$, which is expected in a diffusion problem where the discretization of the viscous term using central difference is second-order accurate. Figure 4.12b shows u^* at $t/T = 1$, which is the initial adjoint velocity profile that diffuses with the boundary condition $u^* = 0$ on $\partial\Omega_c$. Although we do not consider the two-way coupling terms, it is interesting to note that ϕ^* would be non-zero due to the viscosity jump terms in eq. (4.14). However, it would not couple into the x adjoint momentum equation and consequently, it does not affect the gradient calculation. The solution to the y adjoint momentum equation would be $v^* = 0$ and a piece-wise constant adjoint pressure field, where the jump in adjoint pressure exactly balances ϕ^* at the interface.

In the next case, we seek to optimize the surface area of a drop in a steady-state Couette flow, described in Section 4.4.2 and illustrated in fig. 4.5. The domain $[-H/2, H/2]^2$ is discretized with a uniform mesh spacing. The fluid properties of both fluids are $\rho = 1, \mu = 0.1, \sigma = 0$, the drop diameter is $D = 0.5$, the height of the channel is $H = 1$ and the drop is placed at the center of the domain. The cost functional seeks to maximize surface area at the final time, i.e.,

$$\mathcal{J} = -\int_{\Gamma_T} \mathrm{d}S, \tag{4.45}$$

and is controlled by the wall velocity. Although the solution to this optimization problem is $V_w \to \infty$, we verify our method can yield the correct gradient found by

differentiating eq. (4.35) with respect to V_w. The adjoint-based gradient is

$$\frac{\mathrm{d}\mathcal{J}}{\mathrm{d}V_w} = \int_0^T \int_{\partial\Omega_c} 2\mu \frac{\partial u^*}{\partial y}\,\mathrm{d}x\,\mathrm{d}t + \int_\Omega \rho \frac{2y}{H} u^*(0)\,\mathrm{d}\Omega. \tag{4.46}$$

Note that an additional term (as compared to eq. (4.44)) appears in the gradient, since the control V_w is also present in the initial condition. Furthermore, $\partial\Omega_c$ includes both the top and bottom wall. The gradient is evaluated at $V_w = 1$. In the forward problem, the interface gets stretched and rotated purely through a kinematic process. However, in the adjoint problem, the adjoint flow-field is more complex. Figure 4.13a shows that at $t/T = 1$ there exists a zero adjoint velocity field and a non-zero adjoint level set at the interface (see Table 4.1). This adjoint level set is transported backwards in time and feeds into the adjoint velocity through the adjoint pressure jump given by eq. (4.12). Figure 4.13b shows the non-trivial adjoint flow-field at $t/T = 0.5$, as a result of the adjoint pressure jump, convection and diffusion. Figure 4.13c shows the adjoint velocity field at the end of the adjoint calculation, $t/T = 0$, which is integrated as part of the gradient calculation. An interesting observation arises: although the forward problem is purely kinematic, the backwards problems includes advection, diffusion, and singularities at the interface. Figure 4.14 shows that the gradient error converges spatially with first-order accuracy, consistent with the limiting first order downwind scheme of the convective term.

4.5.5 Case 3: Inflow Control of a Drop's Centroid

We will now consider inflow-outflow problems, where we attempt to match the drop centroid to a desired position at the final time using eq. (4.38). Figure 4.8 illustrates the case setup, with the modification that the fluid is initially quiescent.

The control parameter is the inflow velocity U, which is, for now, a constant. The corresponding adjoint-based gradient is given by

$$\nabla_U \mathcal{J} = \int_0^T \int_{\partial\Omega_c} -p^* + 2\mu \frac{\partial u^*}{\partial x} \, \mathrm{d}y \, \mathrm{d}t. \tag{4.47}$$

In the previous sections, we have considered the control parameter to be the wall velocity, which is tangent to the control boundary. In these prior cases, the adjoint pressure was not unique and could vary up to a constant. However, as it did not appear explicitly in the gradient, this was not an issue. This is not true for inflow-outflow problems, since p^* is present in the gradient formula, so a unique adjoint pressure is needed. As described above, a careful implementation of the adjoint outflow boundary condition is necessary for calculating a unique pressure and consequently an accurate gradient.

As a first verification test, we move a drop to a desired position at the final time. The drop diameter is $D = 0.5$, the initial position is $\boldsymbol{x}_0 = (1.5D, 0)$ and the desired position is $\boldsymbol{x}_d = (2.5D, 0)$. The domain $[0, 6D] \times [-D, D]$ is discretized uniformly and the final time is $T = 0.5$. The fluid properties are $\mu_l = 1, \mu_g = 1, \rho_l = 10, \rho_g = 1$ and $\sigma = 0$. Figure 4.16a shows the error of the adjoint-based gradient against the finite difference gradient for various mesh sizes at an operating point of $U = 3$. The gradient error is $\mathcal{O}(\epsilon)$ for large finite difference step sizes and bottoms out at a level corresponding to the discretization error of the adjoint equations as expected. The discretization errors appear large compared to the $\mathcal{O}(\epsilon^{k-1})$ discussed in Section 4.5.2 because of the volume based cost function used.

Figure 4.16b shows that the discretization errors evaluated at $\epsilon = 10^{-3}$ converge with second-order accuracy and exhibit low normalized errors around 1% to 10%, despite our simplifications, such as neglecting the two-way coupled terms eq. (4.14). To qualify this, consider the adjoint level set, which is one-way coupled

to the adjoint pressure jump. This pressure jump creates an adjoint flow field and, specifically, an adjoint stress on the inflow boundary. This adjoint stress is then integrated over time to calculate the gradient. The initial adjoint level set value at $t = T$, as shown in Table 4.1, is determined by how far the drop at the final time is from the desired position. The adjoint simulation integrated backwards in time follows ϕ^* along the interface and increases ϕ^* through the two-way source coupled terms given by eq. (4.14) (if considered). Results demonstrate that the sensitivity coming from the adjoint level set initial value is sufficient in obtaining an accurate and converging gradient. Although the source terms arising from the density differences (and also viscosity differences) are neglected, the formulation should not be thought of as neglecting density and viscosity differences. In fact, the formulation accounts for them through the convective and diffusion terms in the adjoint equations.

4.6 Optimization of Two-phase flows

4.6.1 Case 1: Drop Centroid Matching

Figure 4.15 shows the setup of a drop centroid matching problem, using the cost function eq. (4.38), where the control is a horizontal velocity that varies in space and time, i.e. $(\boldsymbol{g}_c)_j^n = U_j^n$. The gradient is then calculated at discrete points in space and time through

$$(\nabla_U \mathcal{J})_j^n = \left(-p^* + 2\mu \frac{\partial u^*}{\partial x} \right) \Bigg|_j^n . \tag{4.48}$$

The diameter of the drop is $D = 0.5$ and the domain $[0, 12D]^2$ is discretized by 128^2 cells in all directions. The initial drop position is at $\boldsymbol{x}_0 = (2D, 4.5D)$ and

the desired position is $\boldsymbol{x}_d = (6D, 7.5D)$. Because of the different y locations, this problem attempts to create lift on the drop. The fluid properties are $\mu_l = \mu_g = 0.01, \rho_l = 40$ and $\rho_g = 1$. The y boundaries use a periodic boundary condition. The final time is $T = 8$ for which we run two cases where 1) surface tension is $\sigma = 1.0$ and the time step size is $\Delta t = 2 \times 10^{-3}$ and 2) surface tension is $\sigma = 0.2$ and the time step size is $\Delta t = 4 \times 10^{-3}$.

Figure 4.17a shows that in both cases, the optimization procedure described in fig. 4.2 is able to reduce the cost functional by 5 orders of magnitude below its initial value. Figures 4.17b and 4.17c show the complex control solution (taken at $k = 75$, where convergence plateaus) for both cases at $t/T \in \{0.25, 0.5, 0.75\}$ and the initial and desired drop position heights are shown for reference. The control at $t/T = 0.25$ appears bimodal in both cases. In the higher surface tension case, the largest peak appears at a distance $D/2$ below the initial drop position, while the second peak is at a distance D above the initial drop position. In the lower surface tension case, the largest peak appears at a distance $D/4$ below the initial drop position while the second peak is at a distance $D/2$ above the initial drop position. The control then evolves in a complex manner. Figure 4.17d shows the evolution of the interfaces in a zoomed in window. In the higher surface tension case, the drop maintains its circular shape and wobbles to the desired position. In the lower surface tension case, the drop's surface tension cannot keep the drop intact and the drop breaks while being moved to the desired position. However, the adjoint-based optimization framework remains capable of bringing the centroid of the collection of the two drops to the desired position.

4.6.2 Case 2: Drop Levitation

In this section, we levitate a drop that falls under the action of gravity. The cost function we choose to accomplish this is

$$\mathcal{J} = \frac{1}{2}\int_0^T \|\boldsymbol{x}_c(t) - \boldsymbol{x}_d\|^2 \,\mathrm{d}t, \tag{4.49}$$

which is the same cost function as given by eq. (4.38), except integrated over time. This forces the control to consider all time instances instead of just the final time, thereby attempting to match a desired trajectory over the time horizon. The control is a space and time varying inflow velocity U_j^n, as is the case in Section 4.6.2. The gradient formula for this is given by eq. (4.48).

The diameter of the drop is $D = 0.5$ and the domain $[0, 6D] \times [-3D, 3D]$ is discretized by 32^2 cells. The initial drop position is $\boldsymbol{x}_0 = (3D, 2D)$ and the desired position is $\boldsymbol{x}_d = \boldsymbol{x}_0$. The fluid properties are $\mu_l = \mu_g = 0.02, \rho_l = 20, \rho_g = 1$ and $\sigma = 0.5$. The gravitational body force is $\boldsymbol{f} = -0.03\boldsymbol{e}_y$, the final time is $T = 12$, and the top and bottom boundary conditions are slip walls, i.e., $\partial_y u = 0$ and $v = 0$.

Figure 4.18 shows the optimization of this problem starting from an initial 0 guess. Figure 4.18a shows that the optimization is able to reduce the initial cost function value by two orders of magnitude in around 30 iterations. Figure 4.18b shows the control solution (taken at $k = 30$, where convergence plateaus) for various times. The control solution creates regions of positive and negative velocities in order to levitate the drop. Figures 4.19a to 4.19d show the uncontrolled solution where the drop accelerates downward due to gravity. Figures 4.19e to 4.19h show the controlled solution. A significant improvement is observed as the inflow velocity creates a re-circulation to maintain the drop's initial position. Only near the final time $t/T = 1$ does the drop deviate slightly from its objective. This is

because sensitivities are initially 0 at $t/T = 1$ and as such, the control is inherently weak towards the end of the time horizon. Easy improvements can be made such as adding a final time centroid matching term to the cost function or optimizing for a longer time horizon than the time window of interest.

4.6.3 Case 3: Temporally Evolving Mixing Layer

Figure 4.20 shows the setup of a temporally evolving mixing layer, where a gas layer of height H_g sits on top of a liquid layer of height H_l. The interface is initially perturbed by a sum of sinusoidal waves with modes $8, 10, 12, \ldots, 26$, phases that are uniformly distributed and amplitudes of size 0.2 times the mesh size. The cost function attempts to maximize liquid entrainment through the cost functional

$$\mathcal{J} = \frac{1}{2}(y_c(T) - y_d)^2, \quad y_c(T) = \frac{1}{|\Omega_g(T)|}\int_{\Omega_g(T)} y \, \mathrm{d}V, \tag{4.50}$$

where $y_c(T)$ is the vertical position of the liquid centroid and y_d is a sufficient large distance above the interface, chosen to be H_g in this study. A baseline velocity profile is given by

$$u_b = \begin{cases} U_g \mathrm{erf}(y/\delta_g), & y \geq 0, \\ U_l \mathrm{erf}(y/\delta_l), & y < 0, \end{cases} \tag{4.51}$$

where U is the free-stream velocity, δ is the vorticity thickness, and subscripts l and g denote liquid and gas quantities, respectively. The control parameters are the discrete initial velocities of $u_0(y_j)$ and are subjected to the inequality constraint

$$\int_{-H_l}^{H_g} (u_0 - u_b)^2 \, \mathrm{d}y \leq \int_{-H_l}^{H_g} (\eta u_b)^2 \, \mathrm{d}y, \tag{4.52}$$

which limits the variance of the initial velocity profile relative to the baseline profile through the factor η. The free-stream velocities are $U_l = 0.1$ and $U_g = 1$, and the

vorticity thicknesses are $\delta_g = 1$ and $\delta_l = 1$. The domain size $[0, 96\delta_g] \times [-H_l, H_g]$, where $H_l = 12\delta_g$ and $H_l = 36\delta_g$, is discretized by a uniformly spaced mesh with 512×256 cells. The fluid properties are $\mu_l = 0.0125, \mu_g = 0.00125, \rho_l = 10, \rho_g = 1$ and $\sigma = 1.0$. The final time is $T = 200\delta_g/U_g$. The top and bottom boundary conditions are slip walls and the lateral boundary conditions are periodic.

Figure 4.21 shows the optimal initial velocity profile for three separate optimization cases using $\eta \in \{0.01, 0.05, 0.1\}$ which is taken at $k \in \{12, 15, 15\}$, respectively. The initial velocity profile for all three cases increases the shear at the interface by distributing the velocity fluctuations allowed by the constraint, in a neighborhood around interface. As η is increased, the initial velocity profile is allowed more freedom to deviate from the baseline profile and more interesting features appear, such as the multi-shear layer in the gas observed for $\eta = 0.1$. The optimization is solved using a standard penalty method and fig. 4.21b illustrates that all three η are able to satisfy the constraint. As the cost function is quite arbitrary since y_d is some sufficient distance above the interface, we choose to plot the difference of centroid at the final time between the optimal solution $y_c(T)$ and the baseline velocity profile $y_c^{(0)}(T)$, normalized by δ_g. The result is shown in fig. 4.21c. As η is increased, the relative change in centroid increases. Figure 4.22 confirms this as a more corrugated, entrained liquid is observed as η is increased.

4.7 Conclusion

In this paper, we have presented a continuous adjoint formulation for liquid-gas flows using a sharp interface model. We have then used this formulation to demonstrate computational control of liquid-gas flows at moderate Reynolds number.

We have opted for a hybrid formulation, which uses a geometric Volume-of-Fluid (VOF) method in the forward calculation, but relies on a level set method in the backwards calculation. Verification and optimization test cases are shown using one-way coupling in the adjoint equations. We highlighted key features of the implementation of the adjoint equations. A continuum surface force (CFS) method was implemented in the backwards solver to address the adjoint pressure jump [87]. An adjoint outflow boundary condition was used to get a unique adjoint pressure, and subsequently an accurate gradient for inflow-outflow control problems [16, 26, 88]. Finally, a new geometric transport method for surface quantities, using the underlying PLIC, was presented and used for the adjoint level set transport equation.

This formulation was verified by checking the adjoint-based gradient against analytical and finite-difference approximated gradients. We have shown that for liquid-gas flows the finite difference gradient can exhibit $\mathcal{O}(\epsilon^{-1})$ scaling for small finite difference step sizes ϵ when using surface-based cost functionals. As such, volume-based cost functionals were preferred over surface-based cost functionals (at least for verification). We showed mesh converge in a velocity matching cost functional for a lid-driven cavity flow and a planar two-phase Couette flow. Moreover, we showed similar convergence for a surface area maximization problem, where a material interface was placed in a steady-state Couette flow. As a final verification step, we presented converging gradients for a drop centroid matching problem in an inflow-outflow configuration.

As a demonstration of the ability of the proposed framework for control, we showed the ability to produce non-trivial control solutions to move a drop to a horizontally and vertically displaced position using a time and space varying hor-

izontal inflow velocity. Furthermore, we demonstrated the control capability on a problem where we levitated a drop falling under the action of gravity. Finally, we demonstrated the ability to control the initial velocity profile to maximize growth of a temporally evolving liquid-gas mixing layer under a set of optimization constraints.

Under the current framework, we were able to perform control exercises for a range of liquid-gas flow problems; yet opportunities still arise. For a single drop, increasing the Reynolds number and lowering the Weber number would be useful in understanding the limitations of this method, as different physics such as turbulence and break-up, become more important. A more theoretically-grounded effort to account for topology would be useful. Although encouraging results suggest that the adjoint formulation may be capable of handling topology change, further testing is required. Extending this work to allow the inflow of two-fluids (as opposed to one in the current setting) would create more opportunity for a wider range of problems to be studied. This would likely create more source terms in the adjoint formulation and more theoretical development and verification would be needed. A three-dimensional extension would result in more realistic surface tension physics, without much change in the existing formulation. Finally, further effort in discretizing and evaluating the impact of the two-way coupled terms on the adjoint-based gradient would prove extremely useful in gaining a better understanding of the adjoint equations and their impact on optimization of such flows.

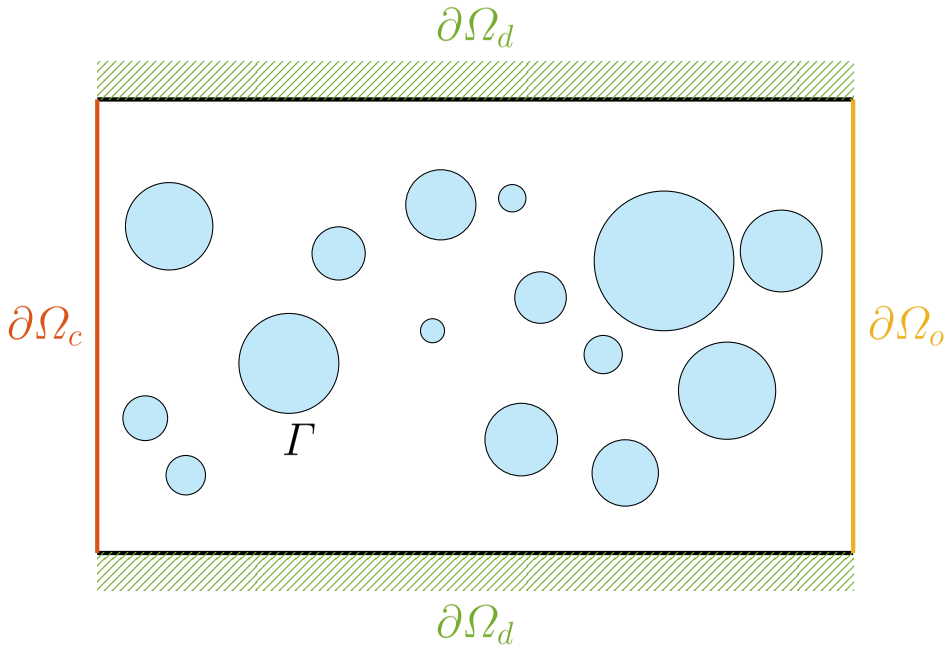

Figure 4.1: Typical domain Ω considered in this work with an interface Γ, controlled inflow $\partial\Omega_c$, boundary using Dirichlet conditions $\partial\Omega_d$ and an outflow $\partial\Omega_o$.

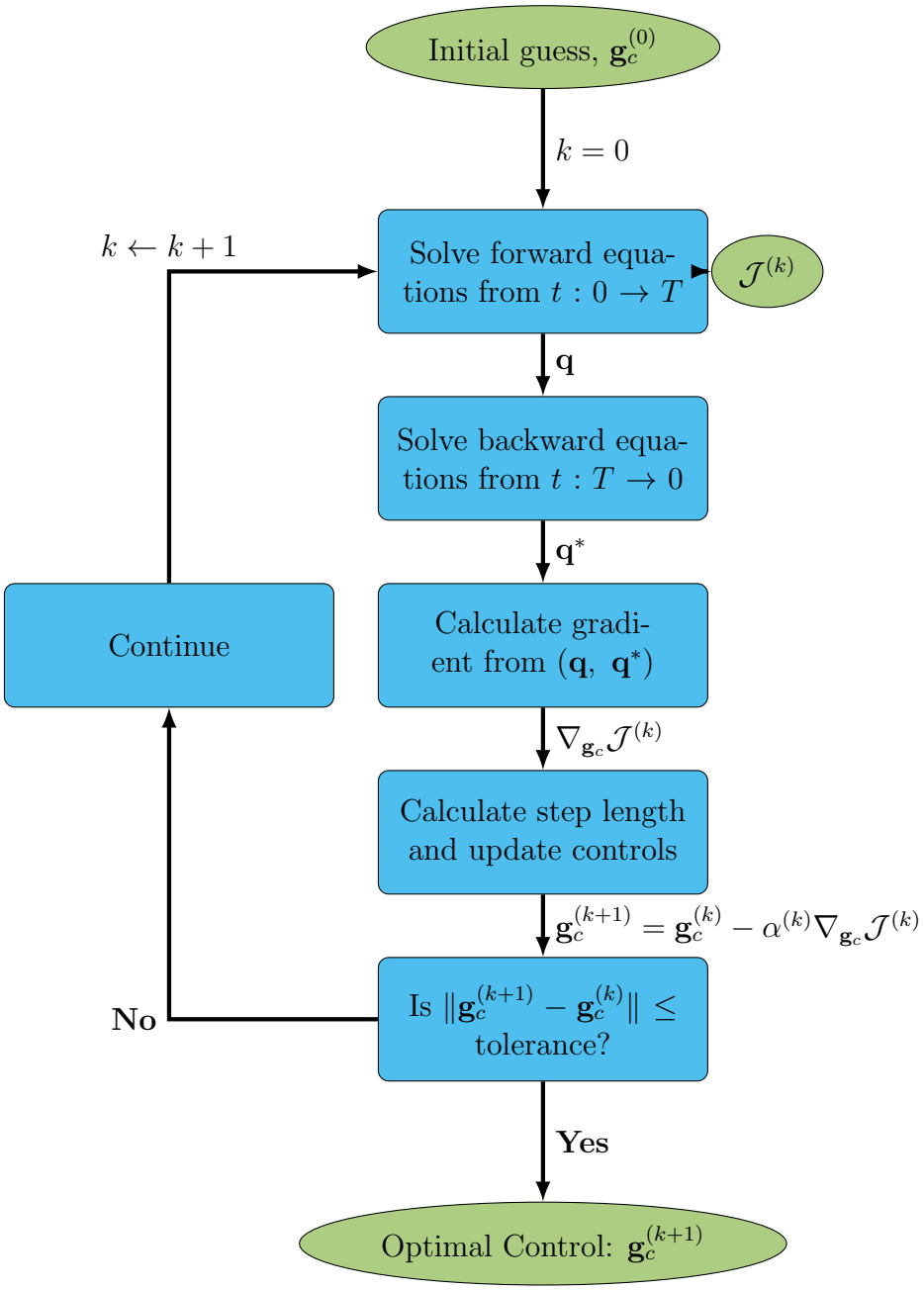

Figure 4.2: Simple adjoint optimization algorithm employed here.

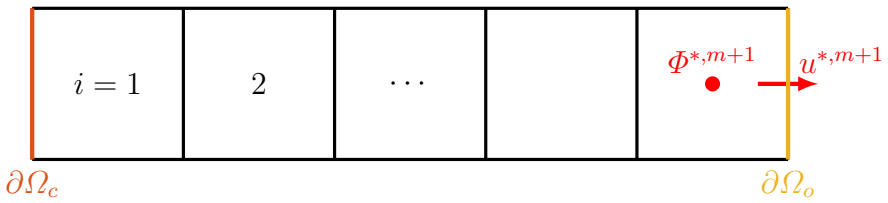

Figure 4.3: Example of adjoint outflow boundary condition setup assuming the normal boundary $\boldsymbol{n}_b = \hat{i}$. $\partial\Omega_c$ is the controlled inflow boundary, $\partial\Omega_o$ is the outflow boundary, and $\boldsymbol{u}^{*,m+1}$ is solved for on $\partial\Omega_o$ and $\Phi^{*,m+1}$ at the cell adjacent to $\partial\Omega_o$.

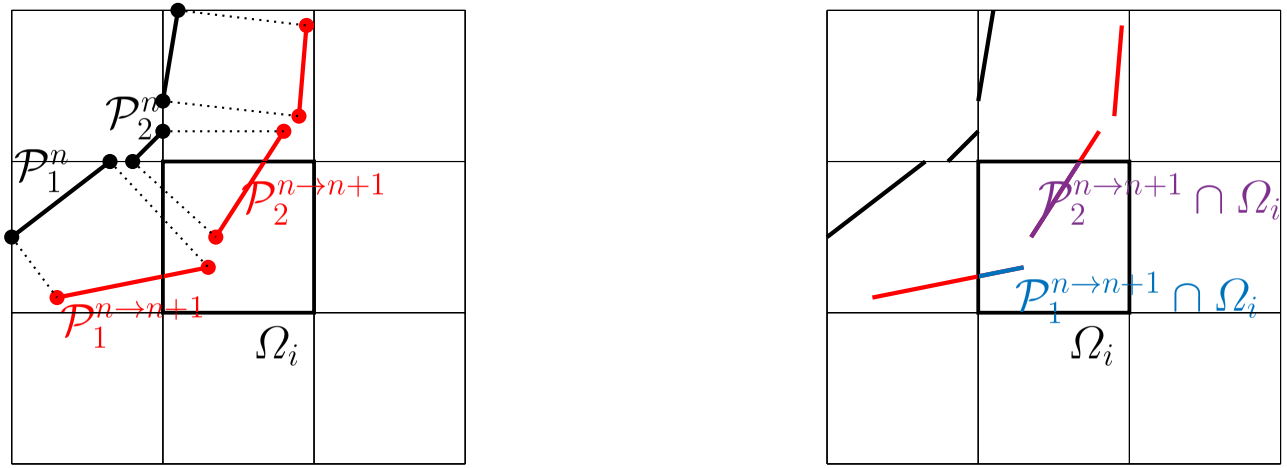

Figure 4.4: Animation of surface transport method: a) PLICs at n shown in black whose vertices are advected forward in time. The resultant PLICs are shown in red and b) their intersection with cell Ω_i are shown in purple and blue.

Algorithm 3 General algorithm for adjoint solution

1: **Input:** $\boldsymbol{q}^{*,n}$, $\boldsymbol{q}^{n}$ in Ω and on $\partial\Omega$
2: Solve for $\phi^{*,n+1}$ using eq. (4.13);
3: Compute ρ^{n} μ^{n} using eq. (4.15);
4: Solve for $\hat{\boldsymbol{u}}^{n}$ in Ω using eq. (4.16);
5: Solve for $\hat{\boldsymbol{u}}^{n}$ on $\partial\Omega_c \cup \partial\Omega_d$ using eq. (4.21) and on $\partial\Omega_o$ using eqs. (4.23) and (4.24);
6: Solve for $\boldsymbol{\Phi}^{*,n+1}$ in Ω using eqs. (4.17) and (4.28) coupled with eq. (4.12) and $\phi^{*,n+1}$;
7: Update $\boldsymbol{u}^{*,n+1}$ and $p^{*,n+1}$ in Ω using eqs. (4.18) and (4.19);
8: Solve for $\boldsymbol{u}^{*,n+1}$ on $\partial\Omega_o$ using eqs. (4.25) and (4.26);
9: **Output:** $\boldsymbol{q}^{*,n+1}$ in Ω and on $\partial\Omega$

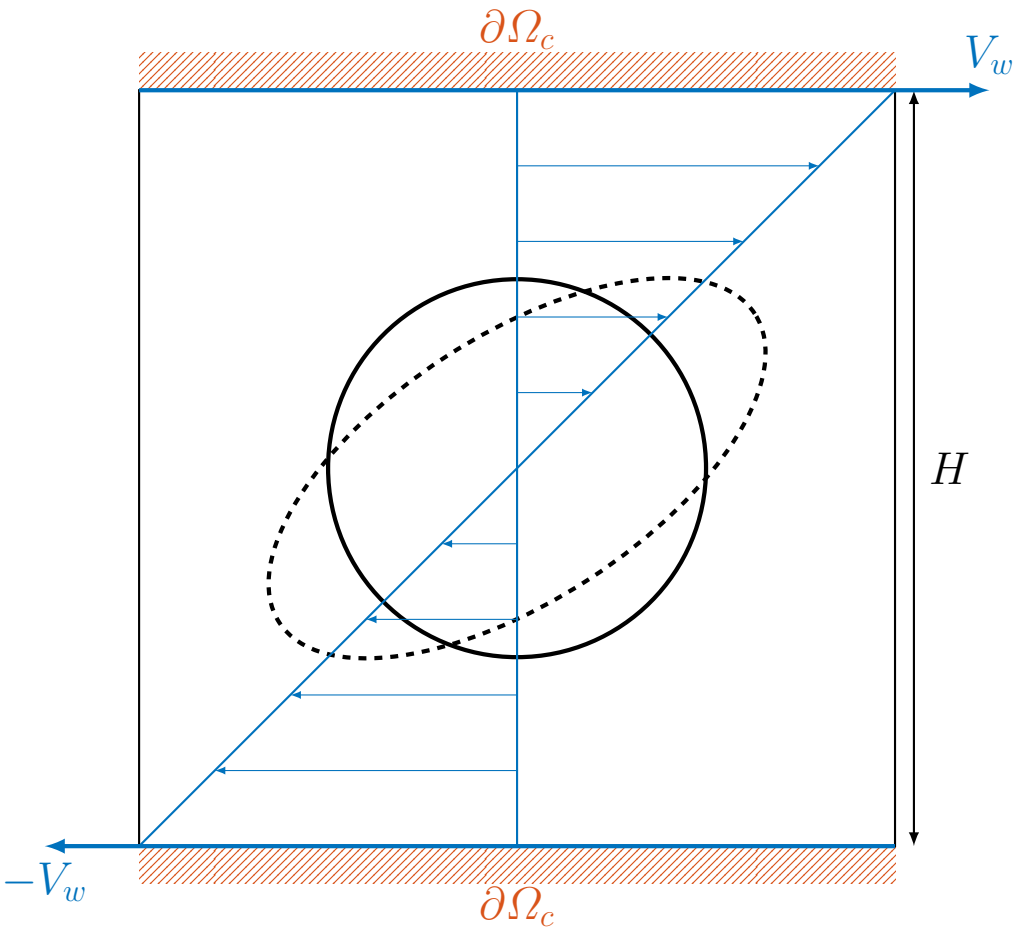

Figure 4.5: Setup of a circular material interface in a steady state Couette flow at the initial (—) and final time (- -).

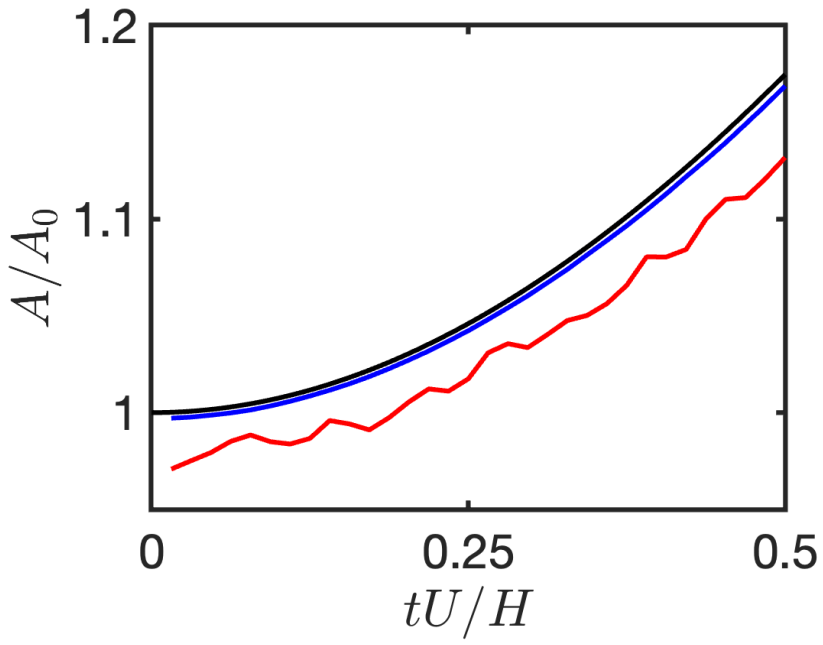

(a)

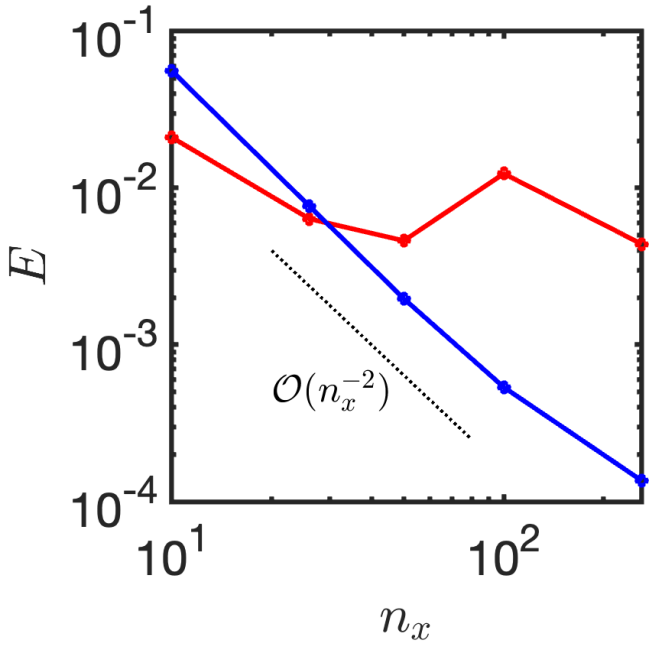

(b)

Figure 4.6: a) Surface area as a function of time for a 32^2 mesh and b) mesh convergence of error at the final time. Exact surface area (—) and surface area calculated from $A[\mathcal{P}]$ (—), and S (—).

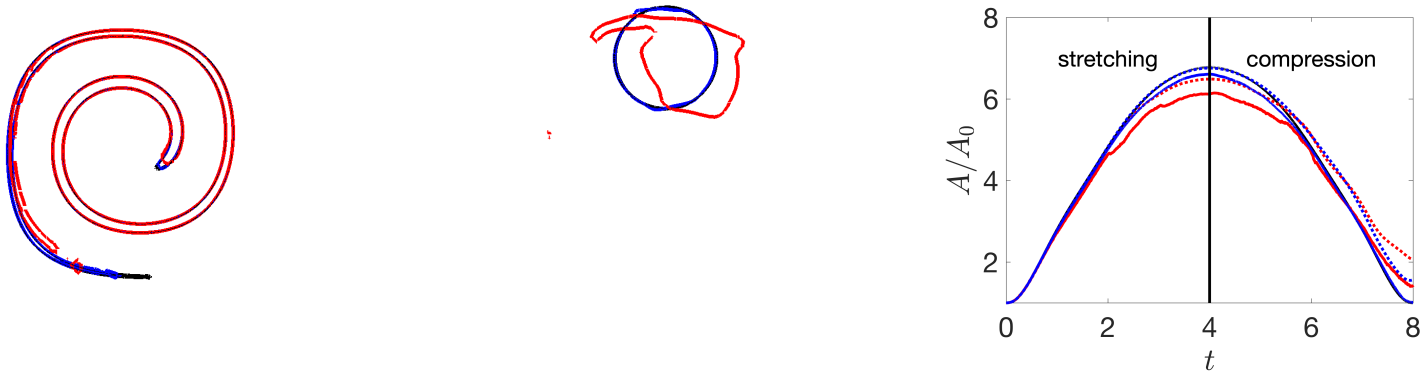

(a) (b) (c)

Figure 4.7: a) Interface at $t = 4$ and b) $t = 8$ for a mesh size 64^2 (—), 256^2 (—), and 512^2 (—). c) Normalized surface area for the corresponding meshes as a function of time measured from $\hat{S}$ (solid lines) and S (dashed lines).

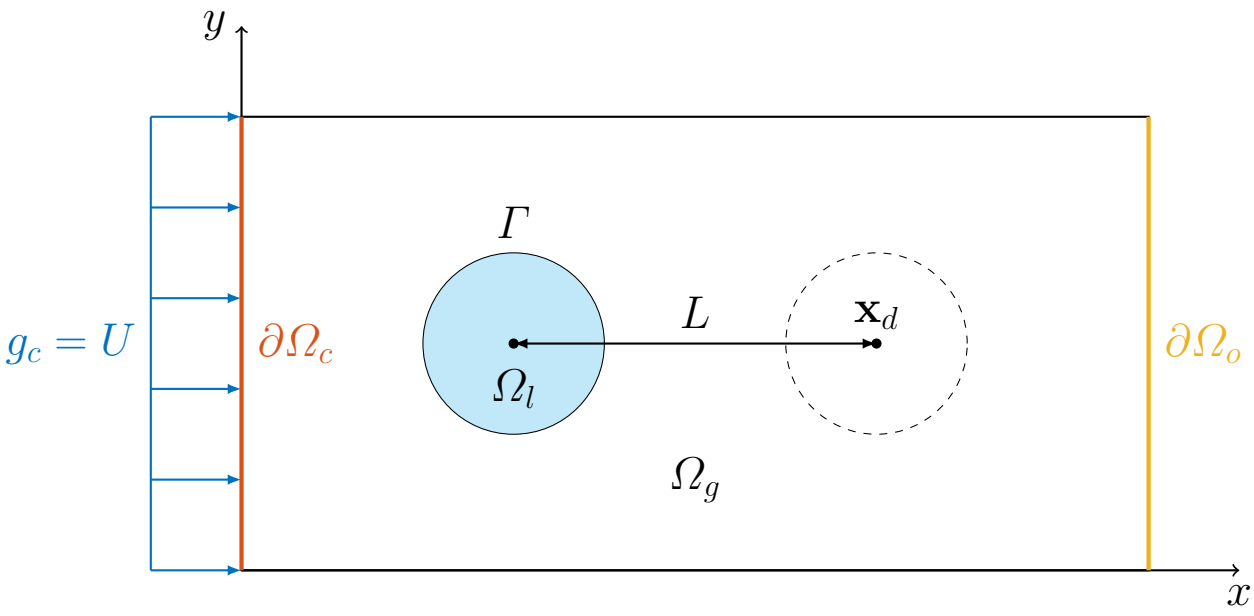

Figure 4.8: Setup of a drop in a uniform flow to match a desired position.

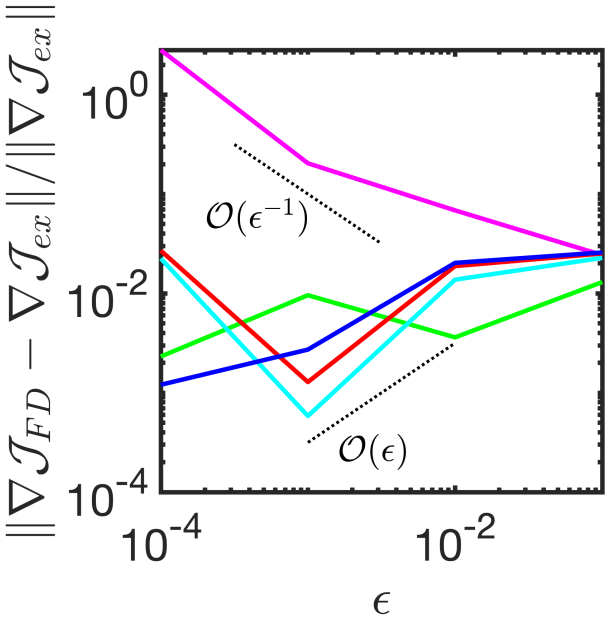

(a)

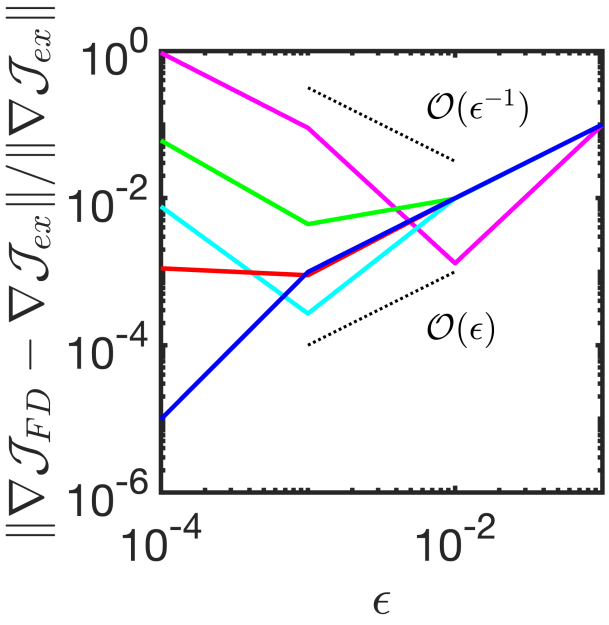

(b)

Figure 4.9: a) Setup of a drop in a uniform flow to match a desired position. Finite difference gradient errors using b) a surface based cost function and c) a volume based cost function for mesh sizes 16^2 (—), 32^2 (—), 64^2 (—), 128^2 (—), and 256^2 (—).

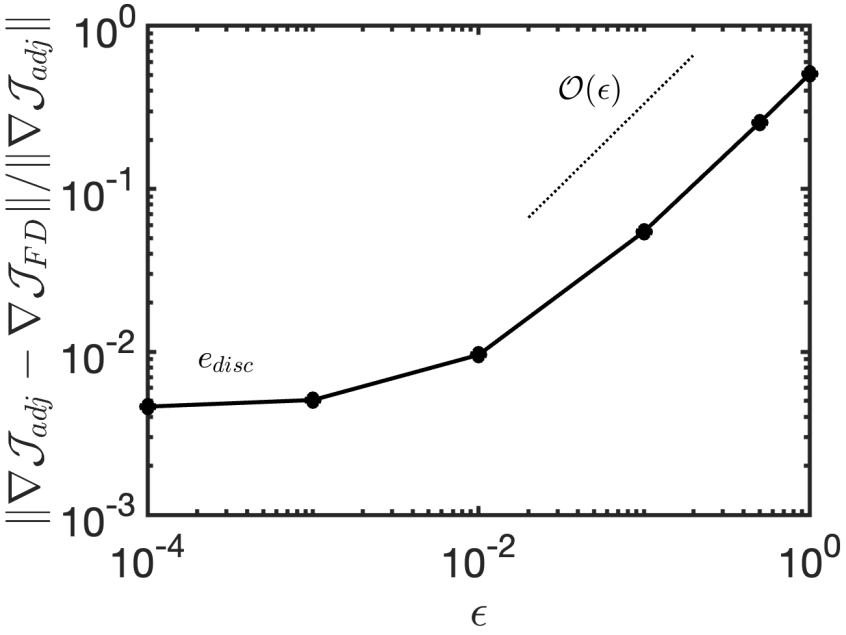

Figure 4.10: Verification of adjoint gradient for a lid-driven cavity velocity matching problem.

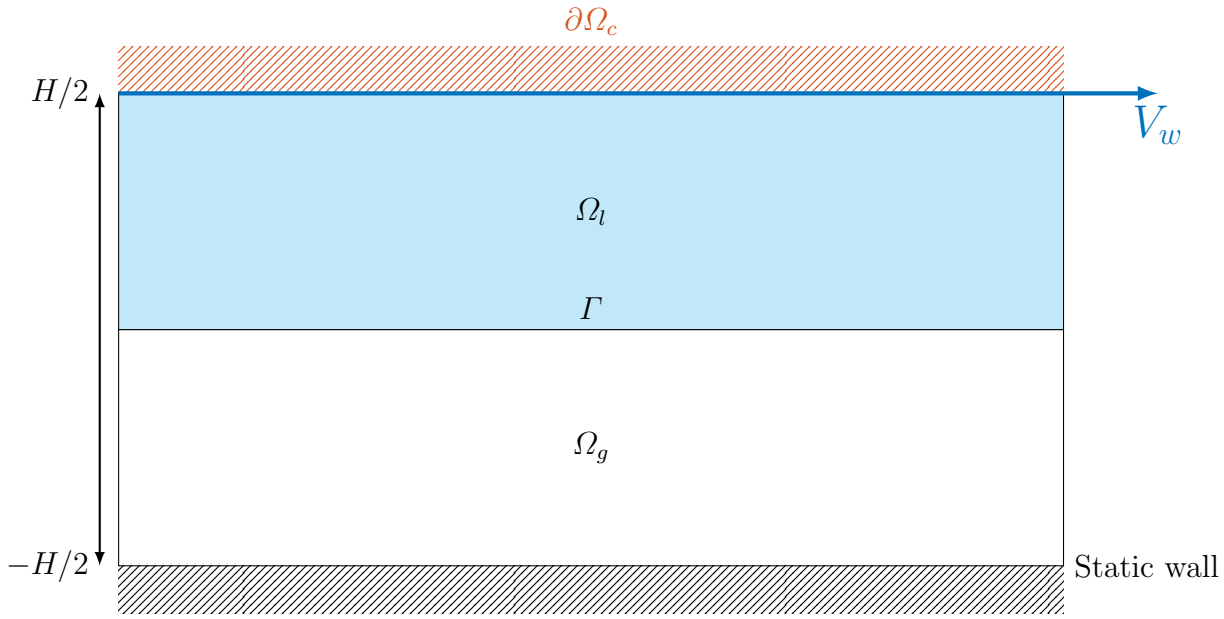

Figure 4.11: Setup of case with V_w as the control parameter.

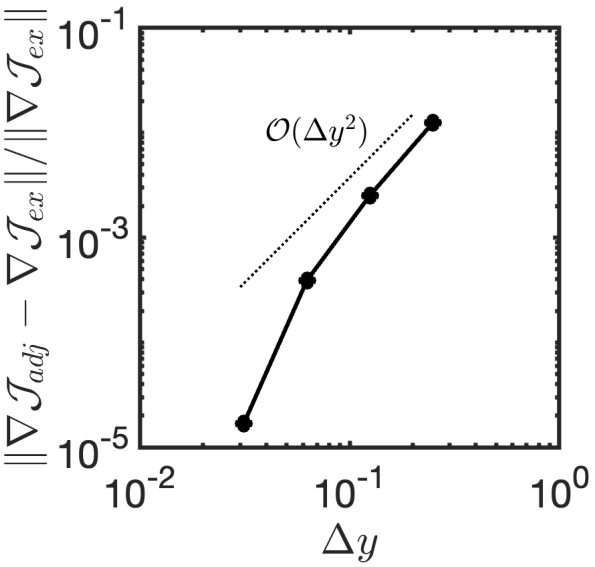

(a)

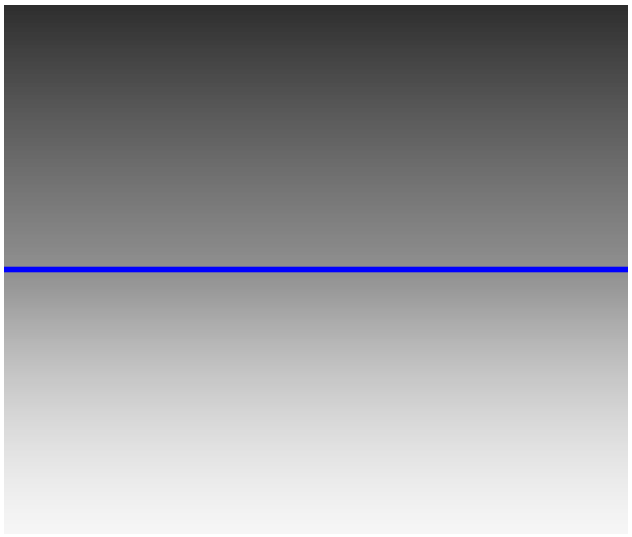

(b)

Figure 4.12: Verification of a two-phase Couette flow. a) mesh convergence of the adjoint gradient, and b) interface (—) and psuedo-color of u^* at $t/T = 1$.

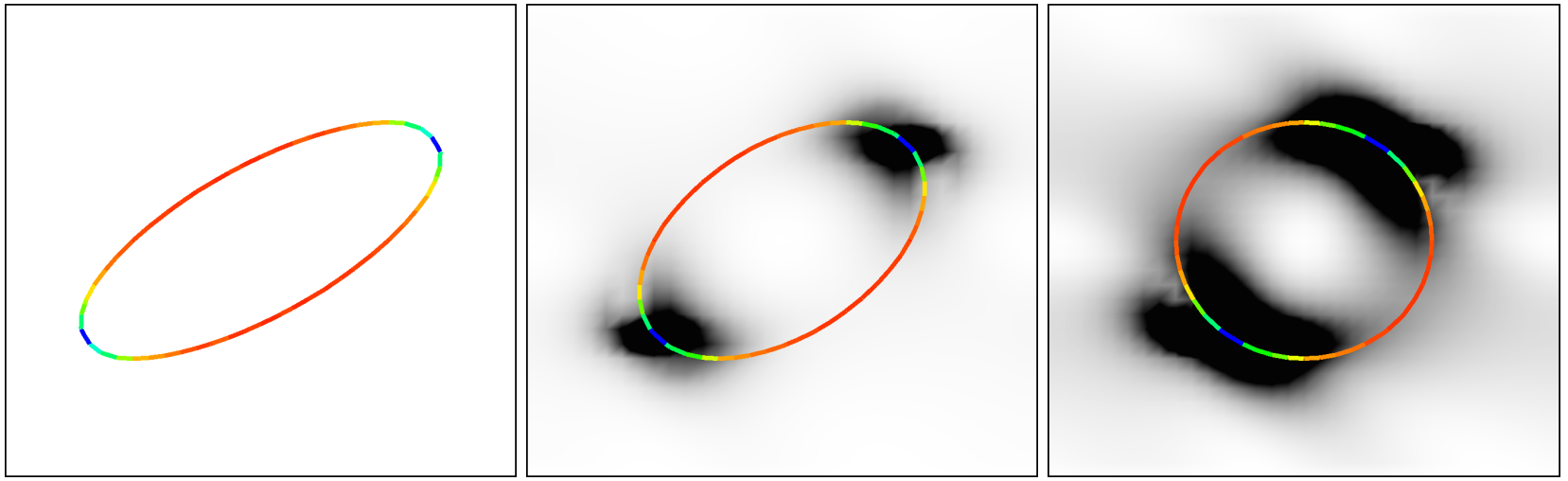

(a) (b) (c)

Figure 4.13: Adjoint simulation for surface area maximization problem of a drop in a steady-state Couette flow. ϕ^* plotted at the interface, $|\boldsymbol{u}^*|$ plotted as a pseudo-color shown at a) $t/T = 1$, b) $t/T = 0.5$ and $t/T = 0$.

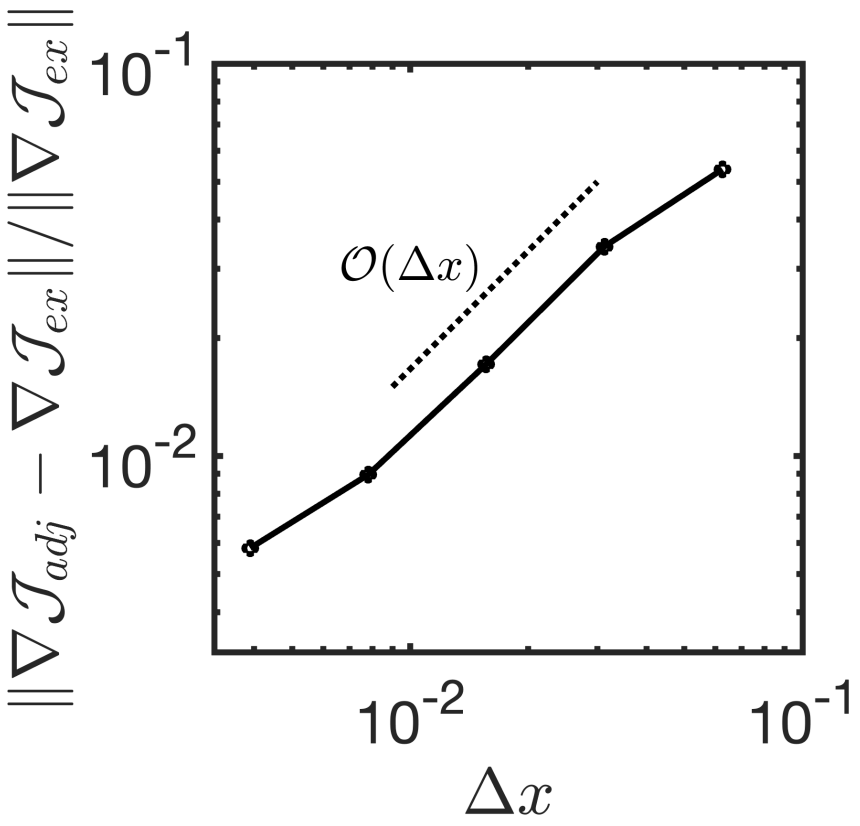

Figure 4.14: Gradient verification for surface area maximization problem of a drop in a steady-state Couette flow.

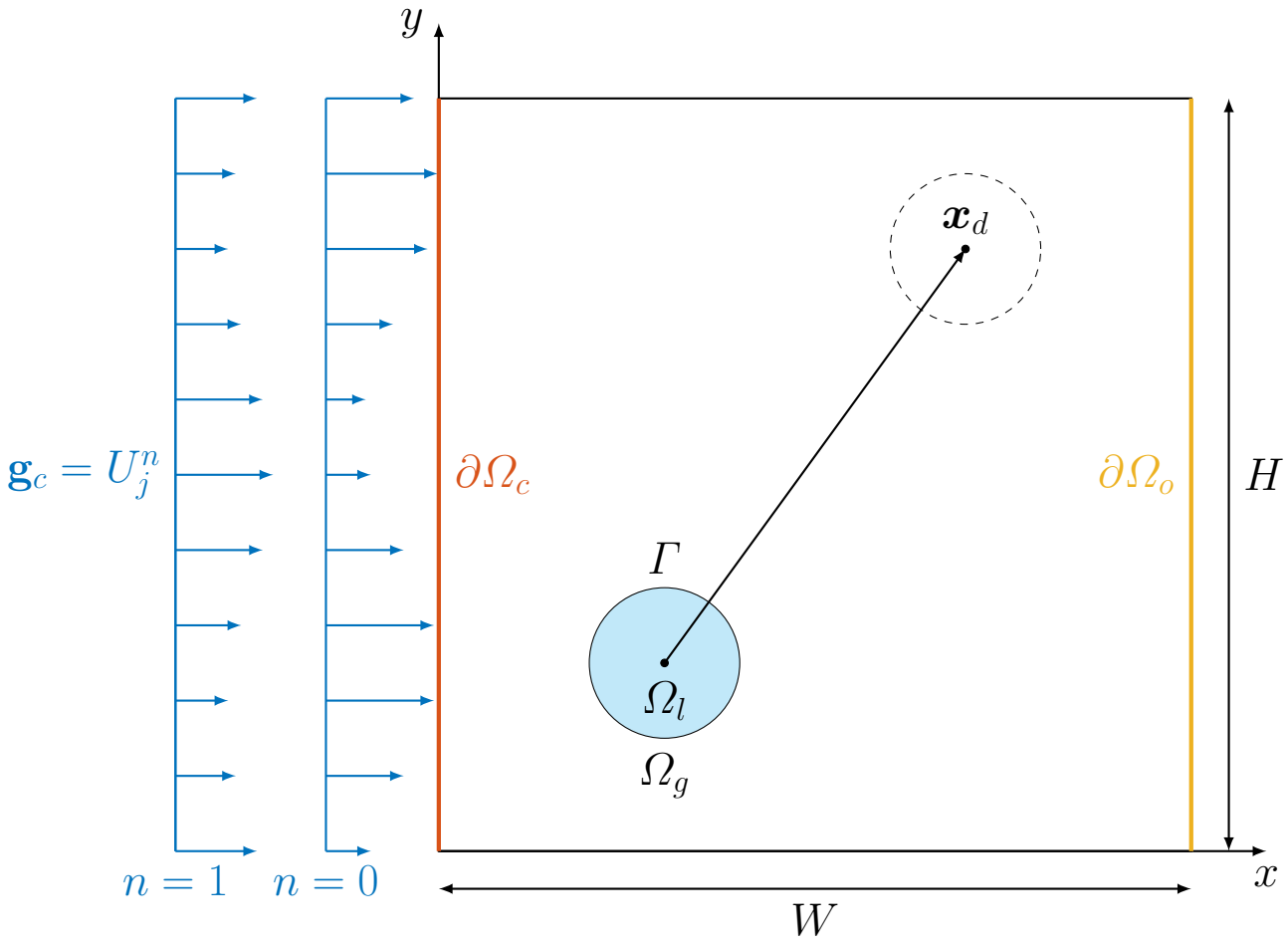

Figure 4.15: Setup of creating lift on a drop using variable spatial and temporal U_j^n control.

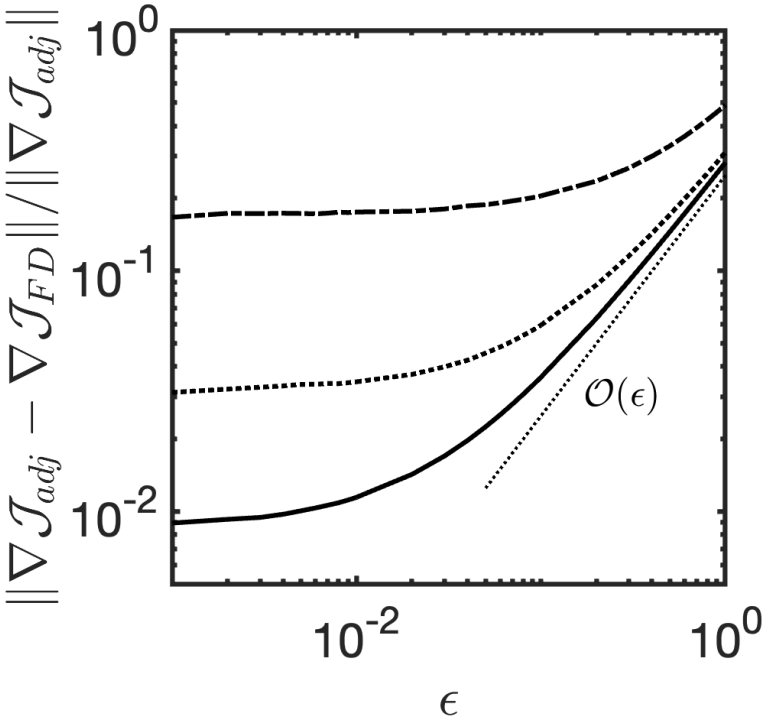

(a)

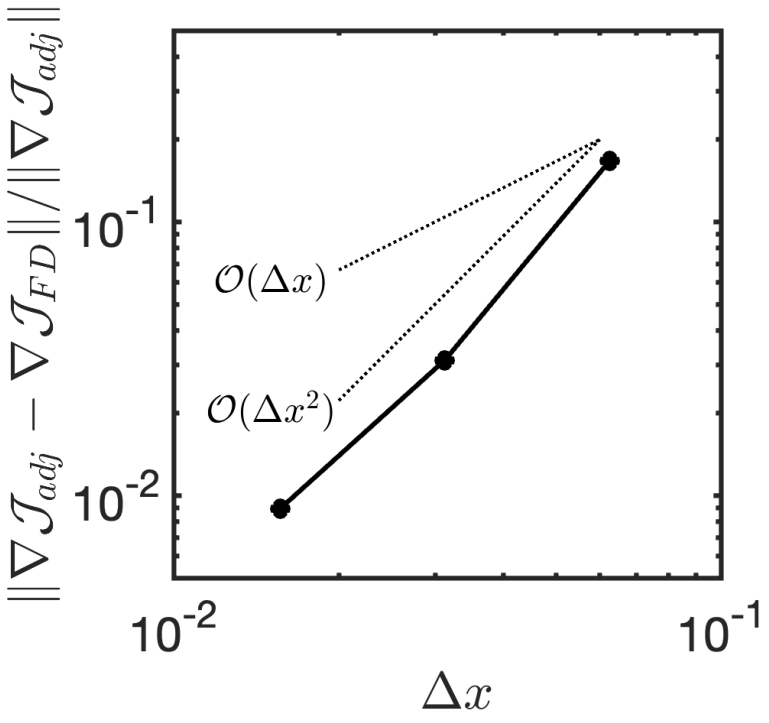

(b)

Figure 4.16: Verification case of 1D inflow control of a drop. a) Finite difference error for different mesh sizes $n = 8$ (-·-), 16 (····), 32 (—) where n is the number of cells across the drop diameter, b) mesh convergence of error at $\epsilon = 10^{-3}$.

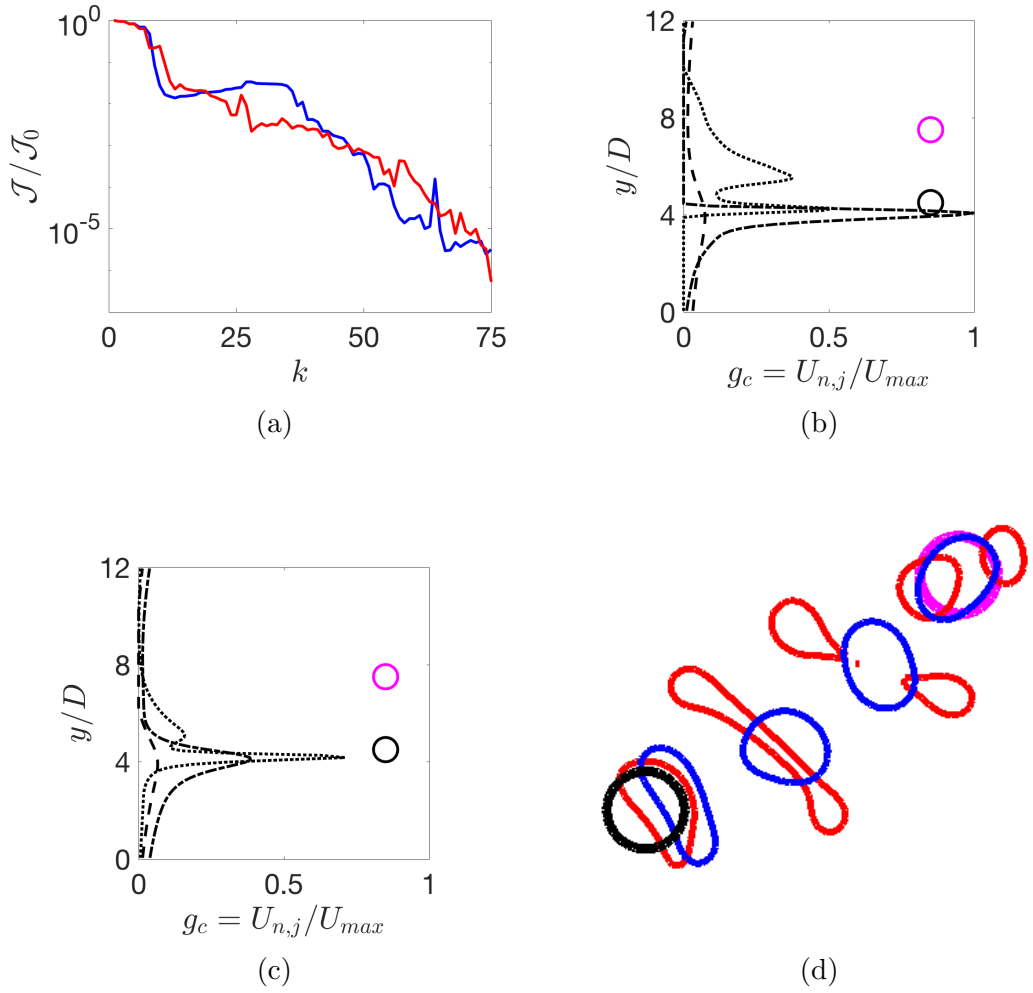

Figure 4.17: a) Cost function vs optimization iteration. Controls shown at $t/T = 0.1$ (····), $t/T = 0.45$ (-·-) and $t/T = 0.8$ (- -) for b) $\sigma = 1$ and c) $\sigma = 0.2$ surface tension case with vertical position of initial (—) and desired position (—) displayed. Optimal solution showing d) evolution of interface (in a zoomed window) at $t/T = 0.25, 0.5, 0.75, 1$ for $\sigma = 1$ (—) and $\sigma = 0.2$ (—) surface tension case.

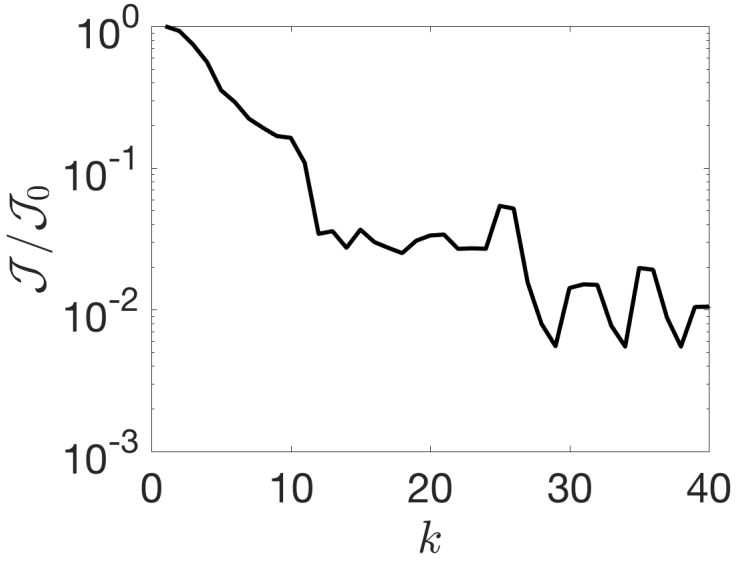

(a)

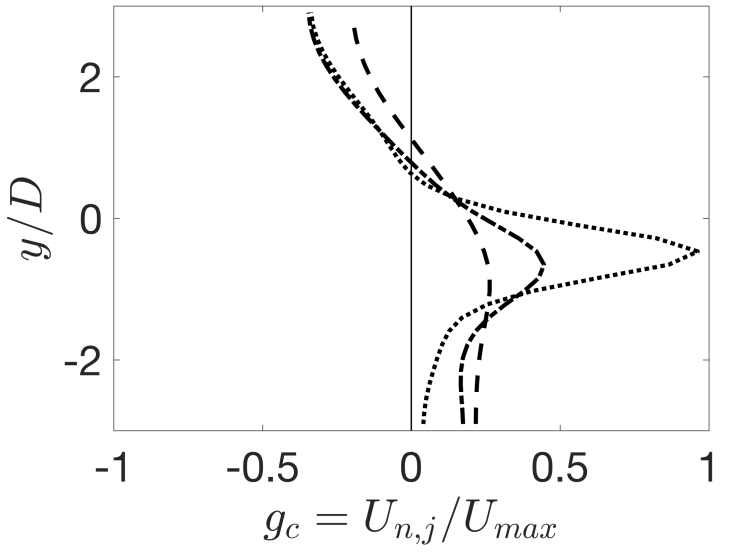

(b)

Figure 4.18: a) Cost function for optimization of drop levitation case and b) controls shown at $t/T = 0.25$ (⋯), $t/T = 0.5$ (-·-) and $t/T = 0.75$ (- -) and vertical line at 0 velocity for reference and signifies the uncontrolled velocity.

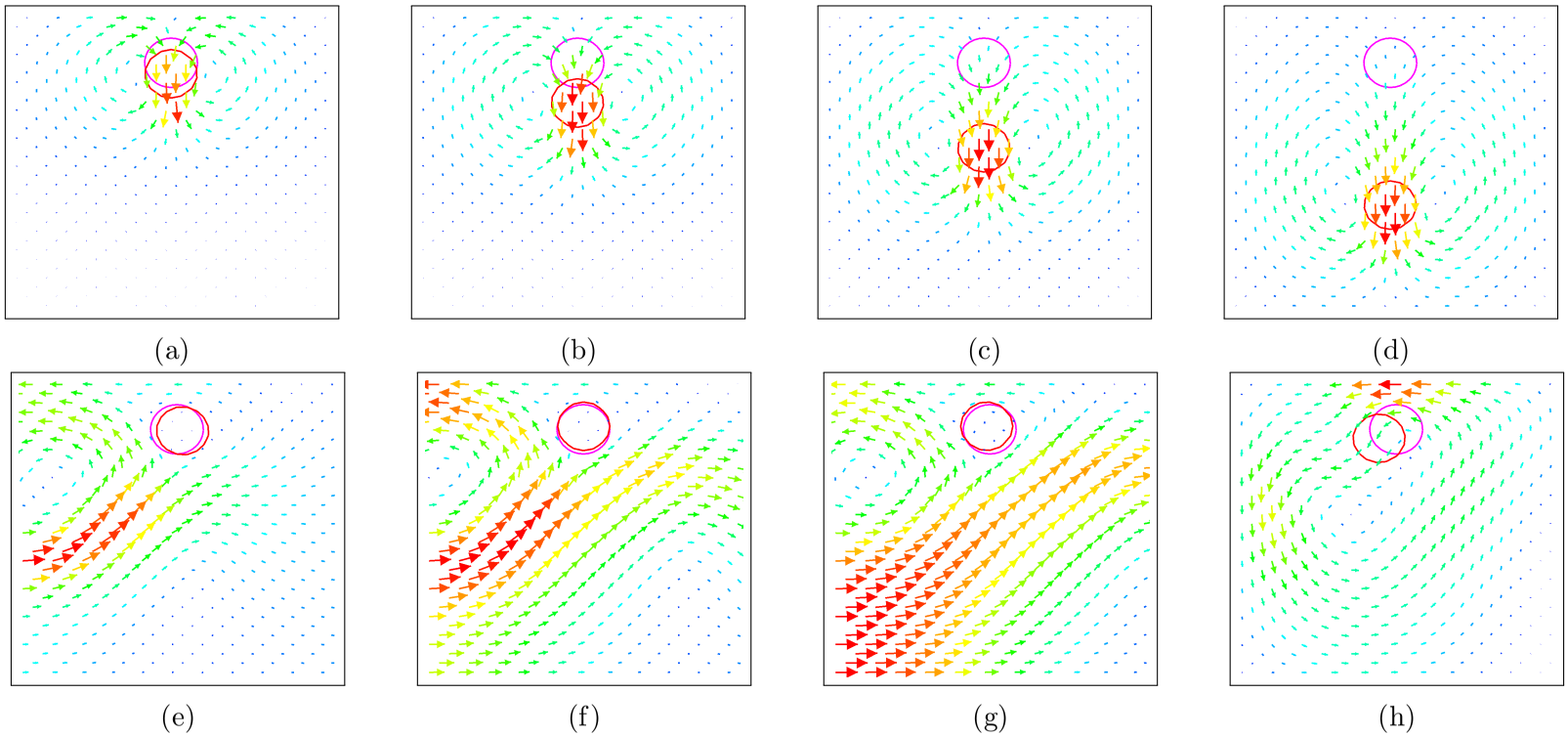

Figure 4.19: Demonstration of inflow control to levitate a drop. The drop's position (—) and the velocity vector plot at $t/T = 0.25, 0.5, 0.75, 1$ against its initial position (—). (a-d) is the uncontrolled case and (e-h) is the controlled case.

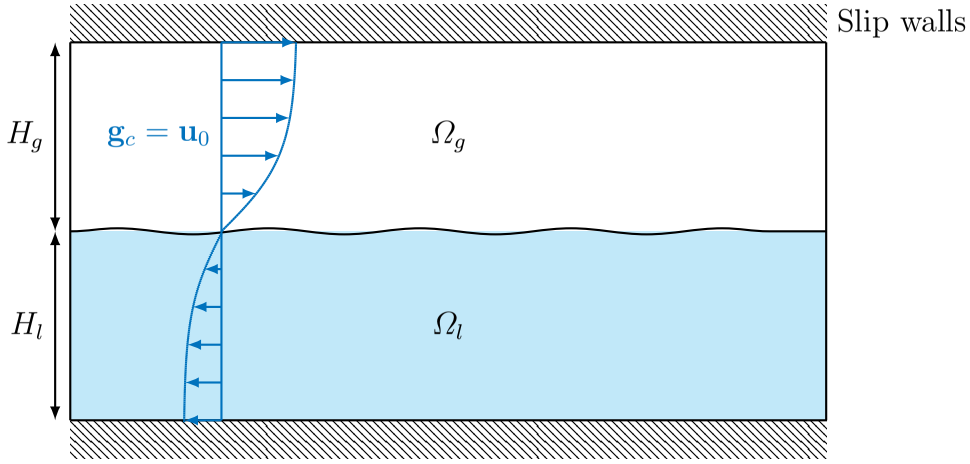

Figure 4.20: Setup of temporally evolving liquid-gas mixing layer.

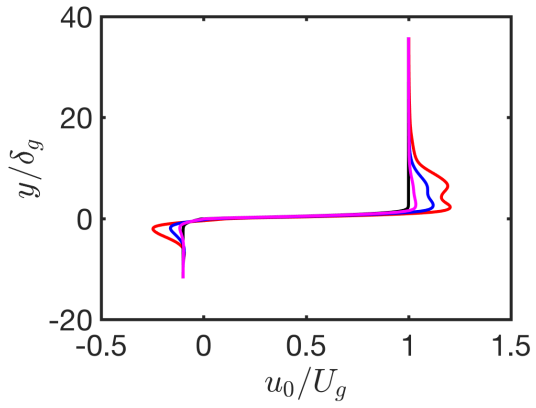

(a)

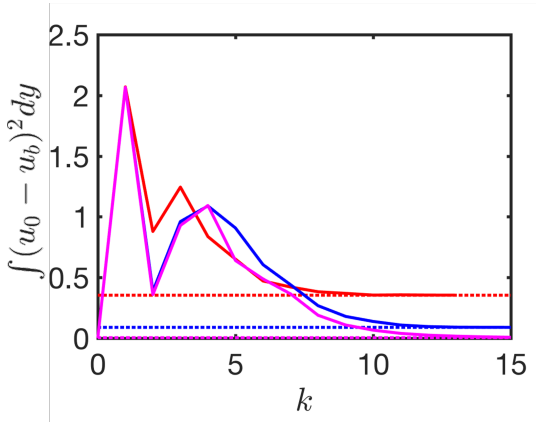

(b)

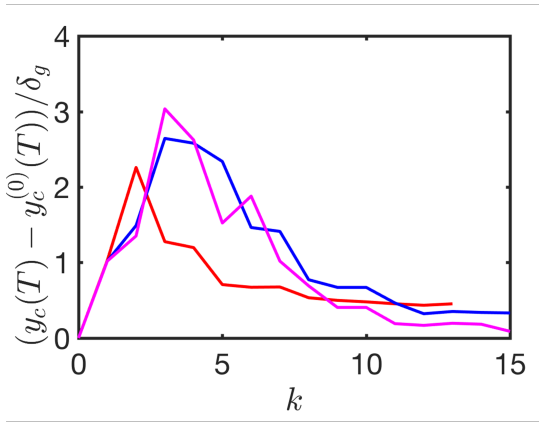

(c)

Figure 4.21: Temporally evolving mixing layer. a) Optimal initial velocity profile, b) variance of the velocity profile relative to the base profile and c) relative change of liquid barycenter for $\eta = 0.01$ (—), $\eta = 0.05$ (—), and $\eta = 0.1$ (—), horizontal dashed lines are the constraints imposed.

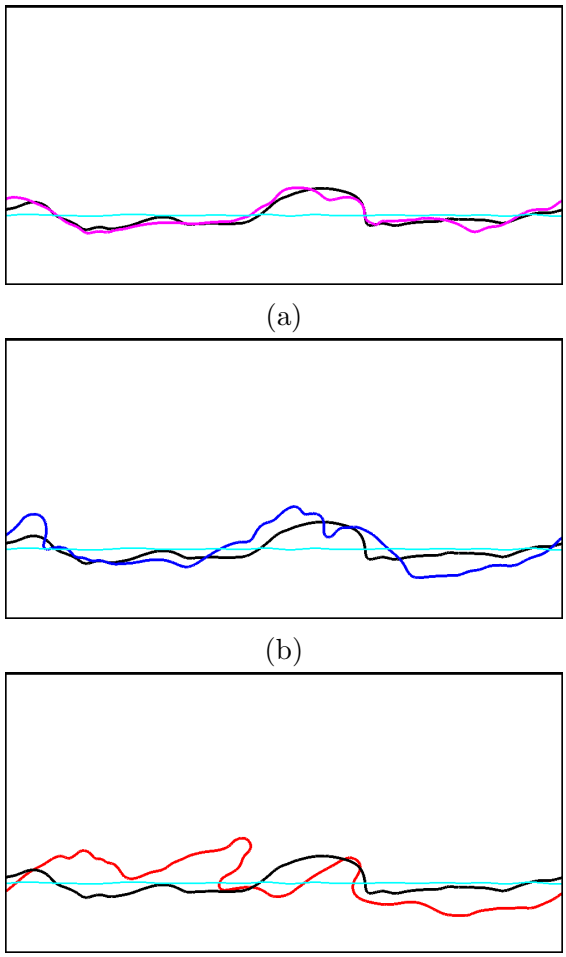

(a)

(b)

(c)

Figure 4.22: Temporally evolving mixing layer, interface at final time for a) $\eta = 0.01$ (—), b) $\eta = 0.05$ (—), and c) $\eta = 0.1$ (—) and the initial interface (—).

Table 4.1: Summary of cost functions and resultant source terms inside adjoint equation.

Case (at final time)	j_{Ω_T}	$\nabla_{\mathbf{u}} j_{\Omega_T}$	j_{Γ_T}	$\nabla_{\phi} j_{\Gamma_T}$
Velocity matching	$\frac{1}{2}\int_{\Omega} \|\boldsymbol{u}(T) - \boldsymbol{u}_d\|^2 \, \mathrm{d}V$	$\boldsymbol{u}(T) - \boldsymbol{u_d}$	–	–
Surface area maximization	–	–	$\int_{\Gamma_T} \mathrm{d}S$	κ
Centroid matching	$\frac{1}{2}\|\boldsymbol{x}_c(T) - \boldsymbol{x}_d\|^2$	$\frac{1}{\Omega_l}(\boldsymbol{x}_c(T) - \boldsymbol{x}_d) \cdot (\boldsymbol{x} - \boldsymbol{x}_c(T))\delta(\phi(T))$	–	–
Case (for all time)	j_{Ω}	$\nabla_{\mathbf{u}} j_{\Omega}$	j_{Γ}	$\nabla_{\phi} j_{\Gamma}$
Centroid matching	$\frac{1}{2}\|\boldsymbol{x}_c(t) - \boldsymbol{x}_d\|^2$	$\frac{1}{\Omega_l}(\boldsymbol{x}_c(t) - \boldsymbol{x}_d) \cdot (\boldsymbol{x} - \boldsymbol{x}_c(t))\delta(\phi(t))$	–	–

Table 4.2: Summary of control and adjoint gradients.

Case	$\boldsymbol{g}_c$	$\nabla_{\boldsymbol{g}_c}\mathcal{J}$	Notes
Wall velocity	V_w	$\int_0^T \int_{\partial\Omega_c} 2\mu \frac{\partial u^*}{\partial y} \,\mathrm{d}x \,\mathrm{d}t$	Lid-driven cavity / two-phase planar Couette
Wall velocity	V_w	$\int_0^T \int_{\partial\Omega_c} 2\mu \frac{\partial u^*}{\partial y} \,\mathrm{d}x \,\mathrm{d}t + \int_\Omega \rho \frac{2y}{H} u^*(0) \,\mathrm{d}V$	Material interface in steady-state Couette flow
Inflow velocity	U	$\int_0^T \int_0^{L_y} -p^* + 2\mu \frac{\partial u^*}{\partial x} \,\mathrm{d}y \,\mathrm{d}t$	Constant velocity field
Inflow velocity	U_j^n	$\left(-p^* + 2\frac{\partial u^*}{\partial x}\right)_j^n$	Space and time dependent velocity field
Initial velocity	u_0	$\int_0^{L_x} u^*(0) \,\mathrm{d}x$	Temporally evolving mixing layer

CHAPTER 5

SUMMARY AND OUTLOOK

5.1 Summary

In this dissertation, I have presented a multi-scale simulation strategy for spray atomization and an adjoint framework for liquid-gas flow control. This multi-scale simulation strategy was used to simulate spray atomization at air-water conditions in a complex geometry and extensively validated against experiments. The adjoint framework was used to control a wide range of non-trivial multiphase flow problems.

Chapter 2 validated the simulations of spray atomization against experiments. Experimental data was gathered from back-lit imaging and focused beam X-ray measurements. Good comparisons were shown in the distributions of liquid equivalent path length (EPL), liquid intact length, and flapping frequency. The gas velocity model was varied. Results showed that the gas vorticity thickness plays a leading role in the distribution of liquid downstream and suggested that turbulent fluctuations also play a key role. The contact line model was varied and shown to have a strong influence on the liquid distribution downstream. A sub-grid scale (SGS) contact line model was used to model the nozzle tip wettability and the effect of the static contact angle on spray metrics was quantified.

Chapter 3 presented a multi-scale simulation strategy that utilized multiple domains. The corresponding governing equations for each domain and the coupling between the domains was presented. This strategy required the use of multiple SGS models and the use of a thin structure break up model to explicitly model topology

change. The thin structure break up model was shown to result in good agreement of drop size distributions against experiments.

Chapter 4 detailed the mathematical formulation and numerical implementation of the two-phase adjoint Navier–Stokes equations. A surface quantity transport method was developed and implemented to solve for the adjoint level set equation arising from this formulation. This adjoint framework was verified by performing gradient checking exercises for model liquid-gas flow problems. It was also demonstrated by optimizing several test cases including optimizing the initial velocity profile to maximize growth of a temporally evolving liquid-gas mixing layer.

5.1.1 Outlook

In this dissertation, developments were made on spay atomization modeling and computational liquid-gas flow control. Yet, there is still potential to expand on these topics.

Simulations presented in this dissertation were performed at a low momentum flux ratio. Performing simulations at a higher momentum flux ratio would bring the simulations closer to industrial relevance. However, they would likely illuminate other modeling obstacles that would need to be addressed. This work has shown that the contact line plays a significant role on the liquid distribution. As such, other computational modeling strategies for it and a more detailed experimental investigation on how the contact line affects spray statistics downstream would be useful. The thin structure break up model used in this work requires a few input parameters. Experimental and numerical studies of the break up of small scale

liquid structures would be invaluable in guiding the choice of these parameters.

Computational control of liquid-gas flows under a sharp interface model is still in its infant stages. Very few studies have attempted liquid-gas flow control and there is no general consensus on what method is most effective. As such, using other common control techniques such as pattern search methods, evolutionary methods, and machine learning to control liquid-gas flows to see how they compare against adjoint methods would be extremely useful. Within the adjoint framework presented here, developing the methods and verification to address the simplifications made, would give a fuller understanding on the method's limitations. The control of a temporally evolving liquid-gas mixing layer presented in this work is demonstrated in an academic setting. Translating this to a more applied spray atomization case, e.g. using the optimized velocity profile and adding a bulk velocity to model the gas inflow, would be extremely interesting.

APPENDIX A

GENERAL ADJOINT DERIVATION

A.1 Shape Calculus

We give here a brief introduction to shape calculus with the goal of defining the main results necessary to discuss the linearization and adjoint of the two-phase Navier–Stokes system defined in Section 4.3. For an in depth discussion of these concepts see [23], for the standard case, and [73] for the case of moving geometries. Furthermore, for a similar application involving the level set formulation see [10].

For the derivation of the adjoint equations, we are mostly interested in defining perturbations of *shape functionals* of the form

$$\mathcal{J} : \mathcal{D} \to \mathbb{R},$$

where $\mathcal{D}$ is a hold-all set that contains all the possible interface configurations in the domain Ω. For this work, we assume that the interface does not intersect $\partial\Omega$, so that all interface surfaces are closed curves in Ω. For a given configuration $\Gamma \in \mathcal{D}$ of the interface, we define its perturbation by the *speed method* (see [23]) as

$$\Gamma_\epsilon \triangleq \{\boldsymbol{x} + \epsilon\tilde{\boldsymbol{V}} \mid \boldsymbol{x} \in \Gamma\},$$

where $\epsilon \in \mathbb{R}_+$ small and $\tilde{\boldsymbol{V}}$ is a sufficiently smooth perturbation velocity field. In the context of level set methods, $\mathcal{D}$ becomes the space of all twice differentiable level set functions and the perturbation velocity is given by

$$\tilde{\boldsymbol{V}} \triangleq -\frac{\tilde{\phi}}{\|\nabla\phi\|}\frac{\nabla\phi}{\|\nabla\phi\|},$$

where ϕ is the level set function and $\tilde{\phi}$ is a perturbation. Then, [23] defines the following shape functional shape derivatives

$$\begin{aligned}
\mathcal{J}_1 \triangleq \int_\Omega f \,\mathrm{d}V \implies \frac{\mathrm{d}\mathcal{J}_1}{\mathrm{d}\phi}[\tilde{\phi}] &= -\int_\Gamma [\![f]\!] \frac{\tilde{\phi}}{\|\nabla\phi\|} \,\mathrm{d}S, \\
\mathcal{J}_2 \triangleq \int_\Gamma f \,\mathrm{d}S \implies \frac{\mathrm{d}\mathcal{J}_2}{\mathrm{d}\phi}[\tilde{\phi}] &= -\int_\Gamma (\boldsymbol{n}\cdot\nabla f + \kappa f) \frac{\tilde{\phi}}{\|\nabla\phi\|} \,\mathrm{d}S, \\
\mathcal{J}_3 \triangleq \int_\Gamma g \,\mathrm{d}S \implies \frac{\mathrm{d}\mathcal{J}_3}{\mathrm{d}\phi}[\tilde{\phi}] &= -\int_\Gamma \kappa g \frac{\tilde{\phi}}{\|\nabla\phi\|} \,\mathrm{d}S,
\end{aligned}$$

where we have assumed that $\tilde{\phi}|_{\partial\Omega} \equiv 0$, as we do not perturb the domain boundary, only the interface Γ. In the above, $f : \Omega \to \mathbb{R}$ is a domain function and $g : \Gamma \to \mathbb{R}$ is a surface function that does not depend on the geometry. We are also interested in the shape derivatives of standard geometric quantities, such as curvature and the normal vector field. From [106], we have that

$$\begin{aligned}
\frac{\partial \boldsymbol{n}}{\partial\phi}[\tilde{\phi}] &= \nabla_\Gamma \left(\frac{\tilde{\phi}}{\|\nabla\phi\|} \right), \\
\frac{\partial \kappa}{\partial\phi}[\tilde{\phi}] &= \Delta_\Gamma \left(\frac{\tilde{\phi}}{\|\nabla\phi\|} \right),
\end{aligned}$$

where ∇_Γ and Δ_Γ are the tangential gradient and the Laplace-Beltrami operator. They can be expressed in terms of the ambient derivatives as

$$\begin{aligned}
\nabla_\Gamma f &= \frac{\mathrm{d}f}{\mathrm{d}s}\boldsymbol{t} = \nabla f - (\boldsymbol{n}\cdot\nabla f)\boldsymbol{n}, \\
\Delta_\Gamma f &= \frac{\mathrm{d}^2 f}{\mathrm{d}s^2} = \Delta f - \kappa(\boldsymbol{n}\cdot\nabla f)\boldsymbol{n} - (\boldsymbol{n}\cdot\nabla\nabla f)\cdot\boldsymbol{n},
\end{aligned}$$

where s denotes the arclength, in the case of two-dimensional domains. In the case of moving geometries presented in [73], all the above formulae remain the same, but the velocity field $\tilde{\boldsymbol{V}}$ is understood as a transverse perturbation that satisfies a given evolution equation. In the context of level set methods, this is can be obtained by linearizing the interface evolution equation (eq. (4.10)). As such, $\tilde{\phi}$ satisfies a linearized advection equation of a form similar to eq. (4.10). The subtlety here lies in the boundary conditions; namely at the inflow $\tilde{\phi}|_{\partial\Omega_i} \equiv 0$,

and at the outflow $\tilde{\phi}$ is left unspecified (outgoing characteristics of the advection equation do not require boundary conditions).

A.2 Formal Derivation of the Optimality Conditions

Using the results presented in Appendix A.1, we are in a position to linearize the Navier–Stokes equations eq. (4.7) with the corresponding jump conditions eq. (4.8). For this, we require an explicit formulation of the Lagrangian eq. (4.2) that contains all the constraints of the problem. We opt to express the two-phase Navier–Stokes system in a variational formulation of the two phases. Note that this is in contrast to the equivalent one-fluid-type formulation given in eq. (4.7). Then, the Lagrangian can be written as

$$
\begin{aligned}
\mathcal{L} \triangleq \mathcal{J} - & \underbrace{\int_0^T \int_{\Omega_{l,g}(t)} \phi^*(\phi_t + \boldsymbol{u}_{l,g} \cdot \nabla\phi)\,\mathrm{d}V\,\mathrm{d}t}_{T_1} \\
& - \underbrace{\int_0^T \int_{\Omega_{l,g}(t)} \boldsymbol{u}^*_{l,g} \cdot (\rho_{l,g}(\boldsymbol{u}_{l,g})_t + \rho_{l,g}\boldsymbol{u}_{l,g} \cdot \nabla\boldsymbol{u}_{l,g} - \boldsymbol{f}_{l,g})\,\mathrm{d}V\,\mathrm{d}t}_{T_2} \\
& - \underbrace{\int_0^T \int_{\Omega_{l,g}(t)} \nabla\boldsymbol{u}^*_{l,g} : T_{l,g}\,\mathrm{d}V\,\mathrm{d}t}_{T_3} + \underbrace{\int_0^T \int_{\Omega_{l,g}(t)} p^*_{l,g}(\nabla \cdot \boldsymbol{u}_{l,g})\,\mathrm{d}V\,\mathrm{d}t}_{T_4} \\
& + \underbrace{\int_0^T \int_{\Gamma(t)} \langle \boldsymbol{n} \cdot T^* \rangle \cdot [\![\boldsymbol{u}]\!]\,\mathrm{d}S\,\mathrm{d}t + \int_0^T \int_{\Gamma(t)} \langle \boldsymbol{n} \cdot T \rangle \cdot [\![\boldsymbol{u}^*]\!]\,\mathrm{d}S\,\mathrm{d}t}_{T_5} + \underbrace{\int_0^T \int_{\Gamma(t)} \sigma\kappa\langle \boldsymbol{u}^* \rangle \cdot \boldsymbol{n}\,\mathrm{d}S\,\mathrm{d}t}_{T_6} \\
& - \underbrace{\int_0^T \int_{\partial\Omega_c} \boldsymbol{g}^*_c \cdot (\boldsymbol{u}_{l,g} - \boldsymbol{g}_c)\,\mathrm{d}S\,\mathrm{d}t}_{T_7} \\
& - \underbrace{\int_\Omega \boldsymbol{u}^*(0) \cdot (\boldsymbol{u}(0) - \boldsymbol{u}_0)\,\mathrm{d}V - \int_0^T \int_{\partial\Omega_c(t)} \phi^*(\phi - \phi_i)\,\mathrm{d}S\,\mathrm{d}t - \int_\Omega \phi^*(0)(\phi(0) - \phi_0)\,\mathrm{d}V}_{T_8},
\end{aligned}
\tag{A.1}
$$

where summation over the phases $\{l, g\}$ is implied and T is the Cauchy stress tensor. Here $\langle\cdot\rangle$ is an interfacial average defined as

$$\langle f\rangle \triangleq \frac{1}{2}(f_l + f_g)$$

and arises in the equations from employing the identity

$$[\![fg]\!] = \langle f\rangle[\![g]\!] + [\![f]\!]\langle g\rangle.$$

A.2.1 Adjoint Navier–Stokes Equations

The adjoint Navier–Stokes equations eq. (4.11) are obtained by linearizing the Lagrangian with respect to the flow variables $\boldsymbol{w} = (p, \boldsymbol{u})$. We then require that the result is a stationary point of the Lagrangian to derive the adjoint equations, i.e.

$$\frac{\partial \mathcal{L}}{\partial \boldsymbol{w}}[\tilde{\boldsymbol{w}}] = 0.$$

This derivation follows exactly the single-phase results that are present in the literature, e.g. [11]. The main difference comes from the fact that we require the application of a modified Reynolds Transport Theorem on the convective terms. As such, we will focus here on the terms present in T_2 from eq. (A.1), which linearize as

$$\frac{\partial T_2}{\partial \boldsymbol{w}}[\tilde{\boldsymbol{w}}] = \int_0^T \int_{\Omega_{l,g}(t)} \boldsymbol{u}^*_{l,g} \cdot (\rho_{l,g}(\tilde{\boldsymbol{u}}_{l,g})_t + \rho_{l,g}\tilde{\boldsymbol{u}}_{l,g} \cdot \nabla \boldsymbol{u}_{l,g} + \rho_{l,g}\boldsymbol{u}_{l,g} \cdot \nabla \tilde{\boldsymbol{u}}_{l,g})\, \mathrm{d}V\, \mathrm{d}t,$$

where the volume forces vanish, as they do not depend on the state variables. Next, we must reduce the right-hand side to the form $\langle \mathcal{N}^*(\boldsymbol{w}^*), \tilde{\boldsymbol{w}}\rangle$, for some operator $\mathcal{N}^*$, which is performed by integration by parts. We first apply the Reynolds Transport Theorem [31] in both phases to obtain

$$\int_0^T \int_{\Omega_{l,g}} \rho_{l,g} \boldsymbol{u}_{l,g}^* \cdot (\tilde{\boldsymbol{u}}_{l,g})_t \,\mathrm{d}V \,\mathrm{d}t = \left[\int_{\Omega_{l,g}} \rho_{l,g} \boldsymbol{u}_{l,g}^* \cdot \tilde{\boldsymbol{u}}_{l,g} \,\mathrm{d}V \right]_{t=0}^{t=T} - \int_0^T \int_{\Omega_{l,g}} (\rho_{l,g} \boldsymbol{u}_{l,g}^*)_t \cdot \tilde{\boldsymbol{u}}_{l,g} \,\mathrm{d}V \,\mathrm{d}t - \int_0^T \int_{\Gamma(t)} [\![\rho \boldsymbol{u}^* \cdot \tilde{\boldsymbol{u}}]\!] (\boldsymbol{u} \cdot \boldsymbol{n}) \,\mathrm{d}V \,\mathrm{d}t,$$

where all terms on $\partial\Omega$ vanish, as that boundary is static. Then, we can apply the Divergence Theorem on the last term to remove the derivative from the perturbation and obtain

$$\begin{aligned} \int_0^T \int_{\Omega_{l,g}} \boldsymbol{u}_{l,g}^* (\rho_{l,g} \boldsymbol{u}_{l,g} \cdot \nabla \tilde{\boldsymbol{u}}_{l,g}) \,\mathrm{d}V \,\mathrm{d}t = & - \int_0^T \int_{\Omega_{l,g}} \nabla \cdot (\rho_{l,g} \boldsymbol{u}_{l,g} \otimes \boldsymbol{u}_{l,g}^*) \cdot \tilde{\boldsymbol{u}}_{l,g} \,\mathrm{d}V \,\mathrm{d}t \\ & + \int_0^T \int_{\Gamma(t)} [\![\rho \boldsymbol{u}^* \cdot \tilde{\boldsymbol{u}}]\!] (\boldsymbol{u} \cdot \boldsymbol{n}) \,\mathrm{d}S \,\mathrm{d}t \\ & + \int_0^T \int_{\partial\Omega_o} \rho_g (\boldsymbol{u}_g^* \cdot \tilde{\boldsymbol{u}}_g) (\boldsymbol{u}_g \cdot \boldsymbol{n}) \,\mathrm{d}S \,\mathrm{d}t \\ & + \int_0^T \int_{\partial\Omega_c} \rho_g (\boldsymbol{u}_g^* \cdot \tilde{\boldsymbol{u}}_g) (\boldsymbol{u}_g \cdot \boldsymbol{n}) \,\mathrm{d}S \,\mathrm{d}t, \end{aligned}$$

where we have assumed that only the gas phase intersects $\partial\Omega$. We can see here that the interfacial jumps from the two terms in T_2 cancel out, as they have opposite signs. Then, on $\partial\Omega_c$ we take $\boldsymbol{u}_g^* \equiv 0$. The remaining term

$$\int_0^T \int_{\partial\Omega_o} (\rho_g \boldsymbol{u}_g^* \cdot \tilde{\boldsymbol{u}}_g) (\boldsymbol{u}_g \cdot \boldsymbol{n}) \,\mathrm{d}S \,\mathrm{d}t$$

on the outflow boundary $\partial\Omega_o$ gives rise to the adjoint traction boundary condition from eq. (4.11). This gives the conservative form of the adjoint Navier–Stokes equations. To obtain the convective form presented in eq. (4.11), we can make use of the continuity and adjoint continuity equations. For a more detailed description of the steps required by the remaining terms, see the equivalent derivation for Stokes flow from [29].

A.2.2 Adjoint Level Set Equation

In [29], the authors have derived an adjoint evolution equation corresponding to the Lagrangian evolution of the interface. The same steps can be applied here to derive an adjoint to the level set equation (eq. (4.10)), by making use of the formulae from Appendix A.1. A few additional observations are in order. First, we have that the shape derivative of T_7 and T_8 vanish, i.e.

$$\frac{\partial T_7}{\partial \phi}[\tilde{\phi}] = \frac{\partial T_8}{\partial \phi}[\tilde{\phi}] = 0,$$

since either the constraints are satisfied or we can use that the state and adjoint velocity fields are both continuous across the interface. Then, the terms corresponding to T_3, T_4, T_5 and T_6 correspond exactly to the two-phase Stokes system studied in [29]. We are left with applying the shape functional derivatives to T_1 and T_2 alone. For the first, we have that

$$\frac{\partial T_1}{\partial \phi}[\tilde{\boldsymbol{\phi}}] = \int_0^T \int_{\Omega_{l,g}} \phi^* (\tilde{\phi}_t + \boldsymbol{u}_{l,g} \cdot \nabla \tilde{\phi}) \, \mathrm{d}V \, \mathrm{d}t,$$

where all the boundary vanishes due the PDE eq. (4.10) being satisfied up to the interface and all the interfacial terms vanish because all the variables are continuous across the interface. Then, we can again apply the Reynolds Transport Theorem and the Divergence Theorem to obtain

$$\begin{aligned}\frac{\partial T_1}{\partial \phi}[\tilde{\boldsymbol{\phi}}] = & -\int_0^T \int_{\Omega_{l,g}} (\phi_t^* + \nabla \cdot (\phi^* \boldsymbol{u}_{l,g})) \tilde{\phi} \, \mathrm{d}V \, \mathrm{d}t + \left[\int_{\Omega_{l,g}} \phi^* \tilde{\phi} \, \mathrm{d}V \right]_{t=0}^{t=T} \\ & + \int_0^T \int_{\partial \Omega_o} \phi^* \tilde{\phi} (\boldsymbol{u} \cdot \boldsymbol{n}) \, \mathrm{d}S \, \mathrm{d}t,\end{aligned}$$

where the outflow term does not vanish directly. It can be made to vanish by choosing $\phi^*|_{\partial \Omega_o} \equiv 0$. This is a standard result for advection equations (see [14]): the state variable ϕ has boundary conditions defined at the inflow $\partial \Omega_i$ and the adjoint variable ϕ^* has boundary conditions defined at the outflow $\partial \Omega_o$.

Finally, we have that

$$\frac{\partial T_2}{\partial \phi}[\tilde{\phi}] = \int_0^T \int_{\Gamma(t)} [\![\boldsymbol{u}^* \cdot (\rho \boldsymbol{u}_t + \rho \boldsymbol{u} \cdot \nabla \boldsymbol{u} - \boldsymbol{f})]\!] \frac{\tilde{\phi}}{\|\nabla \phi\|} \, \mathrm{d}V \, \mathrm{d}t,$$

where the boundary terms vanish, as before. From the Navier–Stokes equations, we can see that the jump above contains all the terms of the momentum equations except the stress. Therefore, it can also be written as

$$\frac{\partial T_2}{\partial \phi}[\tilde{\phi}] = \int_0^T \int_{\Gamma(t)} \boldsymbol{u}^* \cdot [\![\nabla \cdot T]\!] \frac{\tilde{\phi}}{\|\nabla \phi\|} \, \mathrm{d}V \, \mathrm{d}t.$$

Putting these results together with those of [29], we obtain the adjoint two-phase Navier–Stokes equations eq. (4.11) and the adjoint level set equation (eq. (4.13)). In its full generality, the source term in the adjoint level set equation (eq. (4.13)) reads

$$\begin{aligned} f_\Gamma^* = \sigma & \underbrace{(\Delta_\Sigma (\boldsymbol{u}^* \cdot \boldsymbol{n}) + |\nabla_\Sigma \boldsymbol{n}| \boldsymbol{u}^* \cdot \boldsymbol{n} - \nabla_\Sigma (\kappa \boldsymbol{u}^*) - \kappa (\boldsymbol{n} \cdot \nabla \boldsymbol{u}^*) \cdot \boldsymbol{n})}_{T_6} \\ & - [\![\nabla \boldsymbol{u}^* \cdot T]\!] + \langle \boldsymbol{n} \cdot T^* \rangle \cdot [\![\boldsymbol{n} \cdot \nabla \boldsymbol{u}]\!] + \langle \boldsymbol{n} \cdot T \rangle \cdot [\![\boldsymbol{n} \cdot \nabla \boldsymbol{u}^*]\!] \\ & - \boldsymbol{u}^* \cdot [\![\nabla \cdot T]\!], \end{aligned}$$

as presented in [29] with the addition of the convective term we have derived above. Using identities from [106], we can express the surface tension-related terms as

$$\begin{aligned} T_6 &= \boldsymbol{n} \cdot \Delta_\Sigma \boldsymbol{u}^* + 2 \nabla \boldsymbol{u}^* \cdot \nabla_\Sigma \boldsymbol{n} \\ &= \boldsymbol{n} \cdot \frac{\partial^2 \boldsymbol{u}^2}{\partial s^2} + 2\kappa \frac{\partial \boldsymbol{u}^*}{\partial s} \cdot \boldsymbol{t} \\ &= \boldsymbol{n} \cdot \Delta \boldsymbol{u}^* - \boldsymbol{n} \cdot (\boldsymbol{n} \cdot \nabla \nabla \boldsymbol{u}^*) \cdot \boldsymbol{n} - 3\kappa (\boldsymbol{n} \cdot \nabla \boldsymbol{u}^*) \cdot \boldsymbol{n}, \end{aligned}$$

where $\boldsymbol{t}$ is the tangent vector to the interface Γ. The expression in terms of arclength is most effective when an explicit parametrization of the interface is available. On the other hand, the expression in terms of ambient derivatives is also important, due to

$$\begin{aligned} [\![\boldsymbol{n} \cdot \Delta \boldsymbol{u}^* - \boldsymbol{n} \cdot (\boldsymbol{n} \cdot \nabla \nabla \boldsymbol{u}^*) \cdot \boldsymbol{n}]\!] &= 0 \\ [\![(\boldsymbol{n} \cdot \nabla \boldsymbol{u}^*) \cdot \boldsymbol{n}]\!] &= 0, \end{aligned}$$

which implies that a careful discretization can compute these quantities accurately, as they are continuous across the interface. We leave additional discussion of these choices to the main section of the paper.

BIBLIOGRAPHY

[1] G Agbaglah, R. Chiodi, and O. Desjardins. Numerical simulation of the initial destabilization of an air-blasted liquid layer. *Journal of Fluid Mechanics*, 812:1024–1038, 2017.

[2] G. Gilou Agbaglah. Numerical study of hole formation in a thin flapping liquid sheet sheared by a fast gas stream. *Physics of Fluids*, 33(6):062119, 2021.

[3] Charu C. Aggarwal. *Neural Networks and Deep Learning*. Springer, Cham, 2018.

[4] Alberto Aliseda and Theodore J. Heindel. X-ray flow visualization in multiphase flows. *Annual Review of Fluid Mechanics*, 53(1):543–567, 2021.

[5] Chinnaswamy Anandharamakrishnan et al. *Introduction to encapsulation of food ingredients*, chapter 2, pages 37–64. John Wiley & Sons, Ltd, 2015.

[6] D. M. Anderson, G. B. McFadden, and A. A. Wheeler. Diffuse-interface methods in fluid mechanics. *Annual Review of Fluid Mechanics*, 30(1):139–165, 1998.

[7] Thomas Bäck and Hans-Paul Schwefel. An overview of evolutionary algorithms for parameter optimization. *Evolutionary Computation*, 1:1–23, 03 1993.

[8] G. K. Batchelor. *An Introduction to Fluid Dynamics*. Cambridge Mathematical Library. Cambridge University Press, 2000.

[9] Jennifer C. Beale and Rolf D. Reitz. Modeling spray atomization with the kelvin-helmholtz/rayleigh-taylor hybrid model. *Atomization and Sprays*, 9(6):623–650, 1999.

[10] M. K. Bernauer and R. Herzog. Optimal control of the classical two-phase Stefan problem in level set formulation. *SIAM Journal on Scientific Computing*, 33:342–363, 2011.

[11] T. R. Bewley, P. Moin, and R. Temam. DNS-Based predictive control of turbulence: An optimal benchmark for feedback algorithms. *Journal of Fluid Mechanics*, 447:179–225, 2001.

[12] A. Bockhorn, S. H. K. Narayanan, and A. Walther. *Checkpointing Approaches for the Computation of Adjoints Covering Resilience Issues*, pages 22–31. Society for Industrial and Applied Mathematics, 2020.

[13] A. Borunda. The science of how climate change impacts fires in the west. science. *National Geographic*, 2021.

[14] A. Borzi and V. Schulz. *Computational Optimization of Systems Governed by Partial Differential Equations*. Siam, 2012.

[15] Julie K Bothell, Nathanael Machicoane, Danyu Li, Timothy B Morgan, Alberto Aliseda, Alan L Kastengren, and Theodore J Heindel. Comparison of x-ray and optical measurements in the near-field of an optically dense coaxial air-assisted atomizer. *International Journal of Multiphase Flow*, 125:103219, 2020.

[16] Cyril Bozonnet, Olivier Desjardins, and Guillaume Balarac. Traction open boundary condition for incompressible, turbulent, single- or multi-phase flows, and surface wave simulations. *Journal of Computational Physics*, 443:110528, 2021.

[17] Julien Carmona, N. Odier, Olivier Desjardins, Benedicte Cuenot, A. Misdariis, and A. Cayre. A comparative study of direct numerical simulation and experimental results on a prefilming airblast atomization configuration. *Atomization and Sprays*, 31(8):9–32, 2021.

[18] Western Regional Climage Center.

[19] R. Chiodi and O. Desjardins. A reformulation of the conservative level set reinitialization equation for accurate and robust simulation of complex multiphase flows. *Journal of Computational Physics*, 343:186–200, 2017.

[20] Robert Chiodi and Olivier Desjardins. General, robust, and efficient polyhedron intersection in the interface reconstruction library. *Journal of Computational Physics*, 449:110787, 2022.

[21] A. J. Chorin. A numerical method for solving incompressible viscous flow problems. *Journal of Computational Physics*, 135:118–125, 1997.

[22] W. de Campos Galuppo, A. Magalh aes, L. L. Ferrás, J. M. Nóbrega, and C. Fernandes. New boundary conditions for simulating the filling stage of the injection molding process. *Engineering Computations*, 38:762–778, 2021.

[23] M. C. Delfour and J.-P. Zolesio. *Shapes and Geometries - Metrics, Analysis, Differential Calculus, and Optimization*. Siam, 2011.

[24] F. Demoulin, P. Beau, G. Blokkeel, A. Mura, and R. Borghi. A new model for turbulent flows with large density fluctuations: Application to liquid atomization. *Atomization and Sprays*, 17:315–345, 2007.

[25] O. Desjardins, G. Blanquart, G. Balarac, and H. Pitsch. High order conservative finite difference scheme for variable density low Mach number turbulent flows. *Journal of Computational Physics*, 227:7125–7159, 2008.

[26] S. Dong. An outflow boundary condition and algorithm for incompressible two-phase flows with phase field approach. *Journal of Computational Physics*, 266:47–73, 2014.

[27] EPA. Climate change indicators: Snowfall.

[28] EPA. Sources of greenhouse gas emissions, 2020.

[29] A. Fikl and D. J. Bodony. Adjoint-based interfacial control of viscous drops. *Journal of Fluid Mechanics*, 911, 2021.

[30] A. Fikl, V. L. Chenadec, and T. Sayadi. Control and optimization of interfacial flows using adjoint-based techniques. *Fluids*, 5:156–156, 2020.

[31] R. Fosdick and H. Tang. Surface transport in continuum mechanics. *Mathematics and Mechanics of Solids*, 14:587–598, 2009.

[32] J. B. Freund. Adjoint-based optimization for understanding and suppressing jet noise. *Journal of Sound and Vibration*, 330:4114–4122, 2011.

[33] D. Fuster, J.P. Matas, Marty S., Popinet S., J Hoepffner, Cartellier A., and Zaleski S. Instability regimes in the primary breakup region of planar coflowing sheets. *J. Fluid Mech.*, 736:150–176, 2013.

[34] Daniel Fuster, Anne Bagué, Thomas Boeck, Luis Le Moyne, Anthony Leboissetier, Stéphane Popinet, Pascal Ray, Rubenand Scardovelli, and Stéphane Zaleski. Simulation of primary atomization with an octree adaptive mesh refinement and vof method. *International Journal of Multiphase Flow*, 35:550–565, 2009.

[35] H. Garcke, M. Hinze, and C. Kahle. Optimal control of time-discrete two-phase flow driven by a diffuse-interface model. *ESAIM: Control, Optimisation and Calculus of Variations*, 25:13–13, 2019.

[36] Irvin Glassman, Richard A. Yetter, and Nick G. Glumac. *Combustion (Fifth Edition)*. Academic Press, Boston, fifth edition edition, 2015.

[37] M. Gorokhovski and M. Herrmann. Modeling primary atomization. *Annual Review of Fluid Mechanics*, 40:343–366, 2008.

[38] A. Griewank and A. Walther. Algorithm 799: REVOLVE. an implementation of checkpointing for the reverse or adjoint mode of computational differentiation. *ACM Transactions on Mathematical Software*, 26:19–45, 2000.

[39] W. W. Hager and H. Zhang. A survey of nonlinear conjugate gradient methods. *Pacific Journal of Optimization*, 2:35–58, 2006.

[40] Austin Han and Olivier Desjardins. Liquid structure classification towards topology change modeling. In *ICLASS 2021, 15th Triennial International Conference on Liquid Atomization and Spray Systems*, Edinburgh, UK, August 29 - September 2, 2021, 2021.

[41] Theodore J. Heindel. X-ray imaging techniques to quantify spray characteristics in the near-field. *Atomization and Sprays*, 28:1029–1059, 2018.

[42] R. Henderson. Design, simulation, and testing of a novel hydraulic power take-off system for the pelamis wave energy converter. *Renewable Energy*, 31(2):271–283, 2006. Marine Energy.

[43] M. Hermann. A balanced force refined level set grid method for two-phase flows on unstructured flow solver grids. *Journal of Computational Physics*, 227:2674–2706, 2008.

[44] M. Hintermüller and D. Wegner. Optimal control of a semidiscrete Cahn–Hilliard–Navier–Stokes system. *SIAM Journal on Control and Optimization*, 52:747–772, 2014.

[45] J. O. Hinze. Fundamentals of the hydrodynamic mechanism of splitting in dispersion processes. *Aiche Journal*, 1:289–295, 1955.

[46] Robert Hooke and T. A. Jeeves. " direct search" solution of numerical and statistical problems. *J. Acm*, 8:212–229, 1961.

[47] K. Y. Huh. A phenomenological model of diesel spray atomization. *Proc. of The International Conf. on Multiphase Flows '91-Tsukuba*, 1991.

[48] A. James and J. Lowengrub. A surfactant-conserving volume-of-fluid method for interfacial flows with insoluble surfactant. *Journal of Computational Physics*, 201:685–722, 2004.

[49] A. Jameson. Aerodynamic design via control theory. *Journal of Scientific Computing*, 3, 1988.

[50] D. Jiang and Y. Ling. Impact of inlet gas turbulence on the formation, development and breakup of interfacial waves in a two-phase mixing layer. *Journal of Fluid Mechanics*, 921:A15, 2021.

[51] Maxime Kaczmarek, Rodrigo Osuna-Orozco, Peter Dearborn Huck, Alberto Aliseda, and Nathanaël Machicoane. Spatial characterization of the flapping instability of a laminar liquid jet fragmented by a swirled gas co-flow. *International Journal of Multiphase Flow*, 152:104056, 2022.

[52] Alan Kastengren, Christopher F. Powell, Dohn Arms, Eric M. Dufresne, Harold Gibson, and Jin Wang. The 7bm beamline at the aps: a facility for time-resolved fluid dynamics measurements. *Journal of Synchrotron Radiation*, 19(4):654–657, July 2012.

[53] Dokyun Kim and Parviz Moin. Subgrid-scale capillary breakup model for liquid jet atomization. *Combustion Science and Technology*, 192:1334–1357, 2010.

[54] A. N. Kolmogorov. On the breakage of drops in a turbulent flow. *Dokl. Akad. Nauk. SSSR*, 66:25–28, 1949.

[55] A. Kord and J. Capecelatro. Optimal perturbations for controlling the growth of a Rayleigh–Taylor instability. *Journal of Fluid Mechanics*, 876:150–185, 2019.

[56] N. Kühl, J. Kröger, M. Siebenborn, M. Hinze, and T. Rung. Adjoint complement to the volume-of-fluid method for immiscible flows. *Journal of Computational Physics*, 440:110411–110411, 2021.

[57] JC Lasheras, E Villermaux, and EJ Hopfinger. Break-up and atomization of a round water jet by a high-speed annular air jet. *Journal of Fluid Mechanics*, 357:351–379, 1998.

[58] C.K. Law. Recent advances in droplet vaporization and combustion. *Progress in Energy and Combustion Science*, 8(3):171–201, 1982.

[59] R. Lebas, T. Menard, P. A. Beau, A. Berlemont, and F. X. Demoulin. Numerical simulation of primary break-up and atomization: Dns and modelling study. *International Journal of Multiphase Flow*, 35:247–260, 2009.

[60] Y. Ling, D. Fuster, S. Zaleski, and G. Tryggvason. Spray formation in a quasi-planar gas-liquid mixing layer at moderate density ratios: A numerical closeup. *Phys. Rev. Fluids*, 2:014005, 2017.

[61] N. Machicoane, G. Ricard, R. Osuna-Orozco, P. Huck, and A. Aliseda. Influence of steady and oscillating swirl on the near-field spray characteristics in a two-fluid coaxial atomizer. *International Journal of Multiphase Flow*, 129:103318, 2020.

[62] Nathanael Machicoane, Julie K. Bothell, Danyu Li, Timothy B. Morgan, Theodore J. Heindel, Alan L. Kastengren, and Alberto Aliseda. Synchrotron radiography characterization of the liquid core dynamics in a canonical two-fluid coaxial atomizer. *International Journal of Multiphase Flow*, 115:1–8, 2019.

[63] Majid H. Majeed. Static contact angle and large water droplet thickness measurements with the change of water temperature. *Al-Nahrain Journal for Engineering Sciences*, 17:114–128, 2014.

[64] Adel Mansour and Norman Chigier. Dynamic behavior of liquid sheets. *Physics of Fluids A*, 3(12):2971–2980, December 1991.

[65] Philippe Marmottant and Emmanuel Villermaux. On spray formation. *Journal of Fluid Mechanics*, 498:73–111, 2004.

[66] Jean-Philippe Matas, Antoine Delon, and Alain Cartellier. Shear instability of an axisymmetric air–water coaxial jet. *Journal of Fluid Mechanics*, 843:575–600, 2018.

[67] Jean-Philippe Matas, Sylvain Marty, and Alain Cartellier. Experimental and analytical study of the shear instability of a gas-liquid mixing layer. *Physics of Fluids*, 23(9):094112, 2011.

[68] Jean-Philippe Matas, Sylvain Marty, Mohamed Seydou Dem, and Alain

Cartellier. Influence of gas turbulence on the instability of an air-water mixing layer. *Phys. Rev. Lett.*, 115:074501, August 2015.

[69] Jeremy McCaslin. *Development And Application Of Numerical Methods For Interfacial Dynamics In Turbulent Liquid-Gas Flows*. PhD thesis, Cornell University, New York, USA, 2015.

[70] C. Meneveau, T. S. Lund, and W. H. Cabot. A Lagrangian dynamic subgrid-scale model of turbulence. *J. Fluid Mech.*, 319:353–385, 2000.

[71] S. Menon. *Simulation of Combustion Dynamics in Gas Turbine Engines*, pages 33–42. Elsevier, Amsterdam, 2003.

[72] P. Moin and T. Bewley. Feedback control of turbulence. *Applied Mechanics Reviews*, 47:S3–s13, 1994.

[73] M. Moubachir and J.-P. Zolesio. *Moving Shape Analysis and Control*. CRC Press, 2019.

[74] T. Müller, A. Sänger, P. Habisreuther, T. Jakobs, D. Trimis, T. Kolb, and N. Zarzalis. Simulation of the primary breakup of a high-viscosity liquid jet by a coaxial annular gas flow. *International Journal of Multiphase Flow*, 87:212–228, 2016.

[75] National Oceanic and Atmospheric Administration, 2020.

[76] L. Opfer, I. V. Roisman, J. Venzmer, M. Klostermann, and C. Tropea. Droplet-air collision dynamics: Evolution of the film thickness. *Phys. Rev. E*, 89:013023, January 2014.

[77] P.J. O'Rourke and A. A. Amsden. The tab method for numerical calculation of spray droplet breakup. *SAE* Paper 872089, 1987.

[78] J. J. Otero, A. S. Sharma, and R. D. Sandberg. Adjoint-based optimal flow control for compressible DNS. 2016.

[79] M. Owkes and O. Desjardins. A computational framework for conservative, three-dimensional, unsplit, geometric transport with application to the volume-of-fluid (VOF) method. *Journal of Computational Physics*, 270:587–612, 2014.

[80] Mark Owkes and Olivier Desjardins. A computational framework for conservative, three-dimensional, unsplit, geometric transport with application to the volume-of-fluid (vof) method. *Journal of Computational Physics*, 270:587–612, 2014.

[81] Mark Owkes and Olivier Desjardins. A mesh-decoupled height function method for computing interface curvature. *Journal of Computational Physics*, 281:285–300, 2015.

[82] J. Palm, C. Eskilsson, G. M. Paredes, and L. Bergdahl. Coupled mooring analysis for floating wave energy converters using CFD: formulation and validation. *International Journal of Marine Energy*, 16:83–99, 2016.

[83] John Palmore and Olivier Desjardins. A volume of fluid framework for interface-resolved simulations of vaporizing liquid-gas flows. *Journal of Computational Physics*, 399:108954, 2019.

[84] Carly Phillips. How wildfires affect climate change - and vice versa. *The Conversation*, 2022.

[85] J. E. Pilliod and E. G. Puckett. Second-order accurate volume-of-fluid algorithms for tracking material interfaces. *Journal of Computational Physics*, 199:465–502, 2004.

[86] O. Pironneau. On optimum design in fluid mechanics. *Journal of Fluid Mechanics*, 64(1):97–110, 1974.

[87] Stephane Popinet and Stephane Zaleski. A front-tracking algorithm for accurate representation of surface tension. *International Journal for Numerical Methods in Fluids*, 30:775–793, 1999.

[88] A. Poux, S. Glockner, and M. Azaïez. Improvements on open and traction boundary conditions for Navier-Stokes time-splitting methods. *Journal of Computational Physics*, 230:4011–4027, 2011.

[89] R. D. Reitz. Modeling atomization processes in high-pressure vaporizing sprays. *Atom. Spray Technol.*, 3:309–337, 1987.

[90] Rolf D. Reitz. Modeling the primary breakup of high-speed jets. *Atomization and Sprays*, 14(1), 2004.

[91] Guillaume Ricard, Nathanaël Machicoane, Rodrigo Osuna-Orozco, Peter D.

Huck, and Alberto Aliseda. Role of convective acceleration in the interfacial instability of liquid-gas coaxial jets. *Phys. Rev. Fluids*, 6:084302, August 2021.

[92] William J. Rider and Douglas B. Kothe. Reconstructing volume tracking. *Journal of Computational Physics*, 141(2):112–152, 1998.

[93] Daniel Santos, Ana Colette Maurício, Vitor Sencadas, José Domingos Santos, Maria H. Fernandes, and Pedro S. Gomes. Spray drying: An overview. In Rosario Pignatello and Teresa Musumeci, editors, *Biomaterials*, chapter 2. IntechOpen, Rijeka, 2017.

[94] Ruben Scardovelli and Stéphane Zaleski. Direct numerical simulation of free-surface and interfacial flow. *Annual Review of Fluid Mechanics*, 31(1):567–603, 1999.

[95] Ruben Scardovelli and Stéphane Zaleski. Interface reconstruction with least-square fit and split eulerian–lagrangian advection. *International Journal for Numerical Methods in Fluids*, 41, 2003.

[96] M. Schanen, O. Marin, H. Zhang, and M. Anitescu. Asynchronous two-level checkpointing scheme for large-scale adjoints in the spectral-element solver nek5000. *Procedia Computer Science*, 80:1147–1158, 2016.

[97] J A Sethian. A fast marching level set method for monotonically advancing fronts. *Proceedings of the National Academy of Sciences*, 93(4):1591–1595, 1996.

[98] J. A. Sethian and P. Smereka. Level set methods for fluid interfaces. *Annual Review of Fluid Mechanics*, 35(1):341–372, 2003.

[99] Maurice M. Sevik and S. H. Park. The splitting of drops and bubbles by turbulent fluid flow. *Journal of Fluids Engineering-transactions of The Asme*, 95:53–60, 1973.

[100] G. Tomar, D. Fuster, S. Zaleski, and S. Popinet. Multiscale simulations of primary atomization. *Computers & Fluids*, 39:1864–1874, 2010.

[101] Virginia Torczon. On the convergence of pattern search algorithms. *SIAM Journal on Optimization*, 7(1):1–25, 1997.

[102] G. Tryggvason, B. Bunner, A. Esmaeeli, D. Juric, N. Al-Rawahi, et al. A

front-tracking method for the computations of multiphase flow. *Journal of Computational Physics*, 169(2):708–759, 2001.

[103] Salih Ozen Unverdi and Grétar Tryggvason. A front-tracking method for viscous, incompressible, multi-fluid flows. *Journal of Computational Physics*, 100(1):25–37, 1992.

[104] A. Vallet and R. Borghi. Modélisation Eulerienne de L'Atomisation d'un Jet Liquide. *C. R. Acad. Sci. Paris Sér. II b*, 327:11015–10208, 1999.

[105] Agienus Vrij. Possible mechanism for the spontaneous rupture of thin, free liquid films. *Discussions of The Faraday Society*, 42:23–33, 1966.

[106] S. W. Walker. *The Shape of Things: A Practical Guide to Differential Geometry and the Shape Derivative*. Siam, 2015.

[107] Sheng Wang and Olivier Desjardins. 3D numerical study of large-scale two-phase flows with contact lines and application to drop detachment from a horizontal fiber. *International Journal of Multiphase Flows*, 101:35–46, 2018.

[108] M. Wei and J. B. Freund. A noise-controlled free shear flow. *Journal of Fluid Mechanics*, 546:123–123, 2005.

[109] F. Xiao, M. Dianat, and J.J. McGuirk. Les of turbulent liquid jet primary breakup in turbulent coaxial air flow. *International Journal of Multiphase Flow*, 60:103–118, 2014.

[110] S. Xu and Z. J. Wang. Systematic derivation of jump conditions for the immersed interface method in three-dimensional flow simulation. *SIAM Journal on Scientific Computing*, 27:1948–1980, 2006.

[111] Zhi-Qiang Zhu, Yang Wang, Qiu-Sheng Liu, and Jing-Chang Xie. Influence of bond number on behaviors of liquid drops deposited onto solid substrates. *Microgravity Science and Technology*, 24, 06 2012.